

ABSTRACT

Title of dissertation: QUANTUM SIMULATIONS OF THE
ISING MODEL WITH TRAPPED IONS:
DEVIL’S STAIRCASE AND
ARBITRARY LATTICE PROPOSAL

Simcha Korenblit, Doctor of Philosophy
2013

Dissertation directed by: Professor Christopher Monroe
Joint Quantum Institute
University of Maryland Department
of Physics and
National Institute of Standards
and Technology

A collection of trapped atomic ions represents one of the most attractive platforms for the quantum simulation of interacting spin networks and quantum magnetism. Spin-dependent optical dipole forces applied to an ion crystal create long-range effective spin-spin interactions and allow the simulation of spin Hamiltonians that possess nontrivial phases and dynamics.

We trap linear chains of $^{171}\text{Yb}^+$ ions [1] in a Paul trap [2], and constrain the occupation of energy levels to the ground hyperfine clock-states, creating a qubit or pseudo-spin 1/2 system. We proceed to implement spin-spin couplings between two ions using the far detuned Mølmer-Sørensen scheme[3] and perform adiabatic quantum simulations of Ising Hamiltonians with long-range couplings. We then

demonstrate our ability to control the sign and relative strength of the interaction between three ions. Using this control, we simulate a frustrated triangular lattice, and for the first time establish an experimental connection between frustration and quantum entanglement. We then scale up our simulation to show phase transitions from paramagnetism to ferromagnetism for nine ions, and to anti-ferromagnetism for sixteen ions.

The experimental work culminates with our most complicated Hamiltonian - a long range anti-ferromagnetic Ising interaction between 10 ions with a biasing axial field, which I have led.

Theoretical work presented in this thesis shows how the approach to quantum simulation utilized in this thesis can be further extended and improved. It is shown how appropriate design of laser fields can provide for arbitrary multidimensional spin-spin interaction graphs even for the case of a linear spatial array of ions. This scheme uses currently existing trap technology and is scalable to levels where classical methods of simulation are intractable.

QUANTUM SIMULATIONS OF THE ISING MODEL WITH
TRAPPED IONS:
DEVIL'S STAIRCASE AND ARBITRARY LATTICE PROPOSAL

by

SIMCHA KORENBLIT

Dissertation submitted to the Faculty of the Graduate School of the
University of Maryland, College Park in partial fulfillment
of the requirements for the degree of
Doctor of Philosophy
2013

Advisory Committee:
Professor Christopher Monroe, Chair/Advisor
Professor Edo Waks
Professor Ted Jacobson
Professor Eite Tiesinga
Professor Ian Spielman
Professor Gretchen Campbell

© Copyright by
Simcha Korenblit
2013

Dedication

I dedicate this work to my family, who are my rock.

מִה־רַבּוֹ מַעֲשֵׂיךָ, יְהוָה-כֹּלֵם, בְּחִכְמָה עָשִׂיתָ;
מְלֵאָה הָאָרֶץ, קִנְיֶיךָ.

How manifold are Thy works, O LORD! In wisdom hast Thou made them
all; the earth is full of Thy creatures.

Psalms 104:24.

Acknowledgments

A doctoral program is rarely pursued in a vacuum. There are many people and organizations without whom this work would not be possible.

Firstly, I would like to thank my advisor, Chris Monroe, for giving me the opportunity to work at the cutting edge of quantum information. None of this would have happened if he did not happen to be in his office the day I knocked on his door, uninvited, displaying way more confidence than warranted for someone who has not yet been accepted to the Michigan Physics Department. Chris is probably one of the most hands on advisors out there, the kind of advisor who helps his group put up optic table “clouds” and electronics room shelving, while not micro-managing group members, and allowing us room to grow as independent scientists.

Throughout the years, I have benefited greatly from the advice and discussions of scientists outside our group. Here I will only mention a few, and I ask forgiveness in advance from whoever I may have forgotten. Luming Duan has collaborated with us intensively over the years, and has guided us on many issues and directions worth pursuing. His students Guin-Dar Lin, Zeh-Xuan Gong and Chao Shen have worked closely with us and supported our work. We have also had many useful discussions and collaboration with Jim Freericks and his post-doc Joseph Wang, especially regarding the effect of the transverse field on ion chain phonons. We have also received numerical support from Howard Carmichael and his student Changsuk Noh on the extremely intensive quantum trajectory simulations of our experiment.

Working in a world class lab means working with world class people. I have

had the privilege to work with extremely talented and dedicated post doctoral researchers. When I arrived in Maryland I knew nothing about ion trapping and had no knowledge in atomic physics. I received a patient and dedicated introduction from Ming-Schien Chang and Kihwan Kim, who were friends and teachers to me. Later I had the privilege of working with the post-docs Emily Edwards and Wes Campbell. From them I have learned much as well. Soon after arriving I had a an amazing graduate student join me - Rajibul Islam, and he shared the trenches with me for most of my time at Maryland.

Later other students have joined our project and contributed as well - Andrew Chew, an undergrad set up the iodine lock. Aaron Lee joined us as an undergrad and significantly improved my messy control program. He enjoyed this work so much he later joined us a grad student. Crystal Senko switched over from the fast gate project and was instrumental in trouble shooting our messy MBR problem. Jake Smith has joined as well and is quickly getting up to speed. Phil Richerme has joined the team as a post-doc and quickly began to contribute. I have also benefited from working and playing with many grad students, undergrads and post-docs not directly on the project. I list them here in no particular order. Peter Maunz, Dzimitry Matsukevich, Susan Clark, Dan Stick, Yisa Ramula, David Moehring, Kathy-Ann Brickman, Steve Olmschenk, Qudsia Quraishi, Jon Sterk, Mark Acton, Le Luo, Charles Conover, Brian Fields, Kenny Lee, Ilka Geisel, Jonathan Mizrahi, Brian Neyenhuis, Andrew Manning, Geoffrey Ji, Kale Johnson, Volkan Inlek, David Hucul, Dave Hayes, Ken Wright, Shantanu Debnath, Caroline Figgatt, Taeyoung Choi, Chenglin Cao, Daniel Brennan, and Volkan Inlek. It has been a pleasure and

a terrific learning experience working with you.

I would like to thank Crystal, Phil and Jake for reviewing my thesis.

I thank my thesis committee for taking upon themselves this service to the department and to greater science community.

I would also like to thank the Physics department staff, particularly Lorraine Desalvo and Jane Hessing, who have been very warm and welcoming to me when I made the transition from Michigan.

A man cannot live on professional relationships alone. I would like to thank the close friends who were there for me during my time here, but they are too numerous to mention. I would like to send a special thanks to Rob Feldmier who has been like a brother to me, and Rabbi and Rebbetzin Teitelbaum, who have been amazing to me. I would like to thank MesorahDC and the entire Jewish community of DC, who have guided the spiritual journey that paralleled my intellectual journey in this program.

This work is supported by the US Army Research Office (ARO) with funds from the DARPA Optical Lattice Emulator (OLE) Program and the IARPA MQCO Program, the NSF Physics at the Information Frontier Program, the NSF Physics Frontier Center at JQI.

Thank all of you and please forgive me if I omitted you.

Table of Contents

List of Figures	ix
List of Abbreviations	xi
1 Introduction	1
1.0.1 Classical Computation	2
1.0.2 Quantum Information Processing	3
1.1 The DiVincenzo Criteria	5
1.2 Quantum Mechanics	6
1.3 Adiabatic quantum simulation	8
1.3.1 Hydrogen-Like Atom	9
1.3.2 Transition Rules	14
1.3.3 Interaction Hamiltonian	14
1.3.4 Effective Hamiltonian	15
1.4 Conclusion	16
2 The $^{171}\text{Yb}^+$ ion	17
2.1 Ionization	19
2.2 Doppler Cooling	20
2.3 Optical Pumping	22
2.4 Detection	22
3 Quantum Control of The Ion	28
3.1 Light-Ion Interaction	28
3.2 Raman Transitions	29
3.3 Coupling Spin to Motion	31
3.4 Multi-Ion Gates	35
3.5 Conclusion	38
4 Experimental Setup	40
4.1 Introduction	40
4.2 Ion trap	40
4.2.1 Normal Modes	43
4.3 Micromotion	49
4.3.1 The Linear Trap	50
4.3.2 Trap Voltages and Control	52
4.3.3 Oscillating Trap Voltage	54
4.4 Optical Setup	56
4.4.1 Ionization	56
4.4.2 935 nm Repump	57
4.4.3 638 nm Repump	58
4.4.4 Cooling, Pumping, and Detecting with 369 nm	58
4.4.5 Iodine Spectroscopy Lock	65

4.4.6	Vanguard 355 nm Laser	68
4.4.7	Driving Raman and Mølmer-Sørensen Transitions with the Vanguard	72
4.4.8	Florescence Collection	78
4.5	Arbitrary Waveform Generator (AWG)	87
5	Experimental Procedure	90
5.1	Introduction	90
5.2	Temperature	90
5.3	Frequencies	91
5.4	Loading and Alignment	92
5.5	Raman Beams	94
5.6	Calibration	96
5.7	Imaging Calibration	98
6	Summary of Experiments	99
6.1	Introduction	99
6.2	Experimental Demonstration of the Ising interaction	100
6.2.1	Two spin case	102
6.2.2	Three spin case	103
6.3	Adiabatic quantum simulation	105
6.4	Phase diagram	109
6.5	Spin frustration and entanglement	112
6.6	Scalability of the quantum simulation	117
6.7	Scaling of imperfections	121
6.7.1	Spin-motion coupling	121
6.7.2	Diabaticity	122
6.7.3	Spontaneous Emission	122
6.7.4	Intensity fluctuations	123
6.7.5	Detection Errors	123
6.8	Conclusion and Outlook	128
7	Quantum Simulation of the Devil’s Staircase	130
7.1	Introduction	130
7.2	Overview	131
7.3	Experiment	132
7.4	Conclusion	148
8	Simulating the Ising Model with Arbitrary Control of the Couplings	153
8.1	Introduction	153
8.2	Control of an Arbitrary Lattice Hamiltonian	154
8.3	Examples	157
8.4	Implementation	158
8.5	Scalability	163
8.6	Conclusion	165

A	Linear Trap External Pi Filter	167
B	Optical Diagram Legend	169
C	AWG Function Library	170
D	Mathematica ROI and Discriminator Selection Script	181
	Bibliography	186

List of Figures

2.1	$^{171}\text{Yb}^+$ States and transition wavelengths	18
2.2	Doppler cooling	21
2.3	Optical pumping	23
2.4	$^{171}\text{Yb}^+$ Detection Scheme	25
2.5	Single ion histogram	26
2.6	Idealized histograms of multiple ions	27
3.1	Raman	30
3.2	RSB	33
4.1	Paul Trap	41
4.2	Transverse Modes For 10 Ions	47
4.3	Spin-Spin Couplings for 10 Ions	48
4.4	Linear trap 3D diagram	50
4.5	Trap Control Program	53
4.6	Trap Control Program - Electrodes Tab	55
4.7	MBR-110 Laser	59
4.8	369nm Laser and Optics Setup	63
4.9	Chamber and Resonant Beams	64
4.10	Iodine Spectroscopy Setup	67
4.11	MLUV Main Window	69
4.12	MLUV Oscillator Service	70
4.13	MLUV Amplifier Settings	71
4.14	MLUV Oven Settings	71
4.15	MLUV Position Controls	72
4.16	Frequency Combs for Raman	74
4.17	Vanguard Raman Setup	75
4.18	Raman Beams Close Up	79
4.19	Raman Profile	80
4.20	Florescence Collection	81
4.21	10 Bright Ions, Binned	82
4.22	Single Ion on ICCD	83
4.23	ICCD Histograms of 10 Ions	86
5.1	Trap Corner on ICCD	94
5.2	10 Ion Raman Spectrum	96
5.3	Automatic Side-Band Finder	97
6.1	Two Spins Coupled	102
6.2	Three Spins Coupled	104
6.3	Energy Level Diagram for 3 Spins	107
6.4	Measured Ferromagnetic Order	108
6.5	Phase Diagram for Three Ions	110

6.6	Spin Frustration on Triangular Lattice	113
6.7	Entanglement Witness	115
6.8	FM Simulation	119
6.9	FM Data vs Theory	124
6.10	FM Magnetization	127
7.1	6 Ion Spin-Spin Coupling Decay	134
7.2	Controlling the Phases of Simulation Pulses	137
7.3	Magnetization Phase Diagram for 6 Ions	139
7.4	Axial Simulation for 6 spins - States	141
7.5	6 Ion Staircase	142
7.6	6 Ion Complete Energy Spectrum	143
7.7	6 Ion Low Energy Spectrum	143
7.8	6 Ion Exponential Fit	145
7.9	Filtered 6 Spin Staircase	146
7.10	Power Filter VS Adiabaticity	147
7.11	10 Ion Coupling	148
7.12	Axial Simulation for 10 spins - States	149
7.13	10 Ion Exponential Fit	150
7.14	Power Filtered 10 Ion Data	151
8.1	Spectrum of N Ions with N Detunings	155
8.2	Example Solutions for Arbitrary Lattice Generation	159
8.3	Micromirror Array Simulator	160
8.4	AOM Array Simulator	161
8.5	Phase Array Simulator	162
8.6	1D Ising chain Scaling for Simulator	164
A.1	Pi Filter	167
B.1	Optical Diagram Legend	169

List of Abbreviations and Symbols

\hbar	Reduced Plank Constant
K_B	Boltzman Constant
AFM	Antiferromagnetic
AOM	Acousto Optic Modulator
BSB	Blue Sideband
COM	Center of Mass
CW	Continuous Wave
EOM	Electro Optic Modulator
FPGA	Field Programmable Gate Array
FM	Ferromagnetic
PCB	Printed Circuit Board
QE	Quantum Efficiency
SE	Schrödinger Equation
SHG	Second Harmonic Generator
THG	Third Harmonic Generator
RF	Radio Frequency
ROI	Region of Interest
RSB	Red Sideband
UHV	Ultra High Vacuum
VCA	Voltage Controlled Attenuator
IREAP	Institute for Research in Electronics and Applied Physics
NA	Numerical Aperture
NSA	National Security Agency

Chapter 1

Introduction

The work presented in this thesis is complex, and covers many subject areas, which cannot be given a full, bottom up presentation in this work. Furthermore, I do not possess this knowledge. Six years pursuing an experimental result does not allow for such a pursuit. Instead, I will present mostly information needed to understand the motivation for this work and the minimal amount of information needed to follow it as it is exposed. A deeper understanding can be pursued by the interested reader by reading the cited works. Many of the results presented here have already been presented in previously published works to which I have contributed in work and writing, but all the results presented are the fruits of a team effort.

Quantum systems are notoriously difficult to model efficiently using classical computers, owing to the exponential complexity in describing a general quantum state as the system grows in size. In the 1980s, Richard Feynman proposed to circumvent this problem by employing a control quantum system with tailored interactions and logic gates between quantum bits (qubits) in order to simulate the quantum system under investigation [4, 5].

Quantum spin models such as the Ising model have become a proving ground for Feynman's proposal, with systems of qubits behaving as effective spins and interactions engineered with external electromagnetic fields. The quantum Ising

model is the simplest spin Hamiltonian that exhibits nontrivial aspects of quantum magnetism such as spin frustration, phase transitions [6], and poorly understood spin glass and spin liquid phases [7, 8]. Indeed, solving for the ground state configuration of spins subject to a general fully-connected Ising interaction is known to be an NP-complete problem [9]. At the conclusion of this thesis I will show how a fully-connected Ising or more general Heisenberg spin model with arbitrary couplings across the spin network can be generated in a scalable system of trapped atomic ions, even for a one-dimensional chain in space. This may allow quantum simulations with hundreds of spins, where the physics cannot generally be predicted otherwise.

1.0.1 Classical Computation

Over the last century computers and electronics have made enormous advances and transformed our world our and lives. The theoretical foundations of modern computers are rooted in the work of Charles Babbage in the mid 19th century.

It was in the late 19th century, when the need to handle large amounts of data, and the emergence of the vacuum tube, spurred the creation of real world, albeit primitive computers.

The conception of solid state transistors in the 1920's and their technological application in the 1950's enabled a breakneck acceleration in the development of computers. The constant rate of transistor miniaturization led to the observation that the number of transistors on a processor doubles every two years ("Moore's Law") and processor performance doubles every 18 months. The average smartphone

that a consumer carries in their back pocket today is more powerful than a 1990's Cray-2 supercomputer!

Although the available computational power is increasing, this growth cannot continue forever, as technological hurdles such as thermal management and impurities become more severe as the density of transistors and processors continues to increase, and physical obstacles such as unwanted quantum effects due to shrinking component size threaten reliability. Currently, the smallest transistors fabricated in mass are 22 nm in length [10].

Furthermore, there are more fundamental limits to computation speed. A computational algorithm can be analyzed abstractly, and a relationship between the number of steps or other resources needed to solve a problem and the size of the problem can be established.

An important problem in computer science is factoring a large number into two prime numbers, as this can be used to decipher encrypted communications (using the RSA method). With known methods, the number of steps to find the prime factors grows exponentially with a linear growth in the number of digits of the problem number. This makes this problem practically unsolvable and hence the encryption is secure.

1.0.2 Quantum Information Processing

However, it is known that a computer with components that remain in a pure quantum state (undisturbed by uncontrolled external influences) only requires a

polynomial increase in steps [11]. This surprising result shows that quantum computers likely possess computational powers far beyond those of classical computers [4] (this is only a hypothesis though as the fundamental theories of computation are still in their infancy).

The other motivation for the development of quantum information processing machines is the problem of simulating quantum systems. As Feynman proposed in 1982 [4, 5], a well-controlled quantum system could efficiently simulate the behavior of a complex quantum model that is classically intractable. For example, a quantum simulator could be used to determine properties and dynamics derived of poorly understood models in condensed matter such as quantum magnetism [12], spin glasses [7], spin liquids [13] and high temperature superconductors [14, 15].

As the resources required to simulate quantum systems on a classical computer grow exponentially with linear growth of the quantum system, a machine that is itself in a quantum state analogous to a system we wish to investigate will naturally benefit from this growth in its computational space as its number of components grows linearly. This is likely the more important application of quantum information processing, as the number of digital quantum computing algorithms known is limited, but the number of quantum systems whose understanding can benefit are unlimited [16].

Furthermore, it has been shown that a universal quantum simulator is equivalent in computational power to a universal quantum computer up to a polynomial factor in the time needed for computation [17], and as such cannot simply be discounted as a more limited form of quantum computing.

1.1 The DiVincenzo Criteria

In order to implement the ideas discussed above, one needs a practical quantum system. DiVincenzo presented the grocery list of characteristics of such a system :

- Identification of well-defined qubits
- Reliable state preparation
- Low decoherence
- Accurate quantum gate operations and
- Strong quantum measurements

Although originally specified for a circuit quantum computer, the requirements for a quantum simulator are identical. The $^{171}\text{Yb}^+$ system has all of these characteristics. The qubits are well defined in the sense that each $^{171}\text{Yb}^+$ ion is exactly the same. The only variation between these qubits is due to local gradients in electric and magnetic fields. The technical details of the $^{171}\text{Yb}^+$ qubit will be discussed in detail in chapter 2. For now, it will be simply stated that in comparison to competing implementations (mainly solid state Josephson junction based systems [18, 19]) of qubits, the ion systems are superior in all of these criteria except one that is not listed - scalability. The storage of ions for long periods of time is difficult as it requires strong electric fields and very low pressures. In this work, we were limited to working with 16 ions. Although we faced multiple sources of errors that would prevent us from controlling more than 16 ions, the main limiter is our inability to

store in a stable crystal the ions for more than ~ 10 minutes. This is likely due to background atoms colliding with the chain, even at our working pressure of 10^{-12} Torr.

1.2 Quantum Mechanics

The development of quantum mechanics was spurred by false predictions and contradictions encountered by physicists in the late 19th and early 20th century. These problems spanned several different aspects of physics.

First, there was the famous ultraviolet catastrophe, which predicted the radiation of infinite energy from a blackbody at the limit of short wavelengths. Second there was the photoelectric effect, where light shining on a metal would cause a current that would inexplicably cease when the light frequency was reduced. Third, the double-slit experiment demonstrated wave-like behavior for light, except when a detector was placed at one of the slits leading to the baffling appearance of particle-like behavior. The fourth and most problematic discovery was that atoms were most likely composed of electrons in orbit around a small, positive nucleus. A classical description of this would seem to make matter itself impossible due to the electrons completely radiating away their energy, unless they were limited to discrete orbitals for an (at the time) inexplicable reason. These problems were resolved by the introduction of the photon, the de Broglie wave equation, and finally the development of quantum mechanics.

In the quantum mechanical description of physical systems the state is de-

scribed by a vector in a Hilbert space. This vector and its associated conserved quantities (“quantum numbers”) describe all that can be known about the system. The dynamics of such a system is described by the Schrödinger equation

$$H |\psi\rangle = i\hbar \dot{|\psi\rangle} \quad (1.1)$$

Where H is the Hamiltonian, an operator in Hilbert space that is the sum of the energy terms in the system, $|\psi\rangle$ is the wavefunction, a vector in Hilbert space, and \hbar is Planck’s constant, defined as the ratio between photon energy and angular frequency.

The most revolutionary aspect of this new theory is the wave-function description of nature: although particles are discrete (they are always observed as particles), some of their properties can only be described probabilistically. This probability is given by the probability amplitude $\langle\psi|\psi\rangle = \int \psi^* \psi dx$ integrated over the region of interest (this is the inner product of the vector in Hilbert space). The other observables of the system are extracted from the wavefunction using an operator, such that the expectation value for quantum mechanical observable A is

$$\langle A \rangle = \langle\psi| A |\psi\rangle \quad (1.2)$$

where A is a Hermitian matrix (so as to always have real expectation values).

If we assume the Hamiltonian is time independent, we can rewrite Eq. 1.1

$$E |\psi\rangle = H |\psi\rangle \quad (1.3)$$

by assuming that $|\psi\rangle$ has an oscillatory form

$$|\psi(t)\rangle = e^{-iEt/\hbar} |\psi(0)\rangle \quad (1.4)$$

and E is the energy of the eigenvector $|\psi(t)\rangle$.

In general, we define $|\psi(t)\rangle = U(t) |\psi(0)\rangle$ where

$$U(t) = T e^{-i \int H dt / \hbar} \quad (1.5)$$

is the evolution operator, which simplifies to $U(t) = e^{-iHt/\hbar}$ for time independent Hamiltonians.¹

1.3 Adiabatic quantum simulation

One method of quantum information processing is adiabatic quantum simulation. This approach is motivated by the adiabatic quantum computation algorithm first proposed as a method to solve NP-complete satisfiability problems [20]. The process of quantum adiabatic computation works as follows: a quantum system is initialized to the ground state of a trivial Hamiltonian. Next, the Hamiltonian is

¹ T is Dyson's time ordering operator. This operator handles the non-commutation of $H(t)$ for different t .

adiabatically deformed into the Hamiltonian of interest, whose ground state encodes the solution of a problem that has been mapped to the final Hamiltonian. If successful, the system will remain in the ground state and can be directly probed once the system arrives at the desired Hamiltonian. For quantum simulation of magnetically interacting spins, this approach allows the determination of ground states where the Hamiltonian can easily be written, yet the spin ground state cannot always be predicted, even with just a few dozen spins [21].

A precondition for the use of this state is satisfying the adiabaticity criterion²:

$$T \gg \frac{\epsilon}{g_{min}^2} \quad (1.6)$$

where T is total simulation time, $g_{min} = \min(E_1(t) - E_0(t))$ is the minimum energy gap between the ground state (or any other state we can trivially initialize) and closest coupled state, where $\epsilon = \max(|\langle 1, t | \frac{dH}{dt} | 0, t \rangle|)$ is the change in the Hamiltonian at time t for the coupling between those energy levels.

1.3.1 Hydrogen-Like Atom

In this work we be using $^{171}\text{Yb}^+$ ions as qubits. To understand their behavior, we will model them using a quantum mechanical model, first developed to describe the simplest atom - Hydrogen. In order to model the Hydrogen atom and other atoms that have only one valence electron, we assume a simple model of a negative electron orbiting a stationary positive nucleus in a spherically symmetric electric

²This is the criterion usually encountered in the literature. However, this criterion is not in true in general [23]

potential. Then we write our Hamiltonian

$$H = V + T = -\frac{1}{4\pi\epsilon_0} \frac{Ze^2}{r} + \frac{p^2}{2m_0} \quad (1.7)$$

where Z is the number of positive nuclear charges, e is the charge of the electron, r is the distance of the electron from the nucleus, ϵ_0 is the electric permittivity constant, and $\frac{p^2}{2m_0}$ is the kinetic energy of the electron (m_0 is its mass): $-\frac{\hbar^2}{2m_0}\nabla^2$.

We find the eigenfunctions that satisfy the Schrödinger equation:

$$\psi(r, \theta, \phi) = R(r)Y(\theta, \phi) \quad (1.8)$$

$$Y_l^m(\theta, \phi) \equiv \epsilon \sqrt{\frac{(2l+1)(l-|m|)!}{4\pi(l+|m|)!}} e^{im\phi} P_l^m(\cos\theta) \quad (1.9)$$

$$R(r)_l^n \equiv \sqrt{\left(\frac{2Z}{na}\right)^3 \frac{(n-l-1)!}{2n[(n+l)!]^3}} e^{-rZ/na} \left(\frac{2Zr}{na}\right)^l [2L_{n-l-1}^{2l+1}(2Zr/na)] \quad (1.10)$$

$$a \equiv \frac{4\pi\epsilon_0\hbar^2}{m_R e^2} \quad (1.11)$$

Where P_l^m are the associated Legendre functions, $2L_{n-l-1}^{2l+1}$ are the associated Laguerre polynomials, and m_R is the reduced mass of the nucleus and electron.

n, l and m are quantized numbers that label orthogonal eigenfunctions. These numbers are described as “good” quantum numbers. Their goodness is a result of the simplifying assumptions of the model. In the $^{171}\text{Yb}^+$ ion we will see that these assumptions are only roughly true, leading to metastable states defined by other quantum numbers. For Hydrogen-like atoms, n determines the energy of the sta-

tionary state, l (the azimuthal quantum number) orbital angular momentum., and m (the magnetic quantum number) the direction of angular momentum vector.

The definition of the Legendre polynomials restricts the values of l and m :

$$l = 0, 1, 2, \dots; m = -l, -l + 1, \dots, 0, 1, \dots, l \quad (1.12)$$

The Laguerre polynomial solution is found when one restricts the radial solution $R(r)$ to a non-diverging series. The same restriction truncates l at $n - 1$. Intuitively, we can understand that a finite kinetic energy implies finite angular momentum.

Using the standard definition of angular momentum, $L = r \times p$ and our previous implicit definition of the momentum operator, we can show the commutation relations for the Cartesian components of L to be

$$[L_i, L_j] = i\hbar\epsilon_{ijk}L_k \quad (1.13)$$

and if we define the raising and lowering operators as

$$L_+ = L_x + iL_y \quad L_- = L_x - iL_y \quad (1.14)$$

then we find that these are ladder operators for the atomic eigenstates

$$L_+ |l, m\rangle = \hbar \sqrt{(l-m)(l+m+1)} |l, m+1\rangle \quad (1.15)$$

$$L_- |l, m\rangle = \hbar \sqrt{(l+m)(l-m+1)} |l, m-1\rangle \quad (1.16)$$

There are additional complications to this simple model we must address before we can discuss the $^{171}\text{Yb}^+$ ion and its energy structure. First, the electron possesses an innate angular momentum, “Spin”, which is described by exactly the same math as angular momentum, however l for the electron is fixed at $1/2$ and so m only spans $-1/2, 1/2$. We label the operators for spin $\vec{S} \equiv \frac{\hbar}{2}\vec{\sigma}$ where $\vec{\sigma}$ is the Pauli spin vector - a vector of operators with components

$$\sigma_x \equiv \begin{pmatrix} 0 & 1 \\ 1 & 0 \end{pmatrix}, \sigma_y \equiv \begin{pmatrix} 0 & -i \\ i & 0 \end{pmatrix}, \sigma_z \equiv \begin{pmatrix} 1 & 0 \\ 0 & -1 \end{pmatrix} \quad (1.17)$$

Complicating this further, the proton(s) in the nucleus of the atom also have spin. These spins give the proton and electron a magnetic moment, and these experience a magnetic dipole force due to the magnetic field created by the orbiting electron. These add additional terms to the total atom Hamiltonian, of the form $H_d = -\mu \cdot B$. We define two new quantities, the total orbital angular momentum $J \equiv L + S$ and $F \equiv I + J$, where S is the total electronic spin and I is the total nuclear spin.

For most stable atomic states, where we ignore coupling between the outer electron and the inner electrons (LS coupling), we will label the atomic states using

the 'Russel-Saunders' convention

$$^{2S+1}L_J \quad (1.18)$$

The interaction of the electron with the magnetic field created by the rotating nucleus (in the electron's rest frame) gives rise to the fine structure splitting of the energy levels, and the interaction of the nucleus' dipole moment with the magnetic field created by the electron leads to a smaller perturbation of the energy levels, called the hyperfine splitting.

In atoms such as $^{171}\text{Yb}^+$, where the nuclear spin magnetic moment is non-zero (due to the odd number of nucleons), the hyperfine coupling will be strong, and so it will be necessary to add an energy term to the Hamiltonian for the dipole coupling between the nucleus' magnetic moment μ and the magnetic field from the electron, $H_{HF} = -\mu_I \cdot (B^l + B^s)$.

However, the dominant coupling term will be that of the total angular momentum, so we will write the eigenstates of the atom as superpositions of our previously uncoupled basis:

$$|J, M\rangle = \sum_{m_l + m_s = m_j} C_{m_l, m_s, m_j}^{L, S, L+S} |l, m_l\rangle |s, m_s\rangle \quad (1.19)$$

where the coefficients $C_{m_l, m_s, m_j}^{L, S, L+S}$ are the Clebsch-Gordan coefficients. These will be necessary to calculate transition strengths.

1.3.2 Transition Rules

What is the significance of all this? Well, from here we arrive at the rules which tell us what atomic transitions are allowed and which are forbidden. The restriction of atomic transitions will allow us to construct a useful qubit.

When the atom absorbs a photon, angular momentum is conserved. We consider a perturbation H^1 to the atom from an external electromagnetic field. The probability for a transition from a stationary state ψ_1 to ψ_2 will depend on the matrix element $\langle \psi_1 | H^1 | \psi_2 \rangle$. Considering only the dipole component of the multipole expansion of the field, the perturbation to the potential of the electron will be $\propto e\vec{r} \cdot \vec{E}$ which requires $\Delta l = \pm 1$ and $\Delta m = \pm 1, 0$ for a non-zero transition probability. We will see how these rules come in to play when we examine the allowed transitions of $^{171}\text{Yb}^+$ in [chapter 2](#).

1.3.3 Interaction Hamiltonian

For many systems, the Hamiltonian is a sum of a static term H_S and an interaction term H_I . If this is the case we may simplify our analysis by rotating into the static frame, so that the time evolution is only a function of H_I . So our total Hamiltonian in the Schrödinger picture (where all operators are static in time) is

$$H_T = H_S + H_I \tag{1.20}$$

And in the interaction 'picture'

$$|\psi^I(t)\rangle = e^{iH_S t/\hbar} |\psi^T(t)\rangle \quad (1.21)$$

$$H_S^I = e^{iH_S t/\hbar} H_S e^{-iH_S t/\hbar} = H_S \quad (1.22)$$

$$H_I^I = e^{iH_S t/\hbar} H_I e^{-iH_S t/\hbar} \quad (1.23)$$

where the superscript I (T) indicates interaction (Schrödinger) picture. We see that the static term remains unaffected, but now the interaction term in the interaction picture is time dependent. Rewriting the Schrödinger equation 1.1 in terms of the interaction picture, the static component of the Hamiltonian drops out and we are left with

$$H_I^I |\psi^I(t)\rangle = i\hbar |\dot{\psi}^I(t)\rangle \quad (1.24)$$

and now the dynamics only depend on the interacting component of the Hamiltonian.

1.3.4 Effective Hamiltonian

For highly complex systems the interaction picture is still too complex to allow for analytical analysis. For many of these systems, including the spins in the ion trap, simplifying assumptions can be made to rewrite an even simpler Hamiltonian. The following treatment, succinctly presenting the formalism developed by D.F.V.

James[24], can be applied to interaction Hamiltonians of the form

$$H_I(t) = \sum_{n=1}^N H_n e^{-i\omega_n t} + H_n^\dagger e^{i\omega_n t} \quad (1.25)$$

where we are summing over N oscillatory terms, and $0 < \omega_1 < \omega_2 \dots \omega_N$. Then we can derive the effective Hamiltonian given by

$$H_{eff}(t) = \sum_{n,m=1}^N \frac{1}{\hbar \bar{\omega}_{mn}} [H_m, H_n^\dagger] e^{i(\omega_m - \omega_n)t} \quad (1.26)$$

and $\frac{1}{\bar{\omega}_{mn}} = \frac{1}{2} \left(\frac{1}{\omega_m} + \frac{1}{\omega_n} \right)$.

This Hamiltonian is the result of several approximations. First the interaction evolution operator 1.5 is time averaged, so that all fast changes are neglected (general case of rotating wave approximation). The second approximation is neglecting the higher order terms of the averaged evolution operator's time ordered expansion. Applying a second rotating wave approximation leads to 1.26. We will utilize this powerful tool when we treat light-ion interactions in 3.

1.4 Conclusion

This brief introduction to quantum information processing with ions and quantum mechanics has laid down the ground work for understanding the quantum aspects of manipulating a $^{171}\text{Yb}^+$ ion, that will be introduced in the following chapter.

Chapter 2

The $^{171}\text{Yb}^+$ ion

Now that we have discussed the basic physics necessary to understand atomic transitions and energy states, we will introduce our atomic system of choice: the $^{171}\text{Yb}^+$ ion[1]. We will discuss in 4.2 how we actually trap and create these ions from a Yb metal.

The discussion of how we generate and direct the light on the ion will have to wait until chapter 4.

Many ions are used throughout the world in quantum information experiments, mostly from the alkaline earth metals. These are chosen so that once singly ionized the ion will have a hydrogen-like electronic structure, which is more easily understood and controlled.

The second important feature is that the energy structure is such that the ion can be forced through optical pumping and cycling transitions to be constrained to two energy levels, so that it behaves as an effective spin (a qubit). Our ion has a nuclear spin of $1/2$, giving it the simplest hyperfine structure possible in its ground state.

For our qubit, we will be using the ground state $^2S_{1/2}$ energy manifold, and the clock states $|F = 0, m_f = 0\rangle$ as our “down” ($|\downarrow\rangle$) state and $|F = 1, m_f = 0\rangle$ as our “up” ($|\uparrow\rangle$) state. These states are the eigenstates of the σ_z operator with

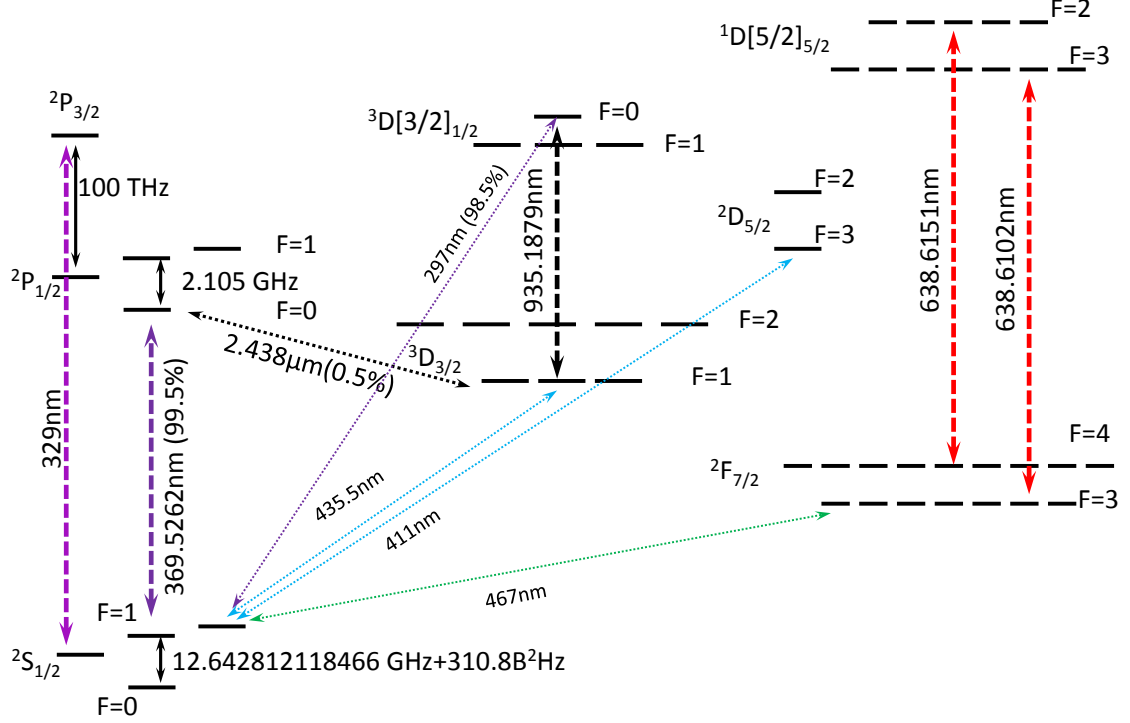


Figure 2.1: The $^{171}\text{Yb}^+$ ion states with transition wavelengths.

eigenvalues 1 and -1 respectively. The clock states are so named as they are used in atomic clocks due to only having a second order Zeeman energy shift, making them robust to magnetic noise. Correspondingly, this ensures the qubits a long T_2 coherence time - 2.5 s [1] without magnetic shielding, orders of magnitude longer than non-clock state qubits with magnetic shielding or magnetic-field feedback.

We use the resonant $^2S_{1/2}$ to $^2P_{1/2}$ transition for cooling, state initialization and detection. As we scatter on this transition, there is a 0.5% chance of decaying out of this cycle to the $^2D_{3/2}$ state. In order to correct for this we irradiate the ion with 935.1879 nm light modulated at 3.07 GHz in order to remove the population from $^2D_{3/2} |F=1\rangle$ and $^2D_{3/2} |F=2\rangle$ to the $^3D[3/2]_{1/2}$ state. This is a metastable state ('Bracket State') where the usual 'good' quantum numebrs are no longer valid

¹. The ion has a 98.5% chance of decaying back to $^2S_{1/2} |F = 1\rangle$ from this state, so it is quickly restored to the correct qubit state (this will however create an error in the phase of one qubit relative to other qubits in the chain).

A much less likely event is the ion transitioning to the $^2F_{7/2}$ state. This happens once in about an hour per ion. It is likely caused by a collision with a background atom in the Ultra High Vacuum Chamber (UHV), as this is a forbidden octopole transition [26]. Previously, we have used 638.61 nm light that is scanned between the two resonance frequencies. We have found that our intense 355 nm Raman beams are actually better at retrieving the ion from this long lived (~ 6 years) dark state, but it is possible that this is due to YbH^+ formation rather than transition to the $^2F_{7/2}$ state [27]. The 355 nm radiation would then disassociate this ionic molecule and return the ion to a coolable state.

2.1 Ionization

The source of our ions is a nearly pure source of neutral $^{171}\text{Yb}^+$. This source is a solid metal, sliced into small shards that are then forced into a narrow stainless steel tube, which is clamped off at one end. A wire is spot welded to the tube, and the tube is fed into a titanium holder, designed to have a high electric resistance and low thermal conductivity so as to isolate the Ohmic heating to the $^{171}\text{Yb}^+$ oven.

A current of roughly 2.3 Amps is run through this circuit (the holder is grounded

¹In this state the outer electron couples to the core electrons, and the state is written as $^{2s_0+1}[K]_J$, Where s_0 is the spin of the outer electron, K is the total angular momentum of the core and the angular momentum of the outer electron, and J is K and the spin of the outer electron. The letter preceding the bracket is not part of the notation but is L for the core in the usual LS notation. [25]

to the chamber). The oven is oriented towards the trapping region, where a 399 nm beam will excite the neutral Yb from 1S_0 to 1P_1 . A powerful 355 nm beam or 369 nm beam will then excite an electron to the continuum. Some of these $^{171}\text{Yb}^+$ ions will be sufficiently cooled by Doppler cooling to be trapped.

2.2 Doppler Cooling

Doppler cooling is achieved by scattering red detuned light from the resonant transitions [28] for the $^2S_{1/2}$ to $^2P_{1/2}$ transitions, as illustrated in Fig. 2.2. The light is tuned to a wavelength of 369.521525 nm, and detuned 25 MHz from resonance, while the transition has a 20 MHz linewidth. To ensure that the ion is cooled for both $F=0$ and $F=1$ states of the $^2S_{1/2}$ manifold, the light is modulated by an Electro Magnetic Modulator (EOM) at half the combined hyperfine splitting of the $^2S_{1/2}$ and $^2P_{1/2}$ states. The second order sideband allows the off resonant cooling of the $|\downarrow\rangle$ state. Doppler cooling utilizes the Doppler shift of the resonant frequency in the frame of the moving ion, such that when the ion is moving towards the oncoming light it is blue shifted towards resonance. The ion will then spontaneously emit a photon into a random direction, so on average losing momentum in the direction of the oncoming beam. The temperature limit of this random process is the 'Doppler cooling limit', $h\gamma/2K_B$, where γ is the linewidth of the transition and K_B Boltzmann's constant. For the S-P transition linewidth of 19.7 MHz, this corresponds to $5 * 10^{-3}$ K. The relation $K_B T = \bar{n} \hbar \omega$ [29] implies for our transverse direction of motion an average of ~ 12 phonons after Doppler cooling.

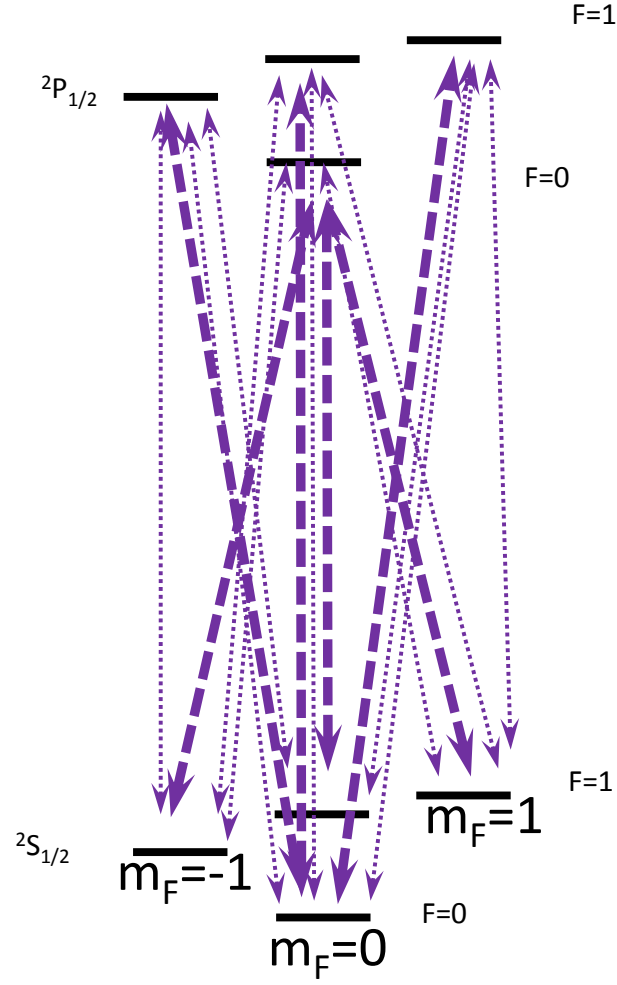


Figure 2.2: Doppler cooling the $^{171}\text{Yb}^+$ ion. Note that the 935 nm repump transition is not shown here. The wide lines represent the lasers driving transitions. The narrow lines represent the allowed decays.

2.3 Optical Pumping

Once the ion chain is sufficiently cooled (after Doppler cooling and sideband cooling), we must prepare the ions in a pure and known quantum state. This can be done with high fidelity. We apply light resonant with a transition from the $|\uparrow\rangle$ state to the $^2P_{1/2}$ $F=1$ state (as shown in 2.3), leading to a cycle that with our beam power of $\approx 10\,\mu\text{W}$ pumps the ion to the $|\downarrow\rangle$ state within $1.5\,\mu\text{s}$ with over 99% fidelity.

2.4 Detection

The detection scheme of the $^{171}\text{Yb}^+$ ion relies on the large separation of $|\uparrow\rangle$ and $|\downarrow\rangle$ states versus the linewidth of the detection transition. We use light resonant with the $|\uparrow\rangle$ to the $^2P_{1/2}|F=0\rangle$ transition, and polarize the light so as to be resonant with all the m_f states (i.e. both linear and circularly polarized light). The linewidth of this transition is $19.7\,\text{MHz}$, while the laser light linewidth is $\approx 100\,\text{KHz}$ wide, and the separation between the $|\uparrow\rangle$ and $|\downarrow\rangle$ states is $12.6\,\text{GHz}$, so off-resonant scattering is small (but not negligible). Also, note that transitions from $^2P_{1/2}|F=0\rangle$ to $|\downarrow\rangle$ are forbidden by transition laws.

This allows us to create a closed cycle of absorption and emission - a cycling transition. There is a small complication here - without a magnetic field to break the degeneracy, a coherent dark state may occur [30]. In this situation, the bright states interfere destructively, and detection fails. However, we apply a magnetic field via an electromagnet under the UHV chamber. This magnet serves multiple purposes -

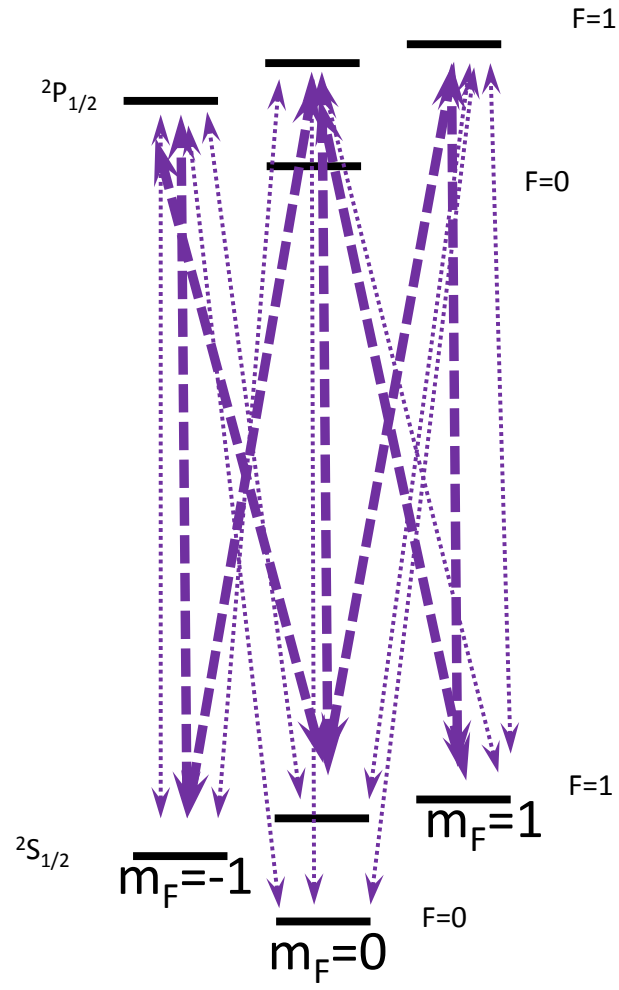


Figure 2.3: Optical pumping of the $^{171}\text{Yb}^+$ ion.

it defines the quantization axis (the Z-spin axis corresponding to the σ_z operator), and it breaks the degeneracy of the $^2S_{1/2}$ manifold, thus preventing this coherent dark state. We estimate the field to be roughly 5 Gauss, providing a Zeeman shift of ~ 7 MHz ($310 * 5^2$ Hz). This can be measured by taking a Raman spectrum of the excitable sidebands.

As the ion fluoresces, the distribution of detected scattered light should ideally follow a Poissonian. However, the possibility of off resonant excitation of the dark state forces us to convolute this distribution with an exponential function[31]. A similar analysis is appropriate for the dark state. The atomic physics derived distributions are deformed by complicating factors. First, there is unwanted scatter off the electrodes of the trap. Second, there is the device physics of the imaging device, which will lead to spurious counts from false photon detections and noise during electrical readout. I will discuss this more in depth in 4.4.8. When detecting the state of a single ion, we can expect a histogram of counts as in figure 2.5. As is seen in the figure, there are two distributions, one centered around the average dark count, and one around the average bright state count of roughly 10 counts. In this case we can use a discriminator value that leads to an equal probability of mistaking $|\uparrow\rangle$ for $|\downarrow\rangle$ and vice versa. i.e the overlap of the distributions determines our single spin detection error.

However, when we must detect multiple ions, we encounter two problems when simply collecting the light into a Photo Multiplying Tube (PMT). First, we do not have the ability to detect the true eigenstate of the chain, only how many ions are bright. This is acceptable in some experiments, where total number of bright ions

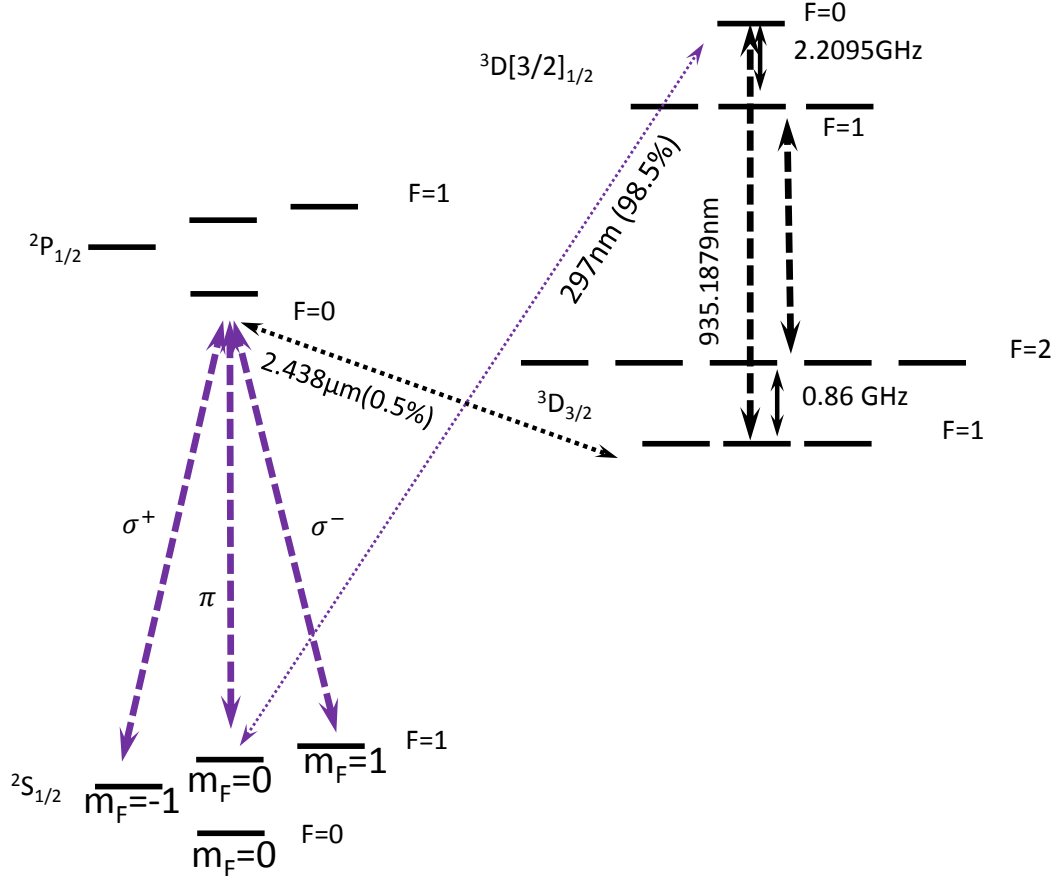


Figure 2.4: The $^{171}\text{Yb}^+$ ion detection scheme. The additional 3D $F=2$ to $F=1$ resonant light is needed for the optical pumping, since the ion may occupy either $^3D_{3/2}$ hyperfine states. Only pertinent states and transitions are shown.

is the quantity of interest. Second, as the number of spins increases, the average number of bright counts per ions bright should naively increase as $N_{ions} \times \text{average count for one ion}$, assuming a uniform detection beam intensity across the chain (we will see this is not exactly the case). But this leads to increasing overlap between the different distributions, so even for the task of just detecting the total number of ions bright the PMT will under-perform compared to a device with spatial information, such as a Charge Coupled Device (CCD) camera.

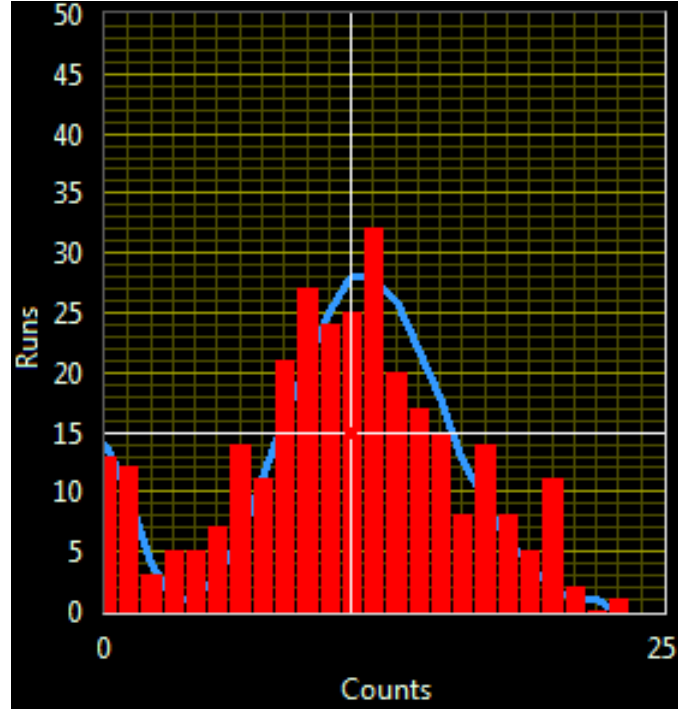


Figure 2.5: Measured count histogram after Doppler cooling with typical experimental conditions. The ion is Doppler cooled for 3ms, during which the ion scatters 10 photons on average into the light collecting Photo Multiplier Tube (PMT). Here, we are not detecting the scattered Doppler cooling light. Rather, we are following the cooling by a $800\text{ }\mu\text{s}$ resonant detection pulse and light collection. This is repeated 100 times and then a histogram is constructed from the number of counts collected by the PMT via the imaging optics for each detection. As can be seen from the graph, the ion is not completely bright following cooling. This screen shot from the control program also shows the Poissonian fits for the dark and bright states. The mean value of the fits are entered as parameters. The fitted amplitudes are interpreted as probabilities for the number of ions bright.

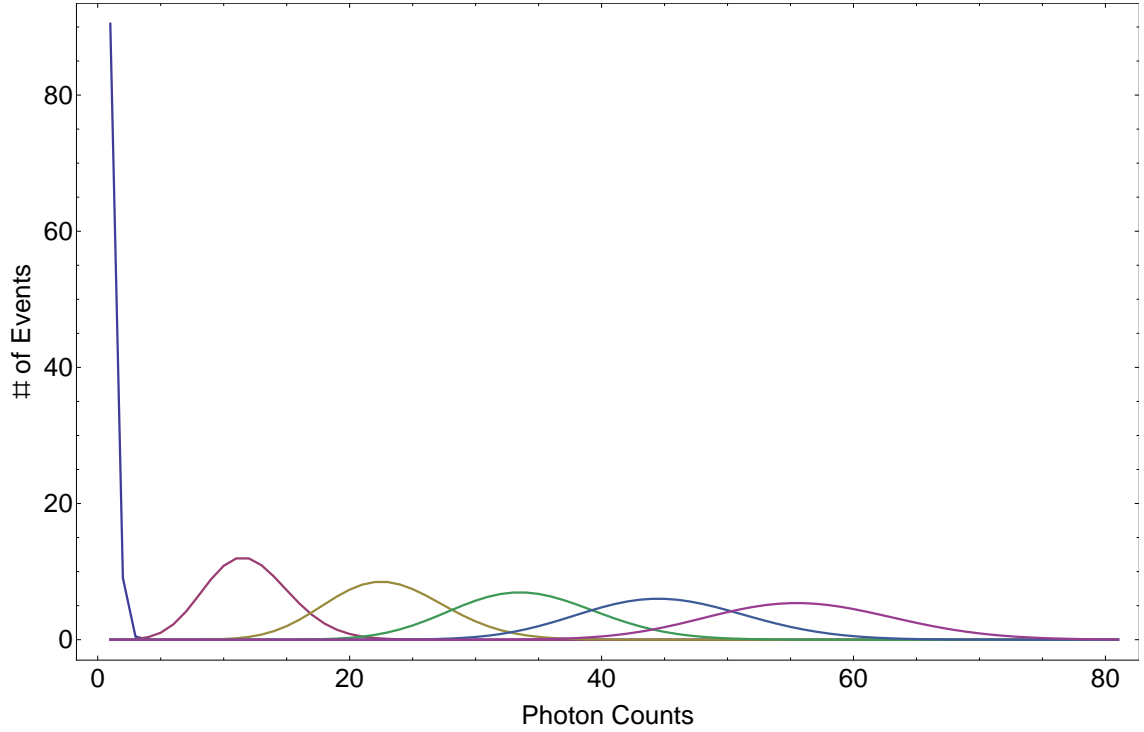


Figure 2.6: Poissonians for the dark state and up to five ions bright. These are idealized bright states as there is no leakage to the dark state. The leftmost distribution is the dark state, and the distribution peaking at 10 counts is a single bright ion. The other distributions are centered at multiples of 10 ($N \times 10$), corresponding to N ions bright. Realistic distributions would have worse overlap due to this effect, including a broadening of the dark histogram as well.

Chapter 3

Quantum Control of The Ion

3.1 Light-Ion Interaction

The last ingredient necessary to make the ion a useful qubit or simulated spin is the ability to control its internal state. For the purpose of this exposition I will utilize the effective Hamiltonian theory introduced in 1.3.4¹. The simplest application of this theory is to the analysis of the AC Stark shift [24]. Applying an off-resonant field, detuned by Δ from the hyperfine splitting of the qubit states ω_{hf} with coupling coefficient Ω , we derive the interaction Hamiltonian

$$H_I = \frac{\hbar\Omega}{2}(|\uparrow\rangle\langle\downarrow| e^{-i\hbar\Delta t} + |\downarrow\rangle\langle\uparrow| e^{i\hbar\Delta t}) \quad (3.1)$$

Applying equation 1.26 to the single harmonic term H_1 to get

$$H_{Stark} = \frac{\hbar^2\Omega^2}{4} \frac{1}{2\hbar} (-|\uparrow\rangle\langle\downarrow| |\downarrow\rangle\langle\uparrow| \frac{2}{\Delta} - |\downarrow\rangle\langle\uparrow| |\uparrow\rangle\langle\downarrow| \frac{2}{\Delta}) \quad (3.2)$$

resulting in

$$H_{Stark} = -\frac{\hbar\Omega^2}{4\Delta} (|\uparrow\rangle\langle\uparrow| - |\downarrow\rangle\langle\downarrow|) \quad (3.3)$$

¹I am still following here the compact approach presented by James, which simplifies the treatment but somewhat obscures the physical justifications. For a different and lengthier presentation, see [32].

We see that the laser is dressing the qubit states and shifting their effective energy in opposite directions and by equal amounts. This is equivalent to a phase gate on a single spin - as the spin is precessing while shifted by the field, it will become out of phase with other spins not under the influence of the field. Alternately, it may become out of phase with an oscillator that was supposed to be locked to the spin's natural precession frequency - a persistent concern for the experiment. We will see in 4 how we can mitigate this. It is important to note that this is only the simplest A.C. Stark shift possible, as a Stark shift can be a multi-photon process, rather than the two photon process presented here.

3.2 Raman Transitions

We now add a third, higher energy level to the system, $|e\rangle$, as depicted in Fig 3.1. Applying two light frequencies ω_1 and ω_2 detuned by Δ from $|e\rangle$, the beat frequency ω_{hf} will drive this transition, while only negligibly populating $|e\rangle$.

We write the interaction Hamiltonian

$$H_I = \frac{\hbar\Omega_1}{2\Delta}|e\rangle\langle\uparrow| e^{-i\Delta t} + \frac{\hbar\Omega_2}{2\Delta}|e\rangle\langle\downarrow| e^{-i\Delta t} + h.c. \quad (3.4)$$

And apply 1.26:

$$H_{eff} = -\frac{\hbar\Omega_1^2}{4\Delta}(|e\rangle\langle e| - |\uparrow\rangle\langle\uparrow|) - \frac{\hbar\Omega_2^2}{4\Delta}(|e\rangle\langle e| - |\downarrow\rangle\langle\downarrow|) + \frac{\hbar\Omega_1\Omega_2}{4\Delta}(|\downarrow\rangle\langle\uparrow| - |\uparrow\rangle\langle\downarrow|) \quad (3.5)$$

where $\Omega_i = \gamma\sqrt{\frac{I_i}{I_{Sat}}}$ is the coupling coefficient for beam i, I_i is the intensity of beam i,

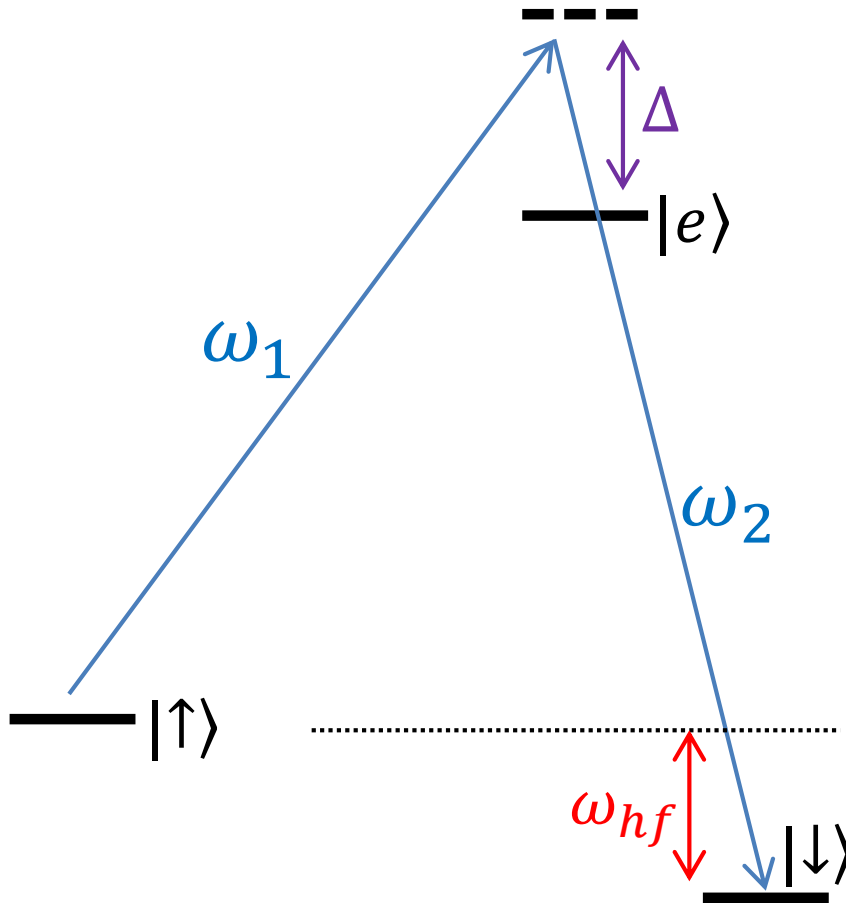


Figure 3.1: Off resonant coupling of the spins. $|e\rangle$ is negligibly populated for $\Delta \gg \gamma\Omega_i$

I_{Sat} is the saturation intensity of the transition for that beam, and γ is the radiative linewidth for that transition.

We see the effect is an AC Stark shift on all levels (a **symmetric** effect for both qubit levels for equal fields) and a coupling between the qubit levels. This is equivalent to a spin under the influence of a transverse field, as $(|\downarrow\rangle\langle\uparrow| - |\uparrow\rangle\langle\downarrow|) = i\sigma_y$. We will refer to the beatnote that drives this transition from hereon as “carrier”.

3.3 Coupling Spin to Motion

So far we have neglected the fact that the ion is confined in a harmonic well. This will be treated more in depth in 4.2. Using the standard quantum mechanical treatment of the harmonic oscillator, we use the ladder operators to lower and raise the number of motional quanta (“phonons”) of the ion with mass m and harmonic vibration frequency ω with the Hamiltonian $H = \frac{\hat{p}^2}{2m} + \frac{1}{2}m\omega^2\hat{x}^2$

$$a = \sqrt{\frac{m\omega}{2\hbar}}\left(\hat{x} + \frac{i}{m\omega}\hat{p}\right) \quad (3.6)$$

$$a^\dagger = \sqrt{\frac{m\omega}{2\hbar}}\left(\hat{x} - \frac{i}{m\omega}\hat{p}\right) \quad (3.7)$$

where the state representing the number of phonons is designated $|n\rangle$, and the ladder operators give

$$a |n\rangle = \sqrt{n} |n-1\rangle \quad (3.8)$$

$$a^\dagger |n\rangle = \sqrt{n+1} |n+1\rangle \quad (3.9)$$

$$a^\dagger a |n\rangle = n |n\rangle \quad (3.10)$$

and the commutator $[a, a^\dagger] = 1$.

Applying two fields with a beat frequency δ detuned to the red (blue) by the energy of the phonon, we can couple the spin to the ions motion and remove (add) a phonon while flipping the spin, as in figure 3.2. This scheme transfers momentum from the fields to the ion. The mode excited is selected spatially by the beat frequency wavevector δk , and spectrally by the beat frequency $\delta = \omega_2 - \omega_1 = \omega_{hf} + \omega_{mode}$

This treatment assumes that we are in the resolved sideband limit, i.e. the exposure of the ion is long enough and low power enough that the driven transition is not broadened to overlap with the carrier or other modes. We can illuminate this effect by writing the interaction Hamiltonian for this situation

$$H_I = \frac{\hbar\Omega}{2} (e^{-i(\delta k \cdot \vec{r} - (\delta\omega)t - \Delta\phi)} \sigma_+ + e^{+i(\delta k \cdot \vec{r} - (\delta\omega)t - \Delta\phi)} \sigma_-) \quad (3.11)$$

where Ω is the coupling strength of the qubit states, δk is the wavevector difference of the two beams, $\delta\phi$ is the phase difference of the beams, \vec{r} is the location

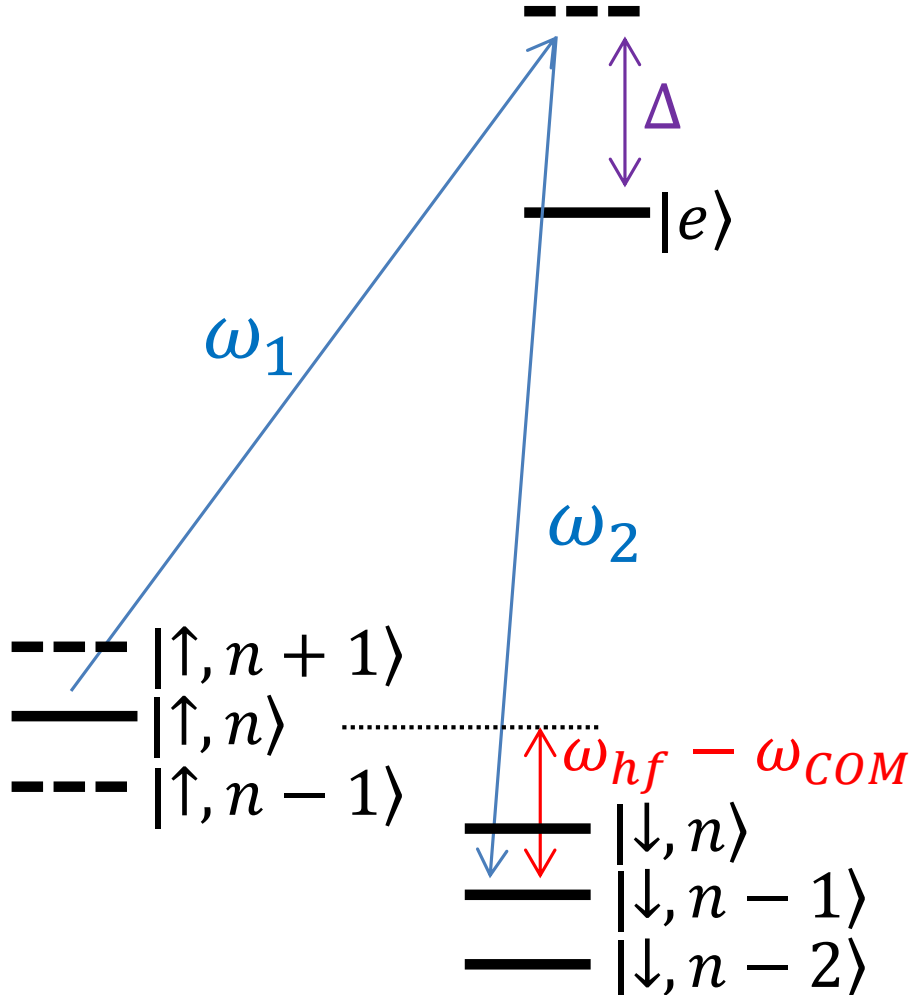


Figure 3.2: Driving a Red Side Band (RSB). The beat frequency $\delta\omega = \omega_2 - \omega_1 = \omega_{hf} - \omega_{COM}$ imparts a spin-dependent momentum kick that takes the ion from $|\uparrow, n\rangle$ to $|\downarrow, n-1\rangle$ by absorbing a photon from ω_1 and emitting a photon into ω_2 .

of the ion, and $\delta\omega = \omega_2 - \omega_1 - \Delta$, i.e. the beat frequency. Simplifying this general description to account for only motion along the transverse-x direction, and writing the coordinate as $\hat{x} = x_0 + \frac{q}{\sqrt{2}}(a + a^\dagger)$, and $q = \sqrt{\frac{\hbar}{M\omega}}$ we rewrite 3.11 as

$$H_I = \frac{\hbar\Omega}{2} (e^{-i(\delta k(x_0 + \frac{q}{\sqrt{2}}(a+a^\dagger)) - (\delta\omega)t - \delta\phi)} \sigma_+ + (e^{i(\delta k(x_0 + \frac{q}{\sqrt{2}}(a+a^\dagger)) - (\delta\omega)t - \delta\phi)} \sigma_-) \quad (3.12)$$

where δk now only refers to the wavevector difference in the x direction. Assuming the spatial spread of the ion relative to the beat wavelength is small, we make the Lamb-Dicke approximation $\eta = \delta k q / \sqrt{2} \ll 1$, and keep leading order terms in the phonon operators

$$H_I = \frac{\hbar\Omega}{2} (e^{-i(\delta k x_0 - (\delta\omega)t - \delta\phi)} (1 - i\eta(ae^{-i\omega t} + a^\dagger e^{i\omega t})) \sigma_+ + (e^{i(\delta k x_0 - (\delta\omega)t - \delta\phi)} (1 + i\eta(ae^{-i\omega t} + a^\dagger e^{i\omega t})) \sigma_-) \quad (3.13)$$

where we have rotated into the frame of the vibrational modes ω [32].

If we set $\delta\omega = \pm\omega$,

$$H_{BSB} = \frac{\hbar\Omega\eta}{2} e^{-i(\delta k x_0 - \delta\phi)} a^\dagger \sigma_+ + h.c. \quad (3.14)$$

$$H_{RSB} = \frac{\hbar\Omega\eta}{2} e^{-i(\delta k x_0 - \delta\phi)} a \sigma_+ + h.c. \quad (3.15)$$

The RSBs will allow us to cool our ion chain beyond the Doppler cooling limit by coherently removing phonons.

3.4 Multi-Ion Gates

Now that we have introduced a way to couple the ion spin to its motion, we can show a way to create gates between ions, using their motion as a bus to transport information between disparate spins [3, 33, 34, 35]. By applying beatnotes symmetrically detuned from carrier we will virtually excite normal modes, and induce sign dependent Stark shifts on ions, where the phase accrued on each spin will depend on the mode coupled and the ion location in the chain.

Generalizing equation 3.13 to multiple ions, while still only coupling to x direction phonons, we rewrite equation 3.13

$$\begin{aligned}
H_I = \sum_i^N \frac{\hbar \Omega_i}{2} [& (e^{-i(\delta k x_0^i - (\delta \omega)t - \delta \phi_i)}) (1 - \sum_{m=1}^N i \eta_{i,m} (a_m e^{-i\omega_m t} + a_m^\dagger e^{i\omega_m t})) \sigma_+^i \\
& + (e^{i(\delta k x_0^i - (\delta \omega)t - \delta \phi_i)}) (1 + \sum_{m=1}^N i \eta_{i,m} (a_m e^{-i\omega_m t} + a_m^\dagger e^{i\omega_m t})) \sigma_-^i]
\end{aligned} \tag{3.16}$$

where i is an index summed over N ions, and m is an index summed over N modes (for a linear chain of ions confined in an harmonic trap, there are N modes per axis [36], as we shall see in 4.2.1. ω_m is the frequency of the m^{th} x direction mode, and now $\eta_{i,m} = \delta k q_{i,m} / \sqrt{2}$, where $q_{i,m} = b_{i,m} \sqrt{\frac{\hbar}{M \omega_m}}$ and $b_{i,m}$ is the normalized matrix of ion displacements for ion i due to mode m , as described in 4.2.1.

We will be applying two global, symmetrically detuned from carrier beats, so

we now sum equation 3.16 over two beatnotes $\pm\delta\omega$:

$$H_I = \frac{\hbar}{2} \sum_i^N (1 - \sum_m^N i\eta_{i,m} (a_m e^{-i\omega_m t} + a_m^\dagger e^{i\omega_m t})) \Omega_i [e^{-i(\delta k^R x_0^i - \delta\omega t - \delta\phi_i^R)} + e^{-i(\delta k^B x_0^i - \delta\omega t - \delta\phi_i^B)}] \sigma_+^i + h.c. \quad (3.17)$$

Where $\delta k^{R(B)}, \delta\phi^{R(B)}$ refer to the wavevector and phase difference for the two beams tuned to the red (blue) of carrier. Distributing the evolving coordinate and temporarily dropping the terms that go as $e^{i(\omega_m + \delta\omega)t}$ to simplify the equations we are left with

$$H_I = \frac{\hbar}{2} \sum_i^N \sum_m^N \eta_{i,m} (a_m e^{-i(\omega_m - \delta\omega)t} e^{-i(\delta k^R x_0^i - \delta\phi_i^R)} + a_m^\dagger e^{-i(\omega_m - \delta\omega)t} e^{-i(\delta k^B x_0^i - \delta\phi_i^B)}) \Omega_i \sigma_+^i + h.c. \quad (3.18)$$

which can be more concisely written as ²

$$H_I = \frac{\hbar}{2} \sum_i^N \sum_m^N \Omega_i \eta_{i,m} (a_m e^{i(\omega_m - \delta\omega)t - i\phi_m^i} + a_m^\dagger e^{-i(\omega_m - \delta\omega)t + i\phi_m^i}) \Omega_i \sigma_{\phi_s^i}^i + h.c. \quad (3.19)$$

where $\phi_m^i = (\delta k^R x_0^i - \Delta\phi_i^R - \delta k^B x_{0,i} + \Delta\phi_i^B)/2$ is the phase of the force on the i^{th} spin, $\phi_s^i = -(\delta k^R x_0^i - \Delta\phi_i^R + \delta k^B x_{0,i} - \Delta\phi_i^B)/2$ is the spin phase of the i^{th} spin and $\sigma_{\phi_s^i}^i = \sigma_+^i e^{-i\phi_s^i} + \sigma_-^i e^{-i\phi_s^i}$

In our experimental setup the wavevectors of the BSB and RSB are counter oriented, i.e. $\vec{\delta k}^R \approx -\vec{\delta k}^B$, causing the spin phase to be insensitive to beam path length fluctuations. As both follow the same path, any fluctuation will cause equal and opposite phase change in both, i.e. $\delta\phi_s^i = -(\delta k^R + \delta k^B)x_0^i/2 = 0$

²The interested reader is welcome to compare this to the special case of 2 ions presented in [32]

Although the Hamiltonian above can create displacements in phase space while coupling to the ion spins, we are only interested in driving transitions where motion is only weakly excited and can be ignored. This happens when the beatnotes are sufficiently far from the side-bands so to not drive them off-resonantly, i.e. $\eta\Omega \ll \omega_m - \delta\omega$. This is known as the “slow” Mølmer-Sørensen gate [3, 33].

Applying 1.26 to 3.19, we will get many terms, however, we can observe that there are three types of commutators that could possibly contribute to the effective Hamiltonian:

1. Same mode, same ion
2. Same mode, different ions
3. Different modes, different ions

Assuming we set the spin phase so that we only have spin operators in the x-basis, only the second option contributes to the effective Hamiltonian.

1. $[a_n\sigma^i, a_n^\dagger\sigma^i] = a_n\sigma^i a_n^\dagger\sigma^i - a_n^\dagger\sigma^i a_n\sigma^i = (\sigma^i)^2(a_n a_n^\dagger - a_n^\dagger a_n) = I$ So this term does not effect the effective Hamiltonian.
2. $[a_n\sigma^i, a_n^\dagger\sigma^j] = a_n\sigma^i a_n^\dagger\sigma^j - a_n^\dagger\sigma^j a_n\sigma^i = \sigma^i\sigma^j(a_n a_n^\dagger - a_n^\dagger a_n) = \sigma^i\sigma^j$
3. $[a_n\sigma^i, a_m^\dagger\sigma^j] = a_n\sigma^i a_m^\dagger\sigma^j - a_m^\dagger\sigma^j a_n\sigma^i = 0$

Thus, the resulting effective Hamiltonian is (here I am including the terms evolving at $\delta\omega + \omega_m$ previously omitted)

$$H_{MS} = \frac{\hbar}{4} \sum_{i,j,m} \left(\frac{\Omega_i \Omega_j \eta_{i,m} \eta_{i,m}}{\delta\omega + \omega_m} + \frac{\Omega_i \Omega_j \eta_{i,m} \eta_{i,m}}{\delta\omega - \omega_m} \right) e^{-i\phi_{m,i}} e^{-i\phi_{m,j}} \sigma^i \sigma^j = \quad (3.20)$$

$$H_{MS} = \frac{\hbar}{2} \sum_{i,j,m} \frac{\Omega_i \Omega_j \eta_{i,m} \eta_{j,m} \omega_m}{\delta\omega^2 - \omega_m^2} e^{-i\phi_{m,i}} e^{-i\phi_{m,j}} \sigma^i \sigma^j \quad (3.21)$$

which we can write succinctly as $H_{MS} = \sum_{i,j} J_{i,j} \sigma^i \sigma^j$ where

$$J_{i,j} = \frac{\hbar}{2} \sum_m \frac{\Omega_i \Omega_j \eta_{i,m} \eta_{j,m} \omega_m}{\delta\omega^2 - \omega_m^2} e^{-i\phi_{m,i}} e^{-i\phi_{m,j}} \quad (3.22)$$

is the coupling strength between spin i and spin j . For the duration of this work, the relative modulation phase will be assumed to be equal for all ions, and will only be meaningful when compared to other force generating lasers. This is due to the ions being addressed with global beams, and the modulation frequencies in the MHz regime have phase fronts that do not significantly change over the length of the ion chain, that is no longer than $\sim 30 \mu\text{m}$.

This assumption will change in chapter 8, where individual phase control for each ion will allow us to control the relative sign of spin-spin couplings.

3.5 Conclusion

In this chapter all the necessary components for creating the simulated or effective components of the Hamiltonians we will investigate numerically and experimentally in 6 have been introduced and succinctly explained. When we simulate these Hamiltonians we will be adding in several frequencies to create both spin-spin interactions as in 3.21 and single spin simulated magnetic fields as in 3.5. The hidden assumption there is that combining the needed modulations of the light will

create an effective Hamiltonian that is a sum of the desired effective Hamiltonians. This is a valid assumption **only** if the beatnotes do not create cross terms with a low or stationary frequency in the effective Hamiltonian. For a more in depth treatment of the possible unwanted effects of this approach, see [\[37\]](#).

Chapter 4

Experimental Setup

4.1 Introduction

The experimental setup for the quantum simulation experiments reported in this thesis is highly complex. In fact, it is so complex that a single grad student starting from an empty lab would likely need more time just to set up part of the experiment, let alone perform any experiment, than an entire PhD program should reasonably require. The setup described here was luckily not started from scratch. The linear ion trap [2] was refurbished from its previous role as a Cadmium ion trap. We also greatly benefited from previous experience in the group [1, 38, 39] regarding how to use $^{171}\text{Yb}^+$. Control circuits for lasers and optical cavities, and the FPGA pulser were designed by authors mentioned in the citations above.

4.2 Ion trap

The type of ion trap we use for our experiment is the Paul ion trap [40]. As ions are electrically charged particles, we wish to create an electric potential with a stable minimum to which the ion will relax. Unfortunately, Earnshaw's theorem [41] informs us that a static electric potential cannot have a stable minimum. Paul's trap circumvents this problem by combining a static electric field and an oscillating

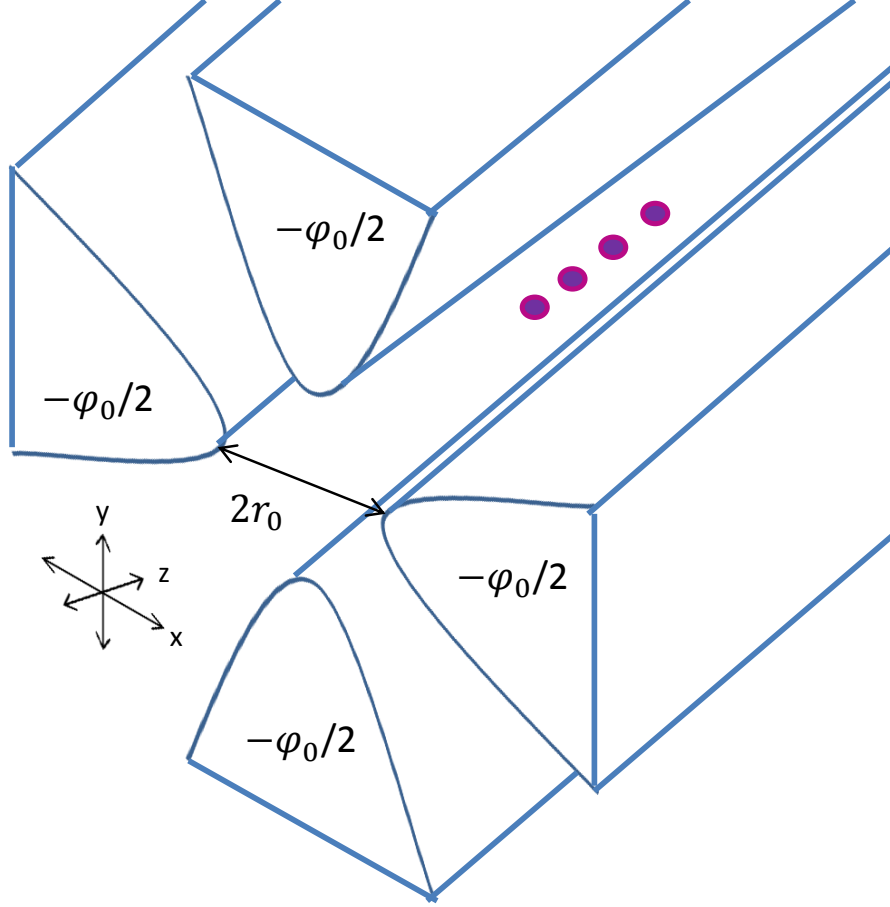


Figure 4.1: Paul trap with ions. the distance between hyperbolic electrodes is $2r_0$.

field to create a time-averaged pseudo-potential that has a stable minimum. The simplest example of such a setup is the four rod Paul trap, where the rods have a hyperbolic cross-section, as shown in figure 4.1.

In order to create a confining potential, we apply the voltage to the electrodes

$$-\phi_0 = U + V \cos(\omega t) \quad (4.1)$$

where U is a DC voltage and V is the amplitude of an RF voltage oscillating at frequency ω . r_0 is the distance from the electrode to the center of the trap, as shown

in figure 4.1. The resultant potential is

$$\phi = \frac{\phi_0}{2r_0^2}(x^2 - y^2) \quad (4.2)$$

After taking the gradient to find the electric field, we can write the equations of motion (known as the Matheiu equations):

$$\frac{dx^2}{d\tau^2} + (a + 2q\cos(2\tau))x = 0 \quad (4.3)$$

$$\frac{dy^2}{d\tau^2} - (a + 2q\cos(2\tau))y = 0 \quad (4.4)$$

where

$$a = \frac{4eU}{Mr_0^2\omega^2}, q = \frac{2eV}{Mr_0^2\omega^2}, \tau = \frac{\omega t}{2} \quad (4.5)$$

When the a and q parameters are chosen so that neither coordinate grows exponentially rather than oscillate, the ions are stably confined. The missing element of the confinement is in the z -direction, the trap axis (I will use this convention from here on out). That can be corrected for by simply adding a repulsive DC electrode to each end of the trap axis.

4.2.1 Normal Modes

A linear chain of N ions, trapped in a harmonic trap, experience a pseudo-potential due to an AC field, a static field and their electric charge[36]

$$V = \frac{M}{2} \sum_{n=1}^N \sum_{i=1}^3 \omega_i^2 x_{ni}^2 + \frac{e^2}{8\pi\epsilon_0} \sum_{\substack{n,m=1 \\ m \neq n}}^N \left[\sum_{i=1}^3 (x_{ni} - x_{mi})^2 \right]^{-1/2} \quad (4.6)$$

from which we can find their equilibrium positions in terms of a rescaled coordinate $u_m = x_m^0/l$, where x_m^0 is the small displacement from equilibrium defined by $x_{ni}(t) = \bar{x}_{ni} + x_{mi}^0$, and

$$l = \left(\frac{e^2}{4\pi\epsilon_0 M \omega_3^2} \right)^{1/3} \quad (4.7)$$

where e is the charge of the ion, M is the mass of a single ion, and ω_3 is the longitudinal collective center of mass frequency - the lowest normal mode frequency.

We can now consider the Lagrangian of the system,

$$L = T - V = \frac{M}{2} \sum_{n=1}^N \sum_{i=1}^3 (\dot{x}_{ni}^0)^2 - \frac{M}{2} \sum_{n=1}^N \sum_{i=1}^3 \omega_i^2 [\bar{x}_{ni} + x_{mi}^0]^2 - \frac{e^2}{8\pi\epsilon_0} \sum_{\substack{n,m=1 \\ m \neq n}}^N \left\{ \sum_{i=1}^3 [\bar{x}_{ni} + x_{ni}^0 - \bar{x}_{mi} - x_{mi}^0]^2 \right\}^{-1/2} \quad (4.8)$$

And expanding to lowest order, neglecting couplings between different spatial

directions¹

$$L \approx \frac{M}{2} \left\{ \sum_{n=1}^N (\dot{x}_{ni}^0)^2 - \omega_3^2 \sum_{m,n=1}^N A_{mn} x_{m3} x_{n3} + \sum_{i=1}^2 \left[\sum_{n=1}^N (\dot{x}_{ni}^0)^2 - \omega_3^2 \sum_{m,n=1}^N B_{mn} x_{m3} x_{n3} \right] \right\} \quad (4.9)$$

and

$$A_{mn} = \begin{cases} 1 + 2 \sum_{\substack{p=1 \\ p \neq m}} \frac{1}{|u_m - u_p|^3} & \text{if } m = n \\ \frac{-2}{|u_m - u_n|^3} & \text{if } m \neq n \end{cases} \quad (4.10)$$

$$B_{mn} = \left(\frac{1}{\epsilon^2} + \frac{1}{2} \right) \delta_{mn} - \frac{1}{2} A_{mn} \quad (4.11)$$

where **A** and **B** are the matrices for the longitudinal and transverse eigenvalue equations. We define the normal modes b_m that describe the oscillatory displacement of ion i from its equilibrium with longitudinal (transverse) frequency $\omega_z \sqrt{\mu_m}$ ($\omega_z \sqrt{\gamma_m}$)

$$\sum_{n=1}^N A_{mn} b_{i,n} = \mu_m b_{i,m} \quad (i = 1, \dots, N) \quad (4.12)$$

$$\sum_{n=1}^N B_{mn} b_{i,n} = \gamma_m b_{i,m} \quad (i = 1, \dots, N) \quad (4.13)$$

and assumed the collective transverse mode frequencies are equal. We define ϵ , the trap anisotropy

$$\omega_x = \frac{\omega_z}{\epsilon} \quad (4.14)$$

¹This is a valid assumption as long as the trap anisotropy parameter is small enough, i.e. the chain is not close to buckling from a linear chain into a zig-zag configuration.

where ω_x is the COM frequency for the x-direction transverse mode and ω_z is the COM frequency along the ion chain axis. The relationship between the axial and transverse normal-mode eigenvalues is

$$\gamma_p = 1/\epsilon^2 + 1/2 - \mu_p/2 \quad (4.15)$$

Transcribing this analysis into a Wolfram Mathematica script generates the ion equilibrium positions:

```

Δk =  $\sqrt{2} \frac{2\pi}{369.5 \cdot 10^{-9}}$ ;
NumofIons = 10;
ωcm = 2π4.863232 * 106;
ωtilt = 2π4.81294 * 106;
ε =  $\sqrt{1 - \frac{\omega_{\text{tilt}}^2}{\omega_{\text{cm}}^2}}$ ;
ωz = ε * ωcm;
l =  $\left( \frac{qe^2}{4\pi\epsilon_0 MYb171\omega_z^2} \right)^{1/3}$ ;
Table[uH[m], {m, NumofIons}]; (* create position variables *)
Table[fH[m] = uH[m] -  $\sum_{n=1}^{m-1} \frac{1}{(uH[m]-uH[n])^2}$  +  $\sum_{n=m+1}^{\text{NumofIons}} \frac{1}{(uH[m]-uH[n])^2}$ ,
{m, NumofIons}];
EqH = Table[fH[m] == 0, {m, NumofIons}]; (* generate coupled equations *)
IniH = Table[{uH[m], m/10}, {m, NumofIons}]; (* generate initial conditions *)
solH = FindRoot[EqH, IniH];
uHa = Table[uH[m]/.solH[[m]], {m, NumofIons}];
Print[uHa * l * 10^6, " position in microns of ions"]

```

And we get the ion distance on the z-axis from the center of the trap in μm for the trap parameters used in chapter 7:

```
{-10.0021,-7.31662,-5.05321,-2.97461,-0.982864,0.982864,2.97461,5.05321,7.31662,10.0021}
```

With these distances we can calculate the transverse frequencies for the x-direction, which we will be using to create our spin-spin interactions:

```

TMatrix =
Table [If [ $i \neq j$ ,  $\text{TransMat}[i, j] = \frac{1}{\text{Abs}[\text{uHa}[[i]] - \text{uHa}[[j]]]^3}$ ,
 $\text{TransMat}[i, j] = (1/\epsilon)^2 - \sum_{j=1}^{i-1} \frac{1}{\text{Abs}[\text{uHa}[[i]] - \text{uHa}[[j]]]^3} - \sum_{j=i+1}^{\text{Numoflons}} \frac{1}{\text{Abs}[\text{uHa}[[i]] - \text{uHa}[[j]]]^3}$ 
], {i, 1, Numoflons}, {j, 1, Numoflons}];
TransEigVal = Eigenvalues[TMatrix];
TransNormalFreq = Sqrt[TransEigVal];
Print [TransNormalFreq *  $\omega_z / 2 / \pi / 10^6$ , “ Trap frequencies in MHz”]
{4.86323, 4.81294, 4.74058, 4.64815, 4.53638, 4.40509, 4.25343, 4.07989, 3.88217, 3.65694}
Trap frequencies in MHz

```

The transverse frequencies displayed here run from the highest, the COM mode, to the lowest - the “zig-zag” mode, as shown in figure 4.2. The second highest mode is the “tilt” mode, and the spacing between COM and tilt, unlike any other two modes, is fixed at $\omega_2 = \omega_1 \sqrt{1 - \epsilon^2}$ (from here on the normal mode frequencies are referred to as ω_n , running from high to low). When generating the spin-spin coupling matrix **J** we will have flexibility in control of the form of the **J** by setting our detuning close to the mode that has the form similar to our desired couplings, as can be seen in figure 4.3. Using a single detuning will not give us complete control, however the modes form a complete basis, and we will use this in 8 to gain complete control over **J**.

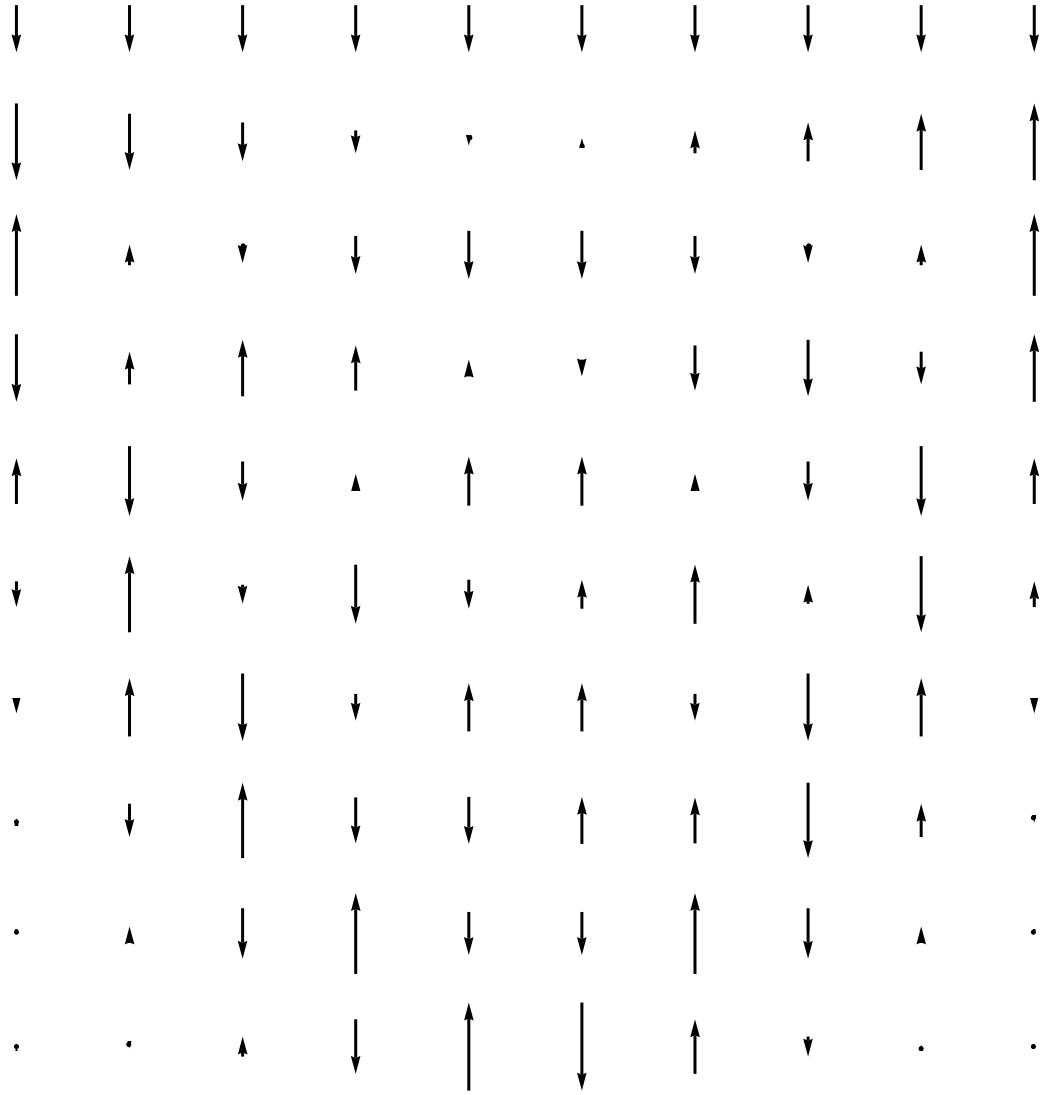


Figure 4.2: Transverse mode components for 10 ions. The arrows represent the maximum displacement of the ions from equilibrium while oscillating at mode frequency. The modes are ordered from highest frequency (COM) to lowest (zig-zag).

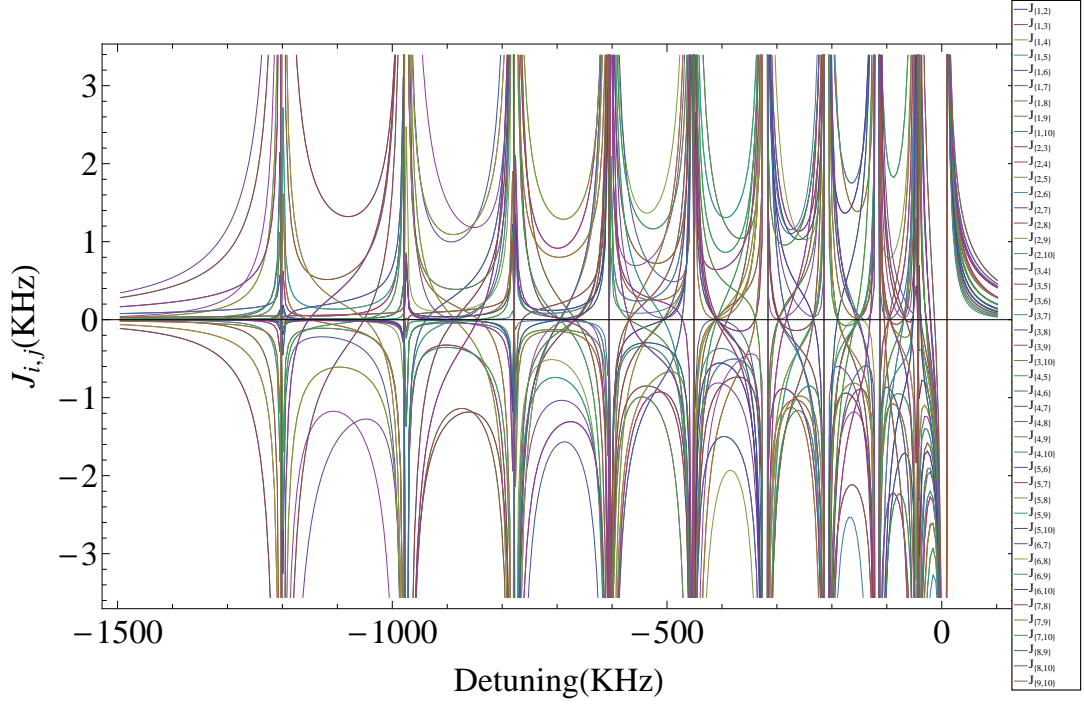


Figure 4.3: The mass of couplings for 10 ions. The x-axis is detuning in KHz from the COM. As can be seen in the plot, near the COM all the couplings are nearly equal, as can be expected from the form of b_1 . Near each mode the couplings diverge to infinity, however this behavior is non-physical as we must maintain the weak excitation of phonons condition.

4.3 Micromotion

In an actual trap, the alignment of the DC saddle point and the RF node will be imperfect. This will alter the form of the equations of motion adding an extra term of excess micromotion - oscillatory motion around the pseudopotential minimum, in addition to the inherent micromotion seen in [4.4](#).

This unwanted motion creates an oscillating Doppler shift on the ion's resonance frequencies, reducing scatter rates for cooling and detection and broadening the transitions. We have found that ions are less stable in the trap when this condition exists. To correct this condition, the DC voltages must be altered as changing the RF node is difficult (or impossible, as in our setup). There are several indicators useful for reducing the excess micromotion[\[42\]](#). One is measuring the Doppler cooling scattering linewidth. The second is measuring a correlation between the trap frequency phase and the scatter rate using a Time to Digital Converter. For micromotion along an axis parallel to an imaging device, one can also reduce V to see a displacement of the ion from DC saddle-point. In our trap we have found that it was very difficult to reduce micromotion, especially in the transverse direction not coupled to our gates (y), as reducing micromotion would rotate the trap axis, creating unwanted components of the Raman beams along the y axis. This would require us to change the incident angle of our Raman beams on the ion chain, which is quite difficult. Instead, we would reduce micromotion by maximizing the Rabi rate. It is likely that reducing the micromotion along the x -axis leads to more efficient Doppler cooling on that axis, leading to a higher Rabi frequency.

4.3.1 The Linear Trap

The trap used in the work in this thesis is of a different design than the one discussed above. It is constructed of three layers of thin alumina, with electrodes segmented by laser machining of the alumina and formed by gold coating, as shown in 4.4.

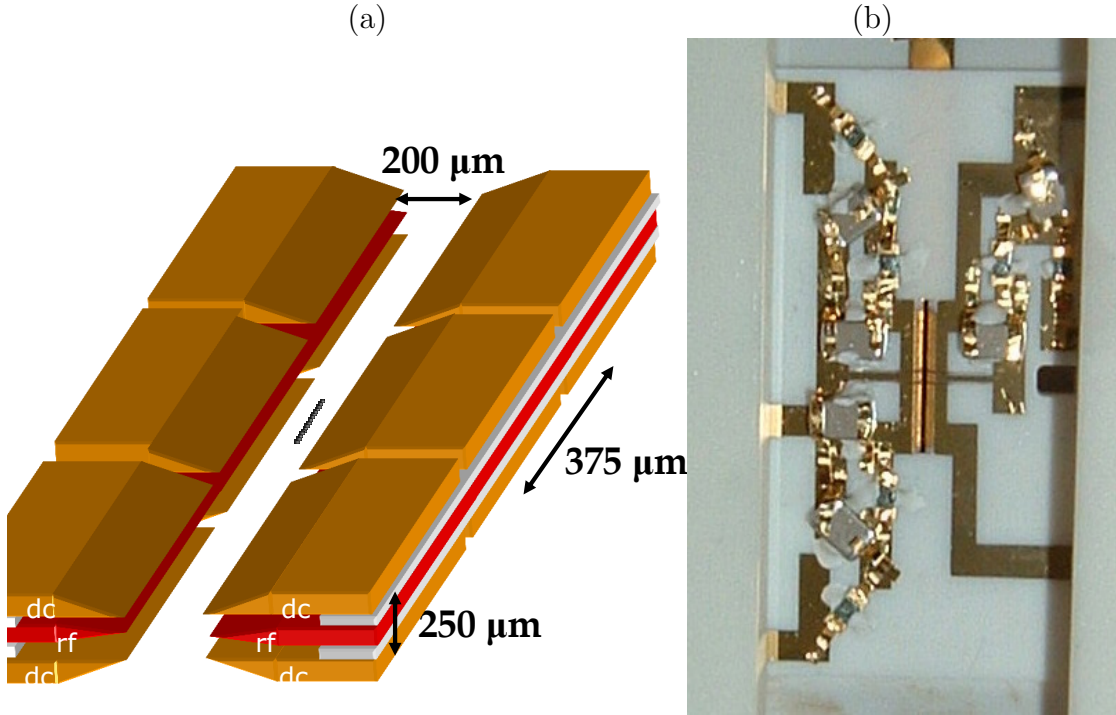


Figure 4.4: (a) Linear trap schematic with ions in trapping region. The RF electrode is a single electrode with a slit of equal dimensions to the DC electrodes central slit. The top and bottom DC layers are identical. (b) Linear trap photograph. Here the capacitors and resistors in a pi-filter configuration on the DC electrodes can be seen. These prevent capacitive RF signal coupling to the DC electrodes.

Although this configuration is quite different from that of the four rod configuration, the analysis is quite similar. As there is no easily found analytical solution for the potential generated by these boundary conditions, the approach we take is modeling the potential numerically with a commercial electromagnetic modeler -

Charged Particle Optics. For each electrode, we set all other electrodes to ground, and set said electrode to some voltage. Thus the linear combination of scaled potential maps gives us the total potential for the trap. Using this numerical solution, a ponderomotive psuedo-potential can be calculated

$$\psi = \frac{e^2}{4m\omega^2} \nabla V(x, y, z)^2 \quad (4.16)$$

and treating the linear trap as we would treat the hyperbolic Paul trap - a field exerting a harmonic restoring force on the ion, we find the secular frequency (the axial COM frequency) [43, 44, 45]

$$\omega_z^2 = \frac{e^2}{4m^2\omega^2} \frac{\partial^2}{\partial^2 z} (|\nabla V(x, y, z)|)^2 \quad (4.17)$$

Then the secular frequency of the trap is

$$\omega_z = \frac{e^2 V^2 \eta}{4\sqrt{2}m\omega^2 r^4} \frac{\partial^2}{\partial^2 z} \nabla (|V(x, y, z)|)^2 \quad (4.18)$$

which is the identical to the secular frequency of the hyperbolic trap, but with a redefined effective distance from the electrode to the ion r and a geometric factor η . This factor is the ratio between the quadrapole portion of the linear trap (or any other trap) to the oscillating term of the hyperbolic trap.

4.3.2 Trap Voltages and Control

As shown in 4.4(a), the trap has six electrodes on both of the DC layers. Wiring all electrodes would give more control than necessary to control the trap axis and minimize micromotion, and would increase significantly the difficulty of assembly and wiring. Therefore, only 3 DC electrodes in each layer are wired to external leads. The remaining three are wired to trap ground. These electrodes are wired to spot welded on board pi-filters. The leads running from these filters then connect to an external breakout box, which itself has additional pi-filters for each electrode, as discussed in 8.6. The trap voltages are supplied by an Iseg EHS-80-05XK3 high voltage module. This module is powered and controlled by an Iseg MPOD mini-crate. The crate provides a network based control of the voltages. The module has eight channels, all with SHV connectors. These are not to be confused with BNC connectors, which are very similar in appearance. We constructed custom cables to connect between the SHV connectors on the ISEG box to the BNC connectors on the breakout box.

It is important to note that the channels have a single polarity (dual polarity requires a floating ground that reduces stability)

- Channels 0-5: up to +500V /15mA
- Channels 6-7: down to -500V

The control program will automatically switch the driven channels from 4 and/or 5 to 6 and/or 7 if the set voltage on electrodes DC 3 and/or DC 4 is negative.

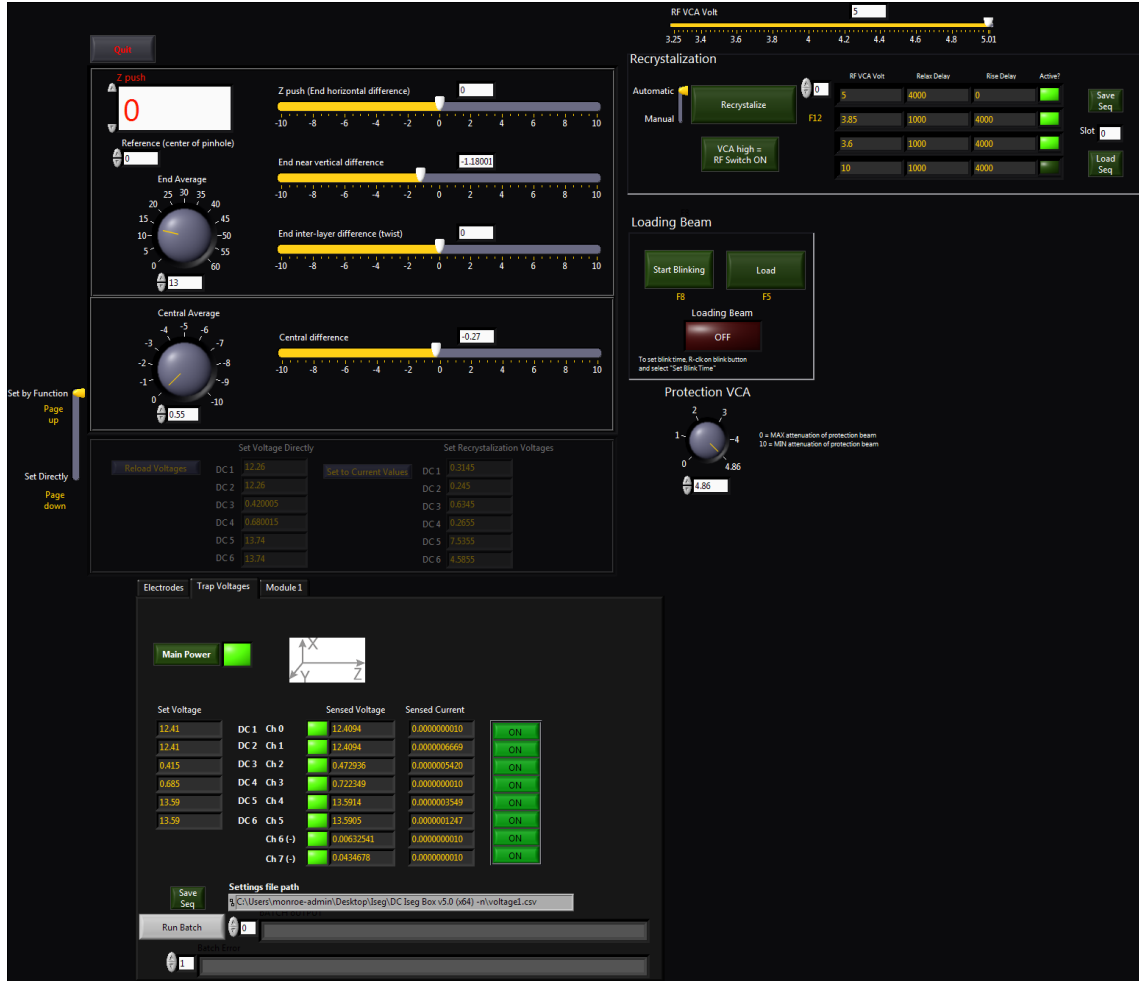


Figure 4.5: Trap control program. The upper right corner provided settings for a timed relaxation and tightening of the trap RF, via the LabJack controlled VCA. Upper right side controls the DC trap voltages. Lower half indicates sensed DC voltages and currents for tab displayed, as well as controls power to individual channels and the Iseg chasis (Main Power).

It is assumed the user has switched the cables on the breakout box if this is the case.

4.3.3 Oscillating Trap Voltage

The RF voltage V is provided via a helical RF resonator [46]. This resonator has a quality factor Q of ≈ 300 and is resonant at 38.86 MHz. As the power delivered through the resonator is changed, the ohmic losses change and the equilibrium temperature of the resonator and perhaps the trap itself changes. This leads to geometric changes that change the resonant frequency of the resonator and the RF voltage of the trap. As this leads to a change in the secular frequency of the ion, we have implemented a stabilization scheme. The first stage of this stabilization scheme is thermal stabilization of the RF resonator. This is accomplished by a Thorlabs TC200 Heater controller. This heater senses the temperature of the resonator using a thermistor, and stabilizes with a resistive coil. The stabilization is improved by insulating the resonator and the thermal feedback system with an adhesive foam with a reflective aluminum layer. We find that this temperature is stable to less than a degree when the set point temperature is 25°C , slightly above room temperature.

The second stage of this stabilization scheme is active frequency stabilization of the HP-8640B driving the trap RF to resonance. This helps stabilize the delivered power. It is helpful, but not sufficient, to stabilize the trap transverse modes.

We pass the driving RF through a Minicircuits BDC ZFBDC-62HPS bidirectional coupler, and mix the reflected signal with a phase shifted reference signal

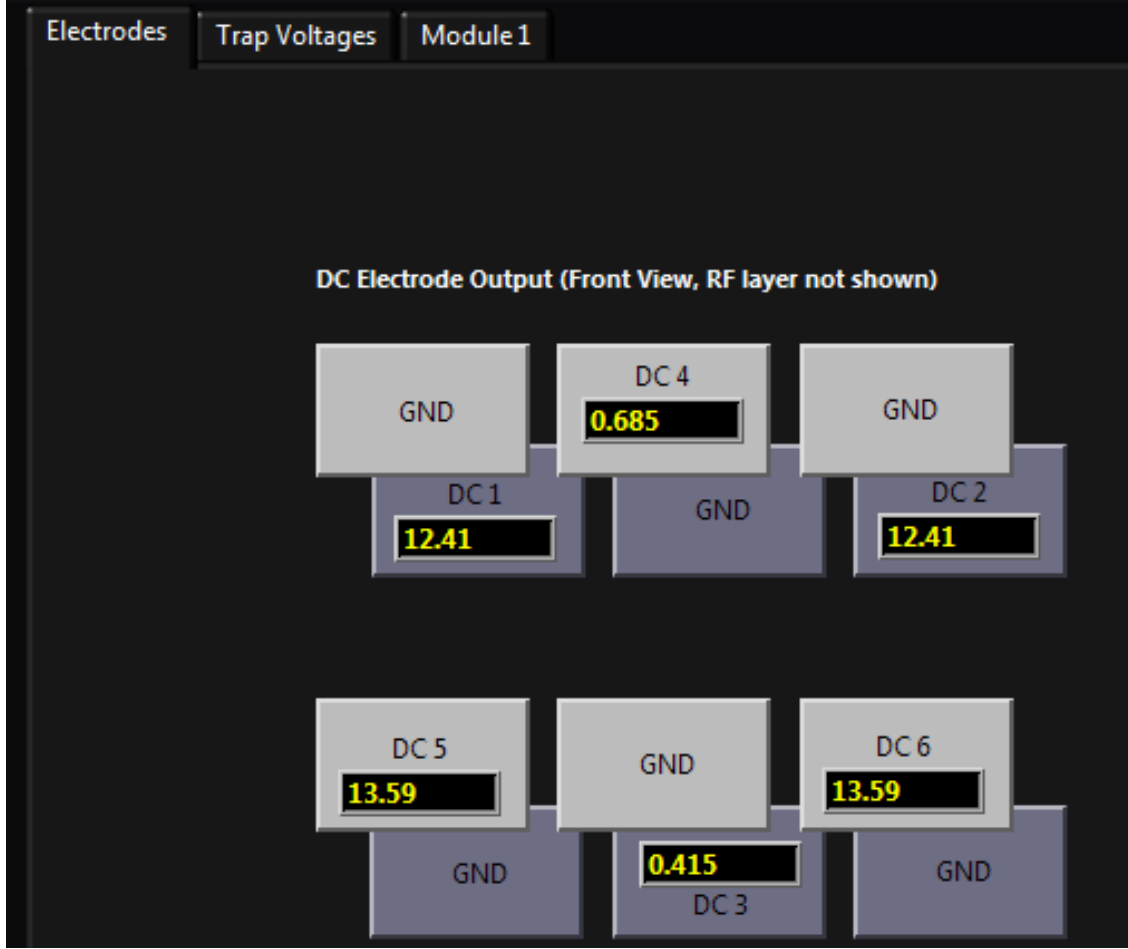


Figure 4.6: Trap control program electrodes tab. Here the sensed voltages on each electrode are displayed. The electrodes are displayed without the RF layer, facing towards the imaging optics. The electrodes labeled 'GND' are grounded.

from the HP-8640B (this signal is impedance matched by passing through a 50 MHz low-pass filter) frequency generator providing the driving signal (which is amplified to $\approx 26dBm$). The phase is adjusted using a potentiometer providing a set-point voltage to a Minicircuits JSPHS-51+ narrow band phase shifter (this component must be selected carefully for the resonant driving frequency of the trap). This mixed signal is low pass filtered so only the DC component remains, and is fed back as a DC frequency shift to the driving 8640B (typical modulation peak of 320KHz).

4.4 Optical Setup

4.4.1 Ionization

There are three lasers used for excitation of the neutral Yb, ionization, cooling, optical pumping, and detecting. These are all DL-100 Toptica lasers - temperature and current controlled laser diodes. Aligning the diode with a reflection from an external optical grating allows for mostly single mode selectivity for the modes selected by the diode cavity. In general, once the grating is aligned to generate a frequency in the neighborhood of the desired frequency (for the minimal lasing threshold current) frequency adjustment should be done by adjusting the grating angle and diode current. If mode hopping occurs, then one may try a sensitive adjustment of the diode temperature.

As discussed in 2.1, it is necessary to excite the neutral ^{171}Yb before it may be ionized by a 369 nm or 355 nm beam. As the beam exiting the laser has an elliptical profile, we first circularize the beam with a prism pair. Next we protect the laser from back reflections from any of the downstream optical elements, as these create unwanted optical cavities with the laser and unnecessary mode hopping (this is true for all the lasers in this experiment except the Vanguard). A mechanical shutter controlled by the trap control program exposes or conceals the trap to the beam, which after passing through the final lens is roughly $50\,\mu\text{m}$ vertically and $100\,\mu\text{m}$ horizontally, at roughly 2mW . When the $^{171}\text{Yb}^+$ oven is driven at 2.3A after warming up for about a minute, the light intensity is powerful enough to load an ion roughly every 10s when using the Raman beams for ionization of the excited

Yb. This is achieved with good isotopic selectivity: the ^{171}Yb oven is roughly 90% pure, but loading unwanted isotopes occurs less frequently than 10%. As the oven is perpendicular to the excitation beam, the atoms do not experience a doppler shift with a thermal distribution.

The desired frequency of the excitation beam is 751.527640 MHz , however we do not lock this laser, rather we tune it to the desired frequency and load before it drifts too far off resonance. The rate of frequency drift depends on the temperature of the room and how long the laser has been operating at given temperature and current settings. The laser takes roughly an hour to equilibrate.

4.4.2 935 nm Repump

The 935 nm laser providing the repump light discussed in [2](#) is provided by a DL-100 as well. As this light is needed to repump both the F=1 and F=2 manifolds of the $^3D_{3/2}$ state, the 320.56922 THz carrier is modulated by an EOSpace fiber EOM at 3.07 GHz .

This laser is only stabilized for long timescales, by a feedback signal to its grating angle provided by a software PID. This PID generates a feedback signal based on the frequency difference between the laser wavelength, measured by a HighFinesse wavemeter via optical fiber and a software controlled set point. The wavemeter accuracy may drift by up to 20 MHz , depending on room temperature, and is calibrated to our iodine spectroscopy setup, discussed below. Its precision is roughly a MHz .

4.4.3 638 nm Repump

As discussed in 2, repumping the ion from the long lived but unlikely $^2F_{7/2}$ state requires two close frequencies of 638.61 nm light. As this light is not often required, and when it is required the ion chain has likely decrystallized (from a collision) and data taking cannot immediately continue, the laser is only stabilized by the HighFinesse wavemeter (~ 5 MHz short time scale stability). To provide both wavelengths of 638.6103 nm and 638.6151 nm, the PID feedback to the laser grating setpoint is alternated between the two desired wavelengths, once every minute. DL-100 laser is first passed through a prism pair to circularize the beam profile, and then coupled into a fiber optic. The output of the fiber is directed at the ion chain with several mW and a large waist at the ion chain, so careful alignment is not required.

4.4.4 Cooling, Pumping, and Detecting with 369 nm

To generate the 369 nm light we require, we use a MBR-110 from Coherent. This is a tunable Continuous Wave (CW) Ti:Sapphire laser, pumped by a Coherent 18W 532 nm Verdi-V18. It outputs roughly 1.5W at our desired wavelength of 739.052526 nm. The MBR-110 is made of a single block of aluminum, and is thus passively stable. The bow tie configuration passes through an optical diode that prevents backward reflections. The wavelength of the laser is selected by controlling the gain profile for multiple laser mode selecting elements. These include the laser cavity length, an etalon (that oscillates around a rotation angle at 80 KHz to gener-

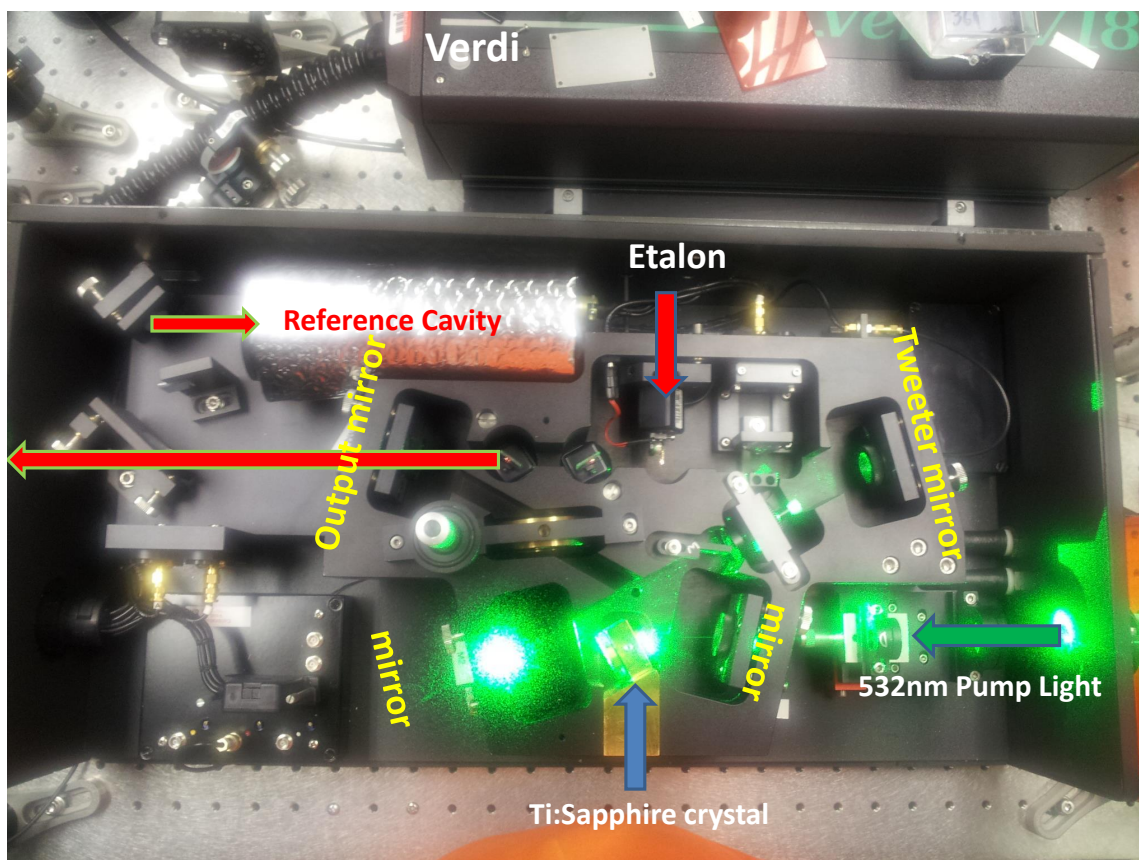


Figure 4.7: The MBR-110 laser.

ate an error signal used to lock its angle to the laser cavity length), and a birefringent filter (with a wavelength dependent response). The Free Spectral Range (FSR) of a bow-tie cavity is $FSR = \frac{c}{L}$ where L is the length of the cavity. As the largest cavity is the laser itself, the mode-hop free frequency range tuning and locking is controlled by laser cavity length ($\frac{c}{L} = 300 \text{ MHz}$). The laser has a linewidth of $\sim 75 \text{ KHz}$.

The 739nm output power of the MBR-110 is fiber coupled into a high power fiber, except $\sim 100mW$ that is fiber coupled to the wavemeter, and $\sim 40mW$ to an EOSpace fiber EOM, used for the iodine lock, described in section 4.4.5. The high power fiber delivers 800mW to a WaveTrain frequency doubler, as shown in figure 4.8.

After exiting the doubler the beam is 430MHz red detuned from resonance. It is divided in three, by a piece of glass. The front surface reflection is modulated by an New Focus EOM driven at 2.105GHz to provide the optical pumping, and is shuttered by an AOM that up shifts the beam by 424 MHz, into resonance with the transitions discussed in 2.2. This beam is then combined with the detection beam before being fiber coupled. The back surface reflection is modulated by an EOM driven at 7.374GHz. It is then passed through a Brimrose AOM. The first order diffracted beam is up shifted by 400MHz and used for cooling (30 MHz detuned from resonance). The zeroth order is used as a “protection beam”. This powerful beam is used to recrystallize the ion chain when a decrystallization is detected by the cooling light scatter PMT. As it is modulated for cooling, it is resonant with both the $^2S_{1/2} |F = 1\rangle$ and $^2S_{1/2} |F = 0\rangle$ to $^2P_{1/2}$ transition, and we have found this to improve the speed and probability of recovering all the ions. The transmission

through the glass is used as the “protection” beam, which is shuttered by an Intra-Action AOM and further red detuned by 200 MHz. This beam is more powerful than the three other beams, but does not cool both transitions as the previous beam. All three beams are coupled into optical fibers to reduce unwanted scatter light in the direction of the first order beam. This scatter was found to limit coherence time in long experiments. The added benefit is clean laser modes and ease of aligning and overlapping the beams.

A small portion of the transmission is siphoned off by a beam splitter, to be shuttered and shifted into resonance by a Brimrose AOM. The “protection+” beam was combined with the 399 nm beam in order to simplify alignment. Unfortunately, we have found that overlap is difficult and the 399 nm beam alignment drifts wildly from day to day due the need to change the laser grating angle and the long beam path to the chamber. Therefore, alignment with the cooling or protection beam at the ion position does not allow perfect overlap along the entire beam path. Before entering the chamber window, the detection, cooling and protection beams are horizontally stretched by cylindrical lenses, and then focused at the ion chain to a horizontal beam waist of $\sim 100\ \mu\text{m}$. However, as shown in figure 4.9, the beams enter the chamber at 45° to the ion chain, giving an effective beam width at the chain of $\sim 150\ \mu\text{m}$. This gives a roughly equal detection beam profile across our ion chain, that for 16 ions is $26\ \mu\text{m}$ for our current operating parameters for the ion trap.

As our beam profiles are roughly Gaussian, the beam dimensions and power are limiting factors on the detection homogeneity. As the power in the beam is limited,

handling longer ion chains with optimal exposure and detection beam powers for all ions requires a larger horizontal beam profiles. In order to achieve this with a fixed laser power, we are required to squeeze the vertical beam waist. This leads to more stringent requirements on beam alignment, and more noise on the effective laser power at ions, due to beam steering by air turbulence. Currently, with our detection beam vertical waist of $\sim 10\ \mu\text{m}$ this is not a limiting factor on our detection error, rather we suffer from power fluctuations of $\sim 5\%$. In order to remedy this issue we are currently investigating the use of a feedback stabilization system (“noise eater”). In fact, it is questionable if we can widen the beam much more without increasing background scatter from the trap off the imaging window into the imaging optics. A possible remedy is to create a beam with a “top hat” profile using diffractive optics, and thus avoid wasted beam power in the wings of the beam and ensure equal detection conditions for all the ions.

Note: for some of the earlier results reported in [6](#), we used the MBR-110 to drive the Raman transition, and a Toptica TA-100 amplified diode laser to drive all resonant transitions. In that setup, we only generated $\sim 200\text{ mW}$ of 739 nm light and suffered as a result for larger numbers of ions. The TA-100 was locked using the iodine spectroscopy setup described in [4.4.5](#). The major difference is the use of a home built confocal cavity, that was locked by length to the transition, and the use of a Pound-Drever-Hall feedback signal to lock the laser frequency to the cavity length. This feedback signal was separated into a low ($< 100\text{ KHz}$) component that controls the laser grating angle, and a high frequency component ($> 10\text{ MHz}$) for the laser diode current, controlled via a Bias-T [\[47\]](#).

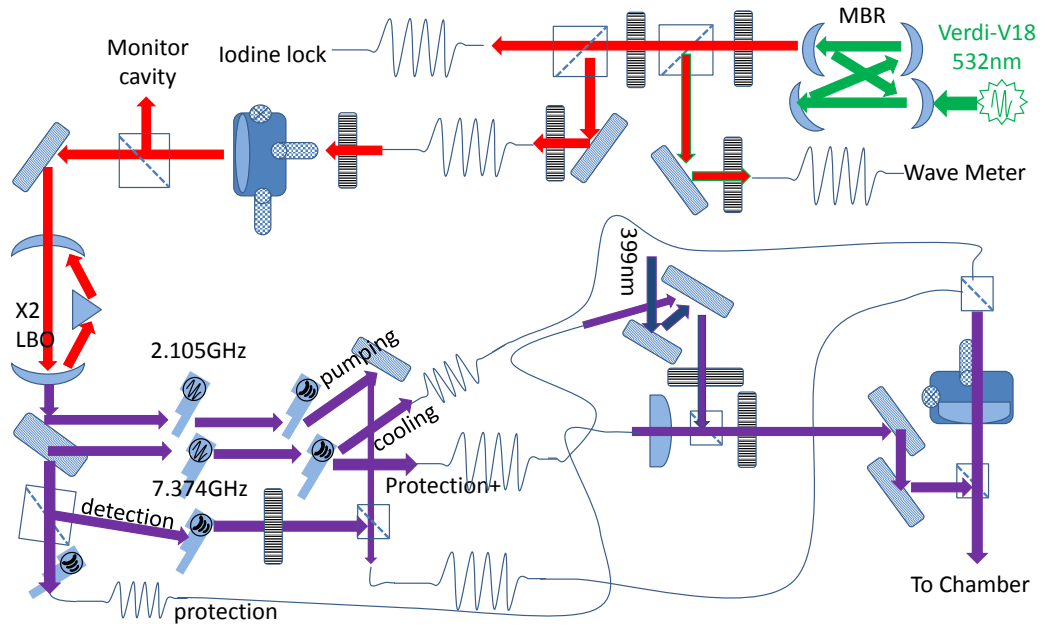


Figure 4.8: A schematic diagram of our 369 nm and (399 nm excitation for neutral Yb) optical setup. The final cylindrical lens, mounted on a micrometer positioning stage, is a vertical lens with focus 150 mm. The micrometer is used for aligning the vertical direction of the detection beam, which is the most sensitive. Chamber is shown in fig 4.9

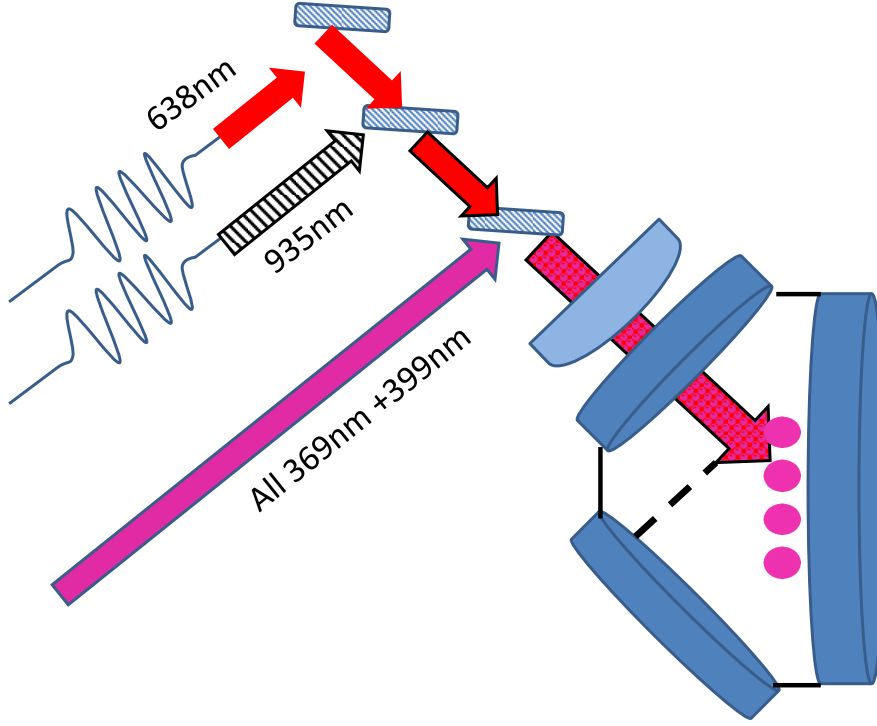


Figure 4.9: A schematic diagram of chamber and final stage of resonant beams. The cylindrical lens the beam pass through focuses the vertical direction of the beams, with an 80 mm focal length. It demagnifies the intermediate focus by 5. The dashed line represents the rough trajectory of the high purity $\sim 90\%^{171}\text{Yb}$ oven. As it is perpendicular to the excitaiton beam, our ability to selectively load the desired isotope (rather than the impurities) is higher than the purity of the oven. Although the beams exit through the front view port, from which the ions' state detection flourescence is collected, the 638 nm , 935 nm and roomlight do not create unwanted signals on the ICCD or PMT as they are filtered. As the waists of these beams is large at the ions, alignment requirements are lax.

4.4.5 Iodine Spectroscopy Lock

As the linewidth of the S-P transition is 20 MHz , we must stabilize the laser on long time scales to a much narrower center frequency to have consistent detection and cooling. This is accomplished using a spectroscopic feature of iodine narrower than our linewidth, to which an external cavity (part of the MBR-110 laser) is stabilized. An optical fiber carrying 40 mW of the MBR-110 output is coupled into a fiber EOM, modulated at 13.315 GHz , so that the first order sideband of this modulation (~ 4 mW) excites the iodine transition of interest[47, 1].

Three beams are derived from the fiber - a reference beam directed at the Nirvana Auto-Balanced Photoreceiver, a probe beam which is sent through the iodine cell and out into the signal photodiode of the Nirvana, and a pump beam transmitted through an 80 MHz Neos AOM into the iodine cell, overlapping with the probe. The iodine cell is insulated with fiberglass and aluminum foil, and heated to 500°C . This excites the higher energy rovibrational states of the iodine molecules and strengthen the absorption signal. A cold finger maintains the pressure in the cell and prevents pressure broadening of the transitions [48]. The Nirvana detector is designed to subtract the reference from the signal, thus making it a sensitive detector able to remove 50dB of noise. We have encountered two major problems with this setup:

- Background light from the pump beam can leak onto the signal photodiode.

As this background light level can drift, the detector fails to subtract the noise.

- The Nirvana detector is designed to balance the attenuation of the photodi-

odes. However, we have witnessed that it is limited in this ability. As the reference beam is much more intense than the probe beam, it must be attenuated for the detector to work properly.

The 80 MHz modulation of the pump beam is itself modulated at 10 KHz , enabling the use of a lock-in-amplifier to demodulate and amplify the Nirvana error-signal (the derivative of the Doppler free hyperfine transitions in iodine). As there are two strong transitions for the above EOM frequency near to the resonant laser frequency (for the 739 nm , non-doubled light), there will be three error-signal peaks. We stabilize the MBR-110 to the peak corresponding to the highest frequency of the three at 405.644321 THz , which is ~ 20 MHz above the nearest feature. This can lead to confusion, as the wavemeter displaying the laser frequency drifts in the same range. However, the incorrect frequency is close enough to the desired one that ions will in fact be visible on the ICCD if this occurs - but they will appear dim.

We route the error-signal from the lock-in-amplifier to a home built PID. The PID output is then routed to the MBR-110 External Lock Input. I have connected an attenuator to this input, as **it cannot take an input larger than 10V**. This signal is fed to the piezo controlling the length of the MBR-110 external reference cavity (an internal component of the laser, as shown in figure 4.7). The piezo mounted tweeter mirror of the laser locks the length of the laser cavity to the external cavity length. This lock can be stable on long time scales to ~ 2 MHz , which is sufficient for the linewidths at hand.

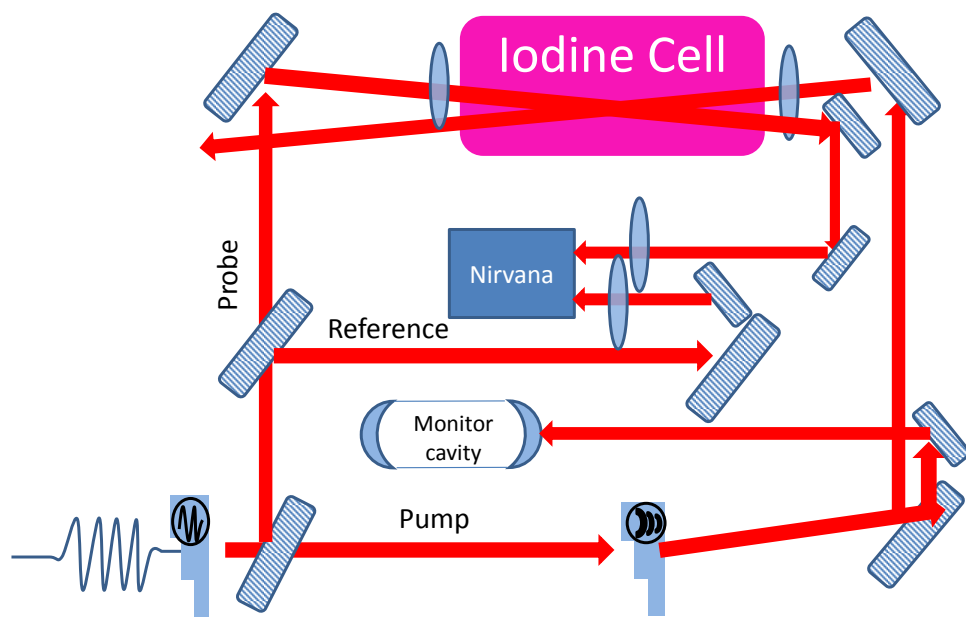


Figure 4.10: Schematic of iodine setup. The angle between the beams in the cell is exaggerated.

4.4.6 Vanguard 355 nm Laser

The Vanguard Diode Pumped Solid State Laser is intended to be a turn key laser. The lasing medium is a Nd:YVO₄ crystal (Neodymium Doped Yttrium Orthovanadate) pumped by a solid state diode lasing 12W of 808 nm through a 19 core fiber bundle. The crystal (“oscillator”) should then lase roughly 5W at 1064 nm . Unfortunately, we are currently overdriving the oscillator to 6W, for reasons to be explained below. The output of the oscillator is then amplified by another Nd:YVO₄ crystal, pumped by two 20W 808 nm diodes, to roughly 20W of 1064 nm laser light. This light impinges on a Second Harmonic Generator (SHG) that produces an 8W beam of 532 nm . A semiconductor saturable absorber reflector mode-locks the laser at 80 MHz , where the pulses have a 10 ps duration [49]. This mirror has a reflection that decreases with increasing light intensity, thereby allowing the creation of laser pulses at high gain.

The 1064 nm and 532 nm beams are mixed on a Third Harmonic Generator (THG) to produce the desired 355 nm light. Although Spectra-Physics is not willing to disclose this information, the SHG and THG are likely type 2 Lithium triborate crystals [50, 49]. The output of the laser according to its specifications should be 4W, as in figure 4.11. Unfortunately, the power we observe is lower and it is dropping, as the laser is old and bought second-hand. The laser is controlled by a desktop computer via serial connection, using the control program MLUV. After initial warm-up (~ 30 min), the power of the laser and its stability may be optimized. As the components of the laser are old, the built in optimization function of MLUV

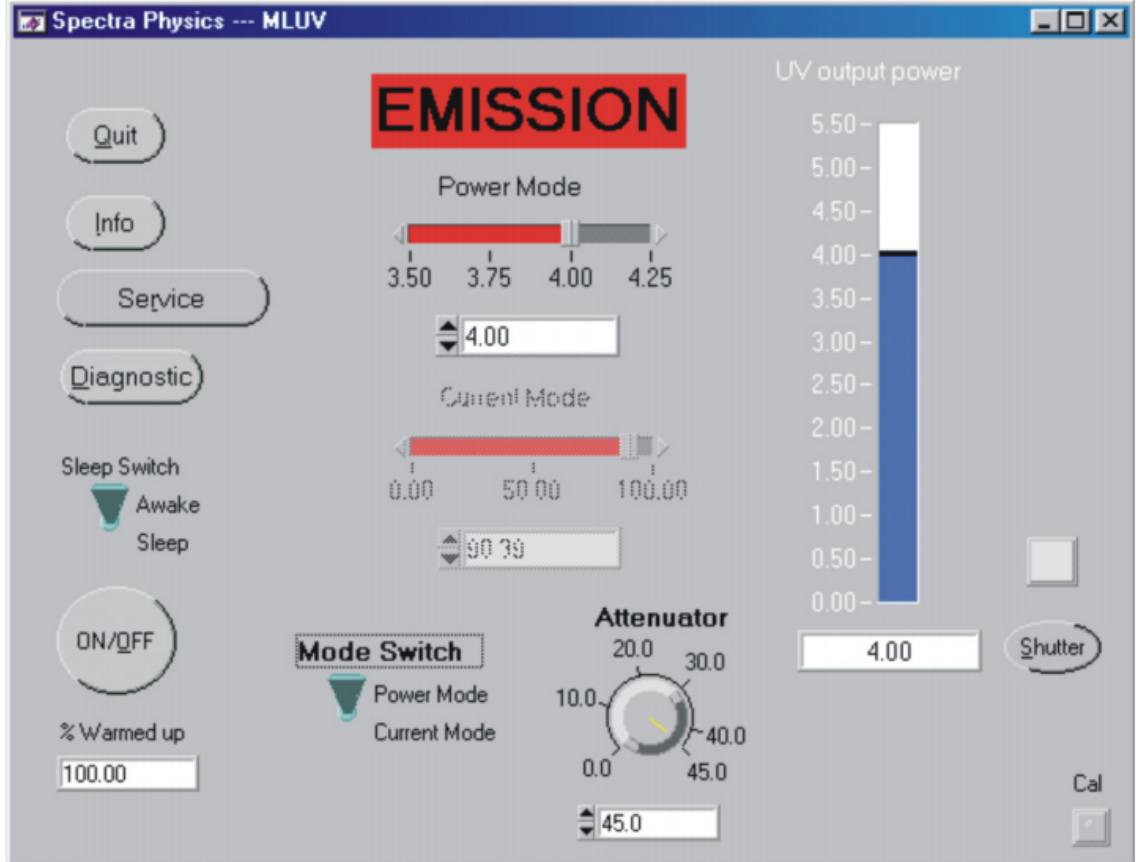


Figure 4.11: MLUV main control window. The laser has two operating modes: one where the laser power is stabilized and one where the diode currents are stabilized. In order to run in power stabilization mode there must be some disposable power. As our power is low, we typically run in current stabilization mode. Although we have not found the power to be less stable in this mode on the short time scale, the overall power is slowly dropping.

does not work.

The initial optimization should focus on the diode currents and temperatures. Lowering diode currents can surprisingly increase power. Usually the most sensitive parameter is the current to “Diode 1”, the oscillator pump, as shown in 4.12. These settings can only be changed when the laser is operating in Current Mode. If this procedure fails to raise the power back to its expected level, the next set of parameters to tweak are the amplifier pump diodes currents and temperatures, as

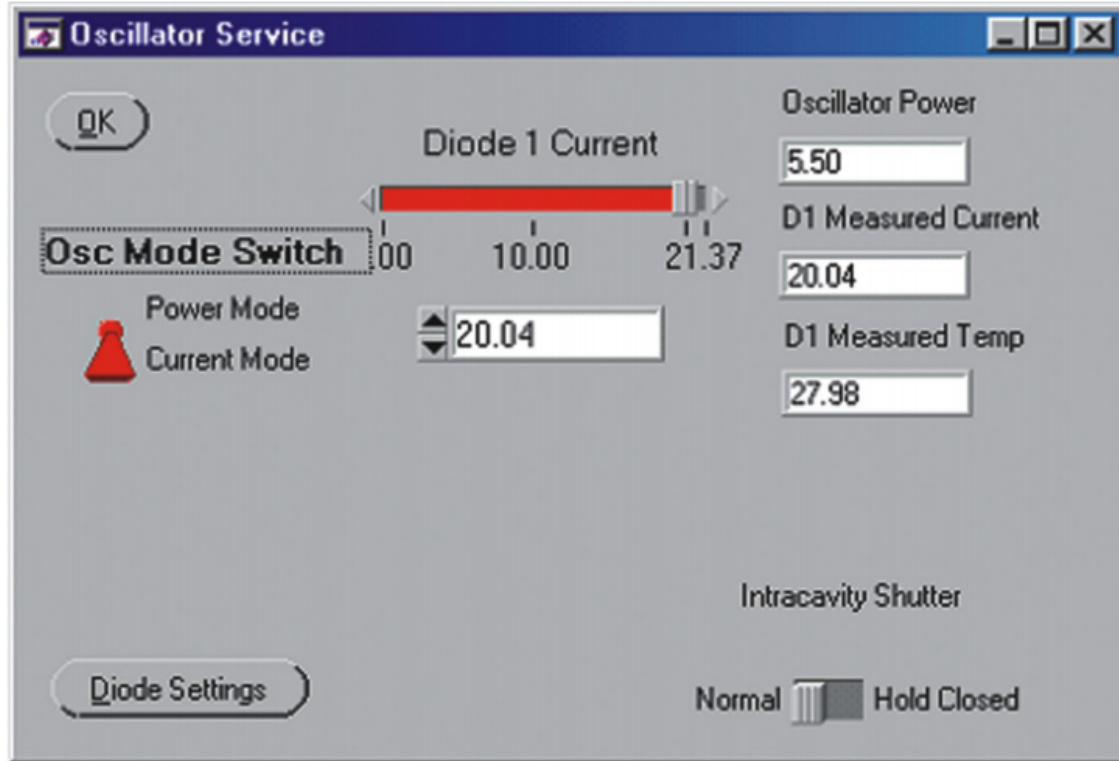


Figure 4.12: MLUV oscillator pump current control.

shown in 4.13. If these parameters yet again fail to raise the laser power, then it may be attempted to change the oven temperatures of the SHG and THG, as shown in figure 4.14. This is a slow process, as each change must be given time to equilibrate. Each change on the fine knob (roughly in steps of five units) should be given at least 2 minutes to assess the effect. If this attempt fails as well, then there is a possibility that the THG and/or the SHG have degraded at the current laser path. It may be necessary to move the THG or SHG. This may be done via MLUV for the SHG and only for the x-direction for the THG, as shown in 4.15. If all the X positions on the THG for a Y position have been degraded, then the Y position may be manually changed via two screws that lock into 6 different orientations, via a side panel on the Vanguard. Both screws must be set to the same position, otherwise vertical beam



Figure 4.13: MLUV amplifier pump current control. In this figure the individual current controls are grayed out as the mode has not been set to individual diode control.

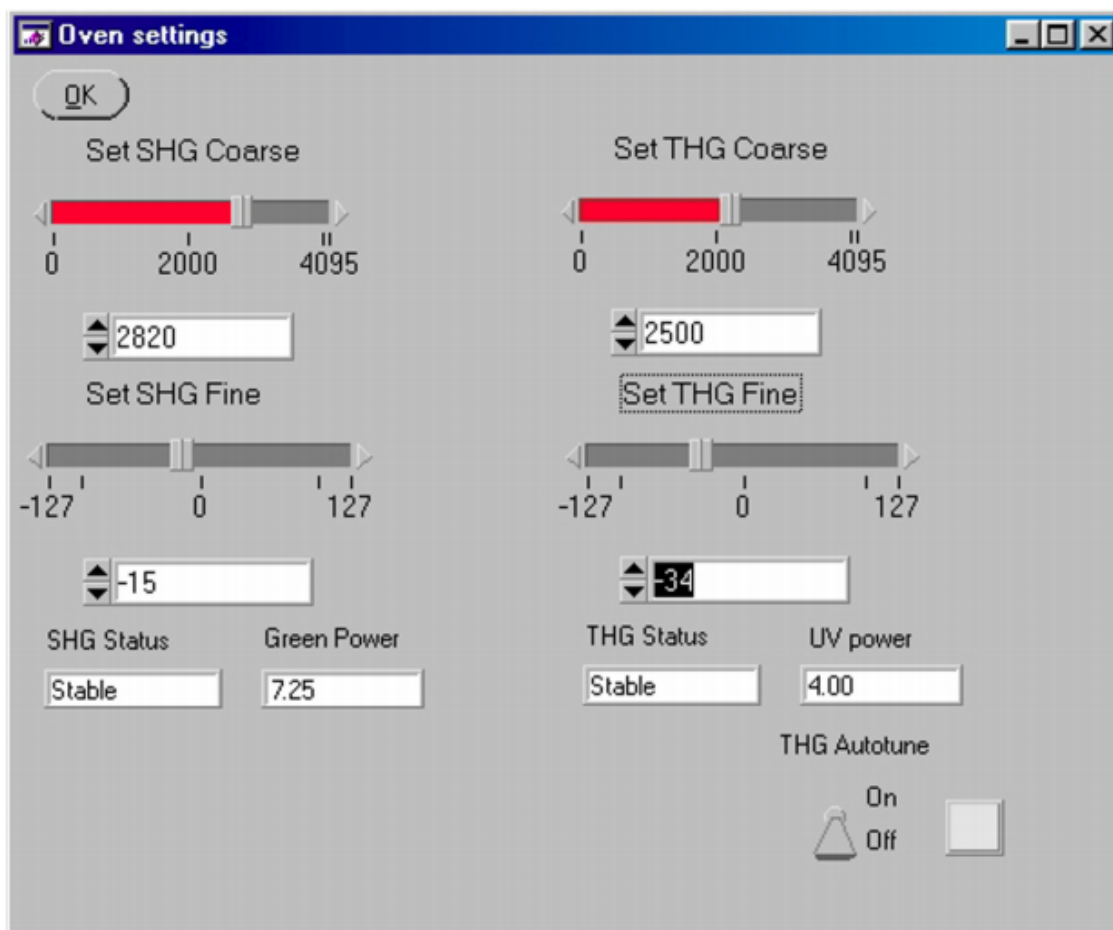


Figure 4.14: Control window for THG and SHG oven temperatures. The fine tuning settings should be used first.

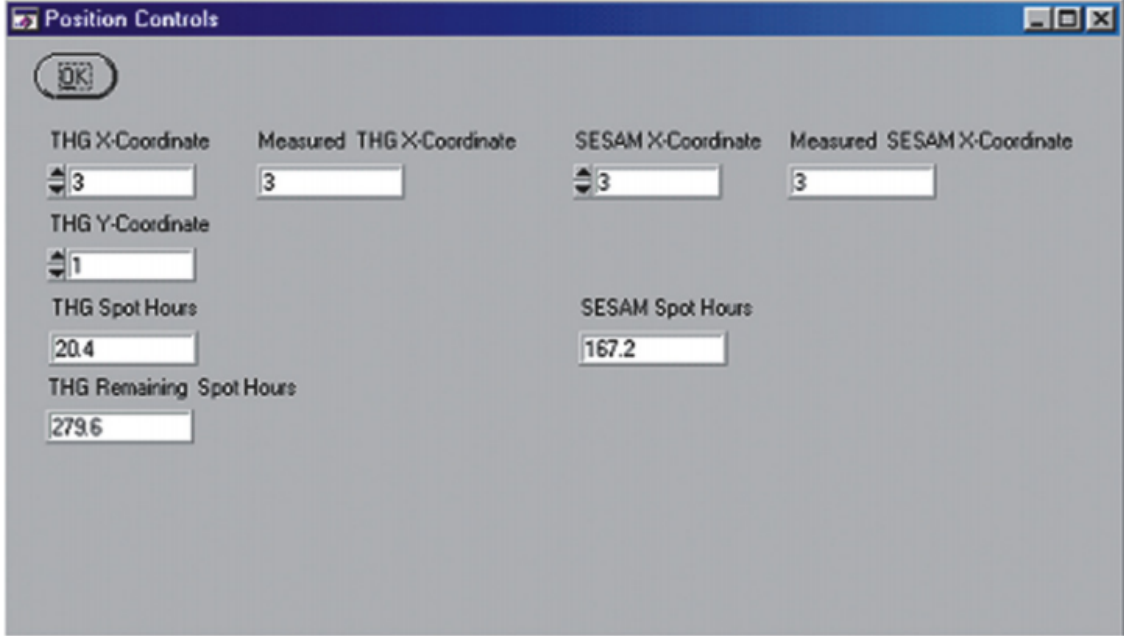


Figure 4.15: MLUV position controls for the SHG and THG. The THG Y-position is only for record keeping - MLUV does not control it.

steering will result.

Although the methods above have worked in the past to raise the laser power, the power has been dropping constantly and can not be recovered (the experiments in chapters 6 and 7 have been performed with powers ranging from 3.7W to 3.4W). This is likely due to the degrading of the amplifier pump diodes.

4.4.7 Driving Raman and Mølmer-Sørensen Transitions with the Vanguard

In 3 we discussed how spin-spin couplings can be created using global beams modulated to drive virtual transitions in the phonon subspace while driving real spin transitions. In the work reported here, this theoretical treatment is realized with the Vanguard DPSS. Although this is a pulsed laser, we will be operating in the weak

pulse regime - each pulse pair radiating the ion will contribute a small change to the ion state (also referred to as the weak pulse regime). Thus we will be able to treat the pulse trains as CW lasers [51]. In order to generate the desired beat frequencies, we will interfere the pulses on the ions, absorbing a photon from one frequency component of the pulse train and emitting into another. The beam exiting the laser will be split into two arms, and both arms will be modulated by AOMS. This will give us control of the beat frequency difference, as schematically represented in figure 4.16. For this scheme, the absolute frequency offset and the absolute phase of the pulse train of each pulse train will have no effect[51]. We can choose to subtract or add the frequency difference between AOMs. The beat frequency of interest between teeth in the two offset combs is $(80.6(n + 157) + AOM2) - (80.6n + AOM1) = 80.6 \times 157 + \Delta_{AOM} = 12654 \text{ MHz} - 12 = 12642 \text{ MHz}$, which drives the carrier.

A prerequisite for this scheme is an acceptable and stable laser pulse repetition frequency. Our qubit splitting is fixed at 12.6428 GHz . As shown in figure 4.17, the 532 nm output of the Vanguard (attenuators not shown) is measured by a Electro-Optics ET-4000 fast photodiode. The output of this photodiode is band pass filtered by a tunable mechanical microwave filter so that only the frequency component close to the qubit splitting is transmitted. This signal is amplified and mixed with a microwave frequency source, allowing us to feed forward a frequency offset to AOM1, thus stabilizing the frequency difference between the Raman arms.

An acceptable frequency must satisfy two conditions:

1. It may not drive the carrier transition with just one arm, nor the Zeeman

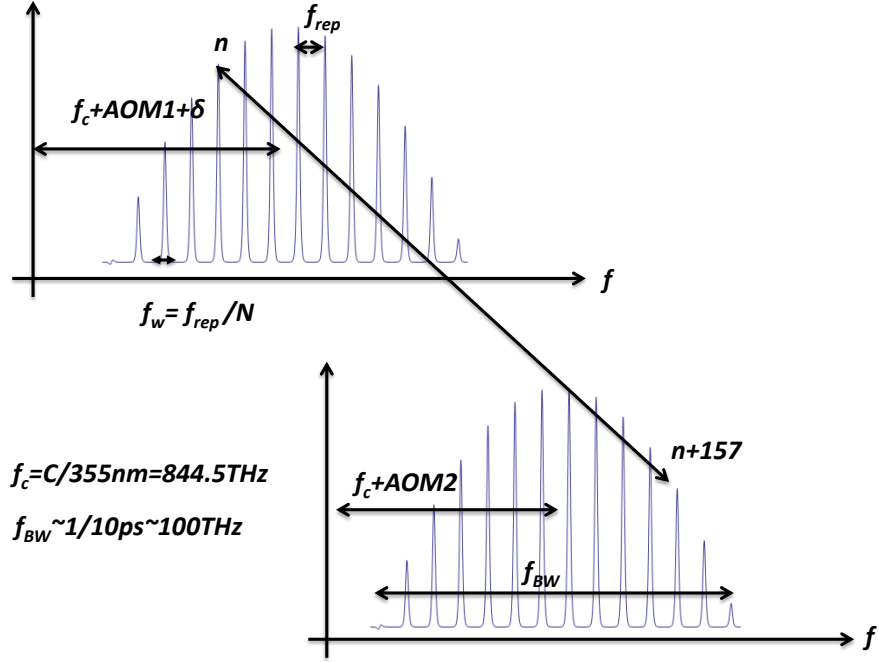
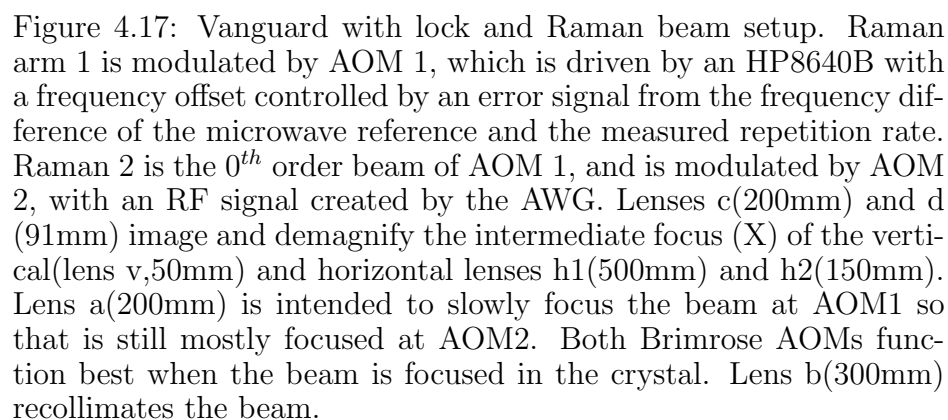


Figure 4.16: Two pulse trains interfering at the ions represented in frequency space. The two AOMs shift the frequency combs, and allow us to control the beat frequency. AOM1 modulates at $\sim 225 \text{ MHz} + \delta$, where δ is a fed forward frequency offset to stabilize the beat frequency. AOM2 modulates at $\sim 213 \text{ MHz}$ when we drive the carrier transition (and a more complex waveform with multiple frequencies for the simulation). The frequency of difference of $\sim 13 \text{ MHz}$ is subtracted from the beat of the teeth. The pulse width in frequency space is $\frac{1}{N f_{rep}}$, where N is the number of pulses involved in a interaction.



carrier transition ($m_f = 0 \rightarrow m_f = \pm 1$) at roughly 7 MHz from carrier (depending on magnetic field strength).

2. It may not drive the Mølmer-Sørensen gate with both Raman beams on (but without the requisite modulations) due to a beat note between the arms that is equally detuned to the blue and red from the carrier.

As the pulse width is ~ 10 ps, the bandwidth of the laser is ~ 100 GHz. With a repetition rate of 80 MHz, that indicates 1180 comb lines in the frequency domain. Enforcing these parameters and above conditions, with the more stringent requirement that the rate not lie between carrier and Zeeman transition, the following Mathematica code reports allowed repetition frequencies :

```
ranges = Table[frep, {n, 1, 1180}];
For[n = 1, n ≤ 1180, n++,
ranges[[n]] = Reduce[{frep * n/2 < (12642.8199 + 7) && frep * n/2
> 12642.8199 - 7 && frep < 81 && frep > 79}]]
ranges = DeleteCases[ranges, False]
```

And the the frequency ranges of the repetition rate f_{rep} that satisfy the conditions for the possible values between 79 and 81 MHz are reduced to: $\{80.9988 < f_{rep} < 81., 80.7401 < f_{rep} < 80.8295, 80.4829 < f_{rep} < 80.5721, 80.2274 < f_{rep} < 80.3163, 79.9735 < f_{rep} < 80.0622, 79.7213 < f_{rep} < 79.8096, 79.4706 < f_{rep} < 79.5586, 79.2214 < f_{rep} < 79.3092, 79. < f_{rep} < 79.0614\}$

Our Vanguard has a measured rep rate of 80.6 MHz, which seems to be just outside one of the permissible ranges (there is no way to control this for this laser, as it depends on laser cavity length that cannot be adjusted). The beat frequency

between two comb teeth separated by 157 teeth is closest to the qubit frequency: $f_{rep} \times 157 = 80.6 \times 157 = 12654.2 \text{ MHz}$. Our fastest Rabi transitions driven by the Vanguard have been measured to be $\sim 1 \text{ MHz}$, which implies the number of pulses needed per Rabi cycle is at least 80. Therefore the width of a comb tooth is no more than 1 MHz when we drive Rabi transitions at full power, and $\sim 1 \text{ KHz}$ for Mølmer-Sørensen transitions at our typical transition strength. Another consequence of the 10 ps pulse width is that pulse is 3mm long in space. As the pulses must overlap at the ion at the same time, we adjust the Raman2 arm using a beam cube, named in 4.17 as Mach-Zender (the setup is similar to a Mach-Zender interferometer as the ion measures the phase difference between the arms).

As we are utilizing long chains of ions, aligned along the z-axis of the trap (as illustrated in figure 4.18). We are also using global beams to address the entire ion chain at once. Therefore, the most power efficient beam shape is a sheet of light. To approximate this, we use two sets of cylindrical lenses, one vertical and one horizontal for each Raman arm. This allows us to compress the vertical beam waist down to $\sim 7 \mu\text{m}$ and the horizontal beam waist down to $70 \mu\text{m}$ (Raman2) and $200 \mu\text{m}$ (Raman1) at the ion. In order to measure these beam profiles, we position a mirror in the beam path before the ion, and image the beam at the estimated distance to the ion with a Guppy CCD, as in figure 4.19. Alternatively, one may place the Guppy at the intermediate focus (marked with an X in figure 4.17), and estimate the beam waists at the ion based on the demagnification of the telescope (roughly 1/4). It is important to note that the telescope for Raman2 images AOM2. As AOM2 is modulated by multiple frequencies, the deflection point in the AOM must

be imaged so as to refocus all frequencies at the ion chain (the AOM deflects with an angle $\sin^{-1}(\frac{m\lambda}{2\Xi})$, where m is the order of the deflected beam, λ the wavelength of light, and Ξ the sound wave wavelength).

This optical setup is far from ideal. The 0^{th} order beam of a driven AOM1 has a poor beam profile, and the power in the beam depends on how strongly AOM1 is driven, thus coupling the beam strengths of both arms. Also, the beam profile seems to be coupled to the imaging plane, and we were unsuccessful at changing the beam profile while maintaining the imaging plane at AOM2. This imaging has also been diagnosed by us to be imperfect, possibly leading to a Stark shift across the chain, that appears as a weak biasing axial field in quantum simulations. An additional issue in this setup is that Raman2 just barely grazes the objective, and has a reflection off the imaging view port that also passes very close to the objective, as seen in 4.17. This limits our possible numerical aperture (NA) to its current value, as discussed in 4.4.8.

4.4.8 Florescence Collection

The state detection via florescence, as discussed in 2.4 is achieved by collecting the spontaneous emission light at 369 nm from the ions using a microscope objective from CVI (UVO-20.0-10.0-355-532). This objective of NA 0.23 is situated roughly 3mm from the imaging port, and 13mm from the ion chain in effective optical distance, as illustrated in 4.20. This setup is very similar to that described in [52]. With an apex angle of 2θ , the solid angle $\Omega = 2\pi(1 - \cos\theta) = 2\pi(1 - \cos(\sin^{-1}NA)) =$

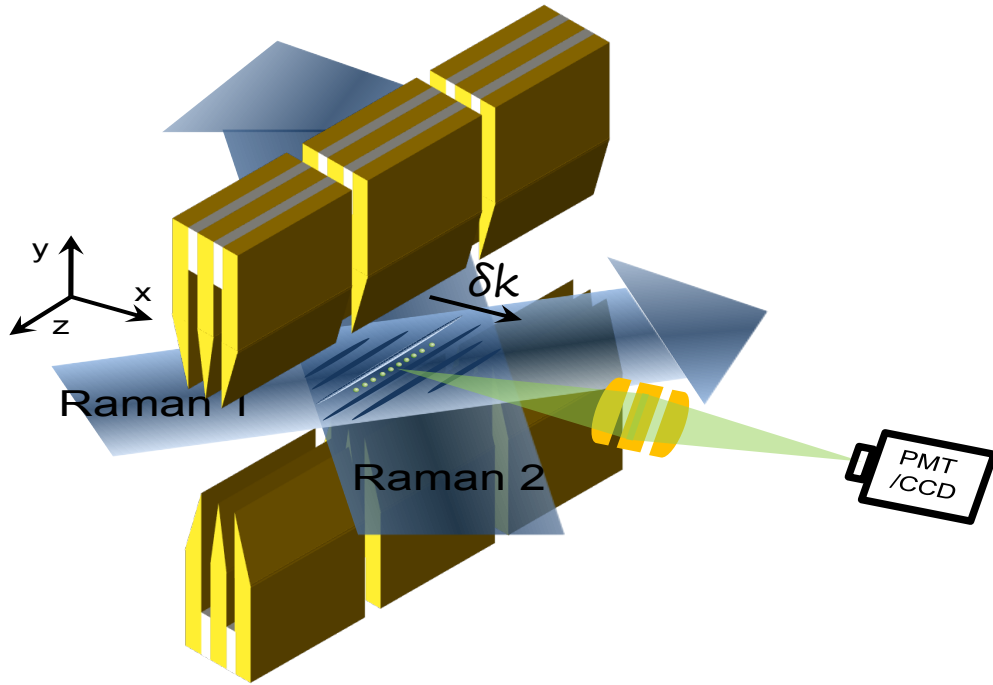


Figure 4.18: Schematic of ion trap apparatus and the geometry of Raman laser beams for the spin-dependent force. Two Raman beams uniformly address the ions, with δk along the transverse x -direction. The spin states are defined with respect to a magnetic field of ~ 5 G along the y -axis. A photomultiplier tube (PMT) and CCD camera are used to measure the spin state of each ion through standard spin-dependent fluorescence.

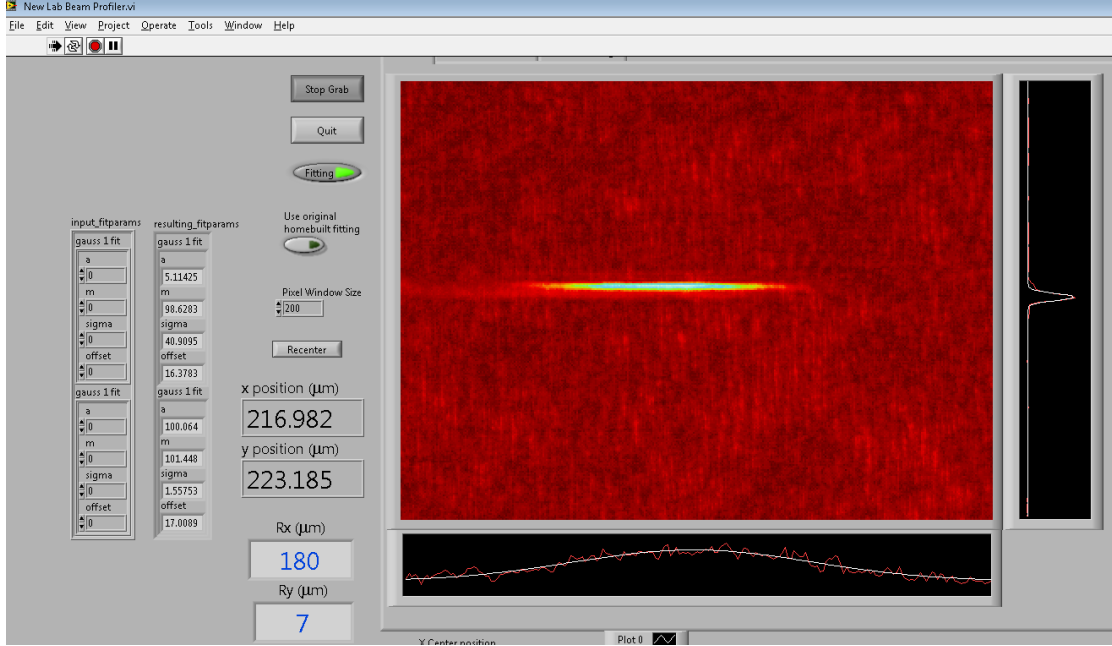


Figure 4.19: Profile of beam as taken with CCD at estimated ion distance. Our home built Labview program fits for the horizontal (wide) and vertical beam waists

0.168, i.e. only $\sim 1.3\%$ of the scattered light. The collected light then passes through a home built $\sim 400\mu\text{m}$ pinhole (a washer thinned by a mill and drilled through) at the image plane to reduce off axis background scatter. The image is further magnified by a doublet pair to $\times 130$ and filtered by a pair of Semrock filters (FF01-370/36-25 and Hg01-365-25) that transmit $\sim 95\%$ of the light at 369 nm, and block the other lasers and roomlight completely (unfortunately, they do not block 355 nm). The light is split into two paths - one for imaging, and one for cooling scatter collection. The latter is part of an automatic decrystallization detection scheme. The imaging path has two possible configurations - one where a flipper mirror diverts the light to the imaging PMT (Hamamatsu H10682-210), and one where the mirror is folded back and the image proceeds directly to the ICCD. The PMT beam path has a lens to demagnify the image, as long ion chain images are too

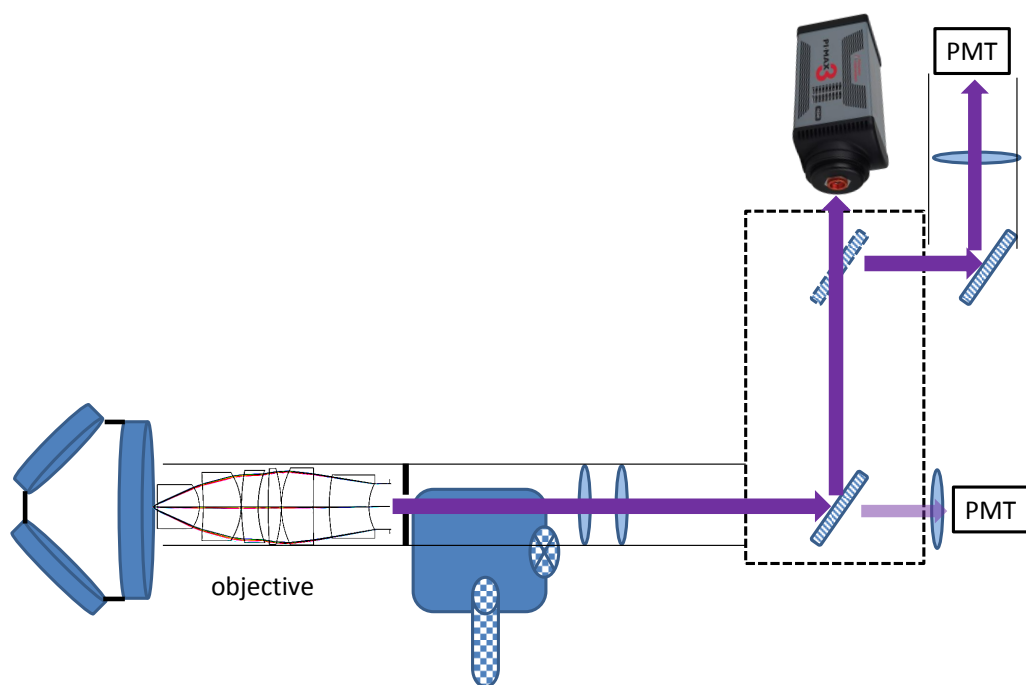


Figure 4.20: Objective collects $\sim 1.3\%$ of spontaneous emission from florescing ions. Then collected light passes through pinhole, double and filters(not shown) that are all mounted in lenstube atop a micrometer positioning stage for alignment. First PMT is for decrysalization detection. PMT or ICCD imaging is selected via remote-controlled flipper mirror, in box(dashed lines).



Figure 4.21: The averaged image of 1000 exposures of 10 bright ions. The pixels are binned in 4×64 super-pixels (hence the vertical compression). This image was produced by the script in appendix D for the data taken in 7.

large to fit the PMT aperture otherwise. In retrospect, we have overly magnified the image. The only advantage to magnification is ease of diagnosing the focus. As long as magnification is enough that adjacent ions do not overlap on the same ICCD pixels the magnification is sufficient. Magnifying beyond that point leads to using more pixels than necessary, slowing down readout, adding readout noise and limiting field of view. The binned image of 1000 3 ms exposures (produced by the script in appendix D) bright can be seen in figure 4.21.

As discussed in the 2.4, the PMT Quantum Efficiency (QE) is $\sim 30\%$ at 369 nm, and only 20% for the PiMax3:1024i “Super Blue”. When we detect the ion state with the PMT for $0.8 \mu\text{s}$, we collect on average 10 photons for a single bright ion, and this is sufficient for detection with 97% fidelity. Due to the lower QE and readout noise of the ICCD, we must use a longer exposure time of 3 ms for the same detection light power. In addition, we bin the 1024×1024 pixel CCD into 4×64 superpixels to reduce readout time and noise[53]. With our parameters the detection fidelity for a single ion on the ICCD is 95%. For our magnification and diffraction limit, the ion occupies a Gaussian circle of $250 \mu\text{m}$ on the ICCD (found from an unbinned $12.8 \times 12.8 \mu\text{m}$ pixel size) as seen in figure 4.22.

When collecting data via PMT during experiments we fit the histograms to simple Poissonians, with an average set by hand. When analyzing such data, we

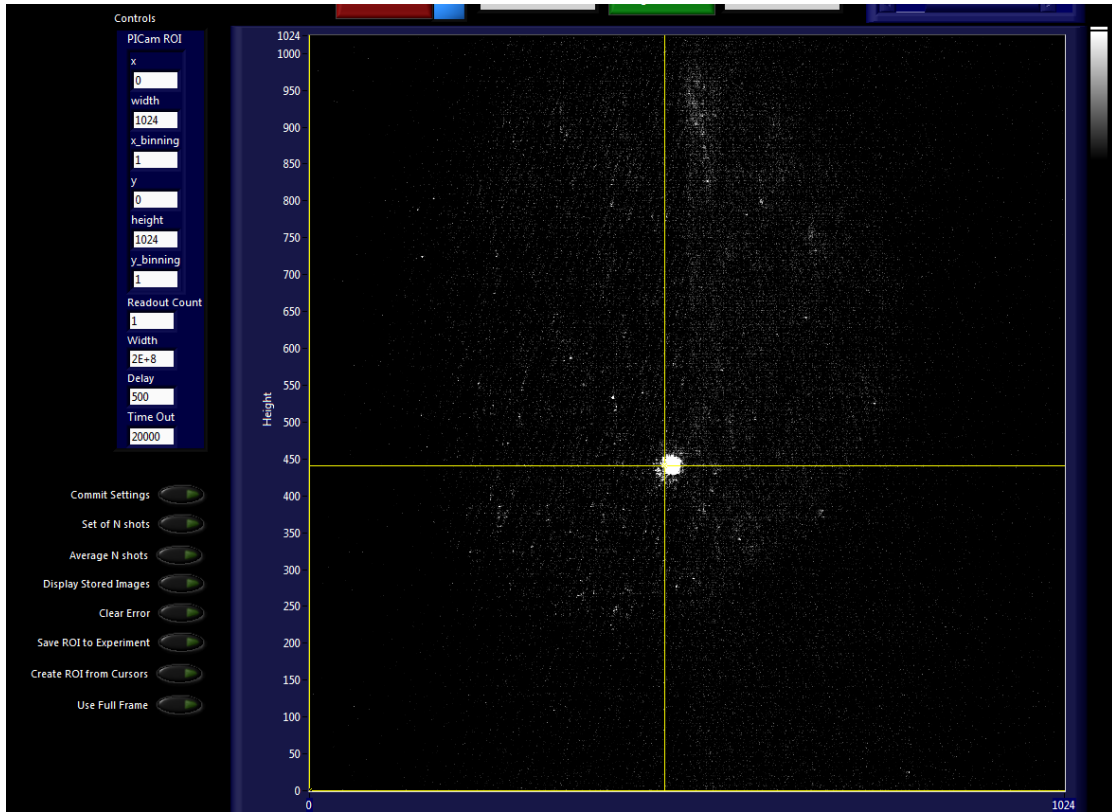


Figure 4.22: High resolution video still of single ion, taken from our control program. Airy ring is somewhat visible. Most of collected light is from cooling. The pinhole is barely visible, outlined by light scattered from the trap and view port.

refit the histograms with more realistic distributions[31]. When collecting data with the camera the treatment is more complex. For real time data taking, we collect 1000 images of the ions when they are pumped dark, followed by 1000 images of the ions rotated to bright by a Raman pulse. The bright images are then averaged, and the image discriminated into dark and bright pixels according to a preselected brightness cutoff. The bright pixels are used to find the Regions of Interest (ROI) for each ion. The brightness of the entire region of each shot is then analyzed to derive histograms for the dark and bright state for each ion. A discriminator that gives equal state detection error for both histograms is then determined. The ROIs and discriminators are then returned to the Labview control program to be used in real time state discrimination. The script is presented in appendix D.

Due to the spot size of the ions and their typical separation of $2\text{-}5\text{ }\mu\text{m}$, we suffer from cross talk. This can be seen in the results returned from the ROI script in table 4.1. Here we see that the detection error ϵ is lower at the center of the chain. This is due to the ions higher proximity at the center the chain. The spillover light from neighboring ions causes the bright histogram to be brighter and hence the lower overlap with the dark histogram seemingly reduces ϵ . To compensate for this cross talk and bias we post process our data. Using the same 1000×2 exposures used previously, we derive new histograms, this time by fitting Gaussians centered at each ion to vertically summed data, as in figure 4.23. By counting frequency of the Gaussian fitted amplitudes, we construct a histogram that accounts for ion cross talk as the fit is found for the entire ICCD width with fixed Gaussian waists and centers. Although this process discards one spatial dimension of the images, it does

Y_1	Y_2	X_1	X_2	ϵ	Discriminator
1	5	45	48	7.	10650
1	5	56	59	5.	10650
1	5	65	69	4.9	14450
1	5	74	78	4.7	14350
1	5	82	86	4.3	14600
1	5	90	93	4.9	11100
1	5	98	102	4.8	14850
1	5	107	110	4.7	11300
1	5	116	120	4.6	14800
1	5	127	131	6.	14600

Table 4.1: ROIs and detection error % ϵ for 10 ions, as returned by the script in appendix D for the 10 ion data in 7.

not have much of an affect on the discrimination between signal and background, as there is severe vertical image smearing at our ICCD clock speed setting (16 MHz).

We further enhance our data by correcting for state bias due to the detection error [54]. We construct the matrix \mathbf{M} that describes the distortion of the probabilities for N ions of each real spin state g_i into the detected probability for spin state

$$f_j = \sum_{i=1}^{2^N} M_{ji} g_i$$

$$M_{ji} = (1 - p_0)^{n_0 - \alpha} (1 - p_0)^{n_1 - \beta} p_0^\alpha p_1^\beta \quad (4.19)$$

Where p_0 the error probability for one dark ion is equal (or should be) to the error probability p_1 for one bright ion, n_0 ($n_1 = N - n_0$) is number of down (up) spins, and α (β) is number of down (up) spin flips to up (down) to misidentify state g_i as state f_j . We then simply invert this matrix to find state probabilities closer to the real ones

$$g_j = \sum_{i=1}^{2^N} M_{ji}^{-1} f_i \quad (4.20)$$

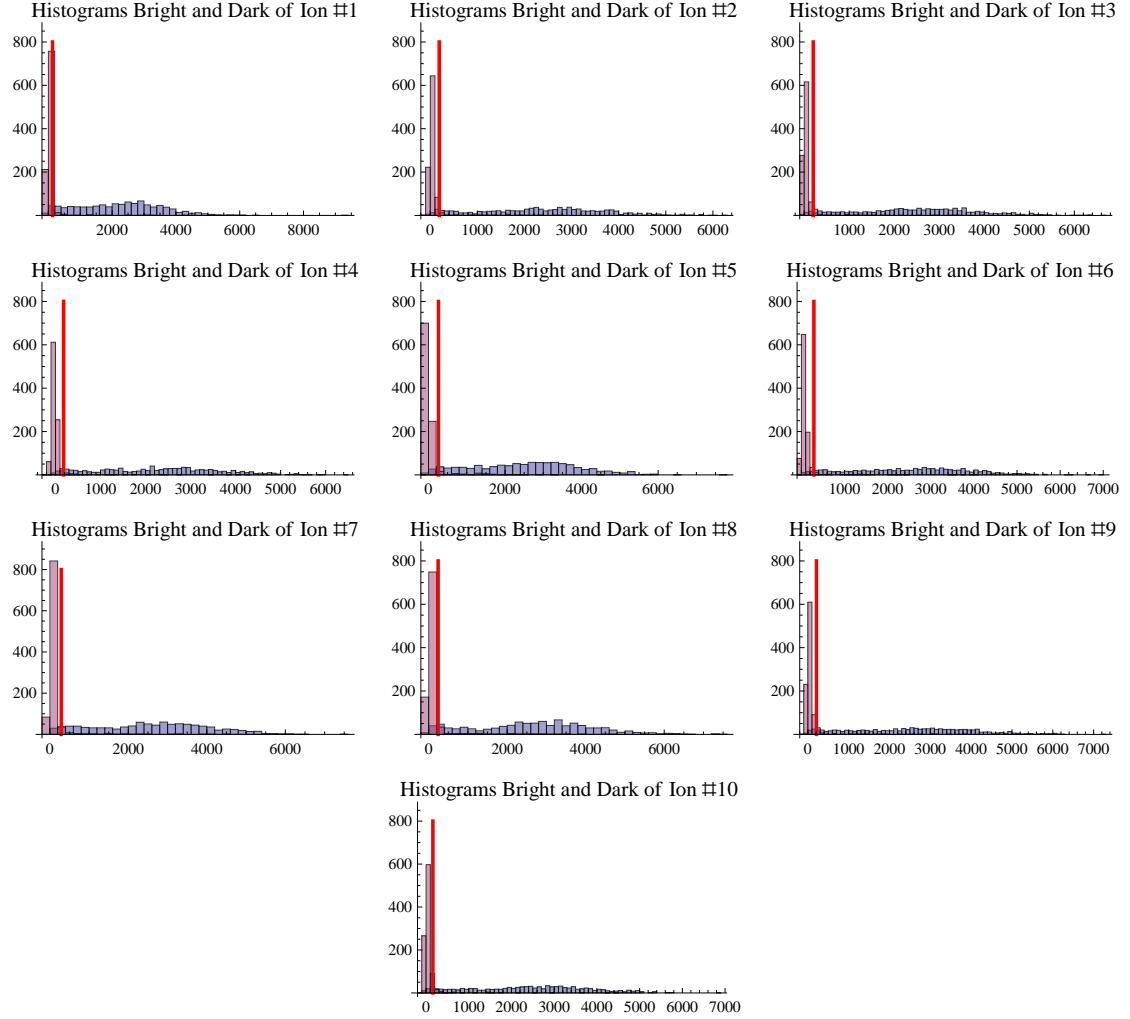


Figure 4.23: The background subtracted Gaussian fitted histograms for 10 ions, for the data in chapter 7. The units are arbitrary. The red line is the found discriminator between down and up states, and is somewhat different between ions.

The algorithm above assumes that we have correctly diagnosed the state detection error, that the error is the same for all ions in the chain, and that the error is independent between ions. All of these assumptions are likely only approximately true, so we can expect improvement but not complete correction of detected state probabilities.

4.5 Arbitrary Waveform Generator (AWG)

In order to generate the complex waveforms that drive the simultaneous Mølmer-Sørensen and Raman gates, we drive AOM 2 with a DA12000-16 from Chase Scientific. This is a standard PCI expansion card that outputs waveform at up to 2 GHz and has 16MB of on-board waveform memory. We have setup the AWG to operate at 1 GHz, and it is phase locked to a PTS3200 Direct Digital Synthesizer (DDS). This oscillator itself is phase locked to the same 10 MHz Rubidium clock as AOM 1, thus locking the phase between the modulations on both beams. Unlike all other oscillators used in the experiment, the AWG does not run continuously - it outputs the stored waveform when it receives a TTL trigger, and then stops. This makes the phase jitter on this trigger critical, as the jitter is transformed into noise on the phase relationship between the Raman AOMs. When a trigger is received, the AWG reads each byte in sequence from memory, and converts each byte with a 12 bit Digital to Analog Converter (DAC), such that 2047 is equivalent to 0V, 4096 is the max voltage, and 0 is the minimum voltage. This limitation on the vertical resolution does not create noticeable effects in the frequency domain as the AWG is

bandpassed. However it limits the resolution when dealing with waves of different magnitudes with physical effects of the same order of magnitude, i.e when we drive the Mølmer-Sørensen gate we drive sidebands > 10 times stronger than the wave that drives the Raman coupling. Thus, our resolution for the Raman coupling will be limited to much less than 2^{12} .

As the resonant frequency of the AOMs is 210MHz, the AWG will typically have only 4-5 points per wave cycle. This is sufficient to generate a frequency that can be bandpass filtered of its alias at $f_{clock} - f_{signal} \approx 800 \text{ MHz}$. Therefore, we chose to run the AWG at half its possible clock frequency and double the duration of the waves we can generate. At a clock rate of 1 GHz, a byte is converted to an analog voltage every 1ns, allowing us a total waveform time of 16 ms. This is more than sufficient for our experiments. Unfortunately, it is not sufficient for all of our diagnostic procedures, such as measuring the spin coherence time.

Besides the waveform duration limitation, there is also a limitation on waveform upload speed. For longer experiments (3-4ms), the upload time becomes significant. The DA12000 has a standard PCI type connector. Naively, this should imply a waveform upload speed of 133MB/s at least, so 120 ms upload time for the entire wave. Unfortunately, we have characterized the upload time to be approximately one hundred times slower. As a result, we are currently in the process of replacing this AWG with a more advanced model.

The AWG is controlled by functions provided in a DLL by Chase. As we interface the AWG via Labview, it was necessary to construct a DLL to interface the function library (da12000_dll.dll) and the card. The chief function of this library

is the translation of data structure from Labview into the data structure expected (“SegmentStruct”, as defined in appendix C) by the chapter loading function. Currently, the chapters run consecutively, and only the first chapter is triggered. A previous attempt to have multiple triggered waveforms results in the occasional missing of a trigger (likely due to a trigger being sent before a chapter was completely generated). This error affects all following experiments as the AWG chapter execution becomes mismatched with the other triggers/oscillators from the first AWG chapter being generated.

There is also an option for a chapter to loop for a fixed number of times. This may be useful for increasing the AWG effective time (for instance, for experiments where the AWG should generate a short pulse, a long duration of no output, and then another short pulse - i.e. Ramsey experiment).

Chapter 5

Experimental Procedure

5.1 Introduction

Before each experiment with our apparatus, we tend to perform the same preparatory tests and calibrations. In this chapter I will go through these procedures and some of the trouble shooting options when the system is more severely miscalibrated than usual.

5.2 Temperature

Before preparing to trap ions, all lasers must be correctly set and stable. Therefore, the first action of the day is turning on the lasers and allowing them to cool-down (or warm up) and equilibrate. For the DL-100 and Vanguard lasers this takes approximately half an hour. For the Verdi and MBR-110 this may take two hours, so generally we do not turn these lasers off when taking data. The Verdi and MBR require chillers for their operation, so these must be activated before the lasers. For the Vanguard, this is done automatically by MLUV. The MLUV program will also display the percent warm up of the THG [4.11](#).

The Pi:Max ICCD must be cooled down to its operating temperature as well (-25°C). The ICCD is cooled by a water circulating CPU cooler, operating at room

temperature. This is due to the crowding on the table preventing proper cooling by the ICCD fan. The ICCD is ready for operation in minutes.

RF power to the trap should be set to the operating power used for the experiment (typically around 26dBm), as the delivered power changes the resonant frequency of the trap. The set point of the TC200 heater for the resonator should be checked.

5.3 Frequencies

Now that the lasers are hopefully stable, their frequencies should be set. Assuming the lasers are well aligned, we set the laser frequencies for $^{171}\text{Yb}^+$ trapping, as indicated in table 5.1. These frequencies are measured by a HighFinesse solid state wavemeter, via optical fibers, and displayed by a homebuilt web client ¹. If loading fails, it might be necessary to attempt to load $^{174}\text{Yb}^+$, as it does not have hyperfine structure and hence scatters more light, and does not require all the laser modulation needed by $^{171}\text{Yb}^+$ nor can it have a coherent dark state [1]. The wavelengths for $^{174}\text{Yb}^+$ are listed in table 5.1 as well. When alternating to $^{174}\text{Yb}^+$, the loading rate may be highly increased by switching over to the natural isotope distribution Yb oven, although it is possible to load from our usual high purity ^{171}Yb oven.

After setting the laser frequencies, the lasers must be stabilized, as discussed in chapter 4, as well as the wavetrain frequency doubler for the MBR. This often requires slight adjustments of the input coupling lens.

¹Created by Peter Maunz.

Laser	$^{171}\text{Yb}^+$	$^{174}\text{Yb}^+$
MBR-110	405.644318 THz	405.645530 THz
935 nm DL-100	320.56922 THz	320.57190 THz
399 nm DL-100	751.52764 THz	751.52680 THz
638 nm DL-100	469.445-469.442 THz	469.439 THz

Table 5.1: Laser frequencies for trapping. The 638 nm can be locked anywhere in above range as long as it is mode-hop free for the entire range.

The Vanguard shutter should be opened and emission engaged (via MLUV). The Vanguard frequency cannot be set, rather the feed forward lock on AOM2 is engaged. For the RF resonator, the reference signal is adjusted to close to 0 by slightly adjusting the RF oscillator, and then engaging the RF frequency lock. A moderate gain must be set here (by tuning the HP8640B modulation strength knob) as recrystallization will severely change the resonance frequency. Also, the Labview voltage control program should be checked to see that there is no attenuation of the trap RF power. Once all lasers are locked one may turn on the Yb oven, and after a minute of oven warm up (at $\sim 2.4\text{A}$) one may drop the trapping voltages and RF power using the recrystallization settings, while radiating the trap with the 399 nm light and alternating pulses of 355 nm light, while waiting for an ion or ion cloud to appear in the Pi:Max3 viewing program (figure 4.22).

5.4 Loading and Alignment

If an ion is successfully loaded, then beam alignments must only be slightly adjusted to maximize cooling and detection counts. If loading is slow one may attempt to adjust the 399 nm beam, as that is the most likely to be misaligned. If

the detection or cooling seem to be unstable, one may try adjusting the 935 nm beam alignment and polarization.

In general, as all 369 beams share the same final path, it is reasonable to assume that if they are all overlapping then the beams are close to the correct alignment.

Another sanity check is the scatter patterns of the trap electrodes. By diverting the beams slightly up or down from the center of the trap, one may find the gaps between the trap electrodes by viewing the profile of the beam on exit through the view port. If all beams seem reasonably aligned and loading is not seen on ICCD, then the PMT counts should be viewed instead. If this fails as well, then Yb oven temp should be increased. If loading still fails, then the trap may have shifted relative to the imaging system. In order to realign the imaging system, one must detect a trap corner (as shown in figure 5.1), and thus reorient the imaging system micrometer settings relative to the trap. Vertical alignment of the beams based on the clipping profile of the beams is trivial. It is important to remember that the beams are entering the trap at a 45^0 angle, and the horizontal lens alignment of the beams is measuring the displacement of the beams at that angle rather than parallel to the trap. When viewing the corners of the trap, it is most likely the corners of the electrode furthest from the camera that are being viewed. When attempting to load over long periods, it is important to occasionally shut off the trap RF so as to release possible trapped ion clouds. These do not crystallize nor cool efficiently and are thus less visible than single ions.

Once the ions are loaded it is important to verify that the cooling and detecting

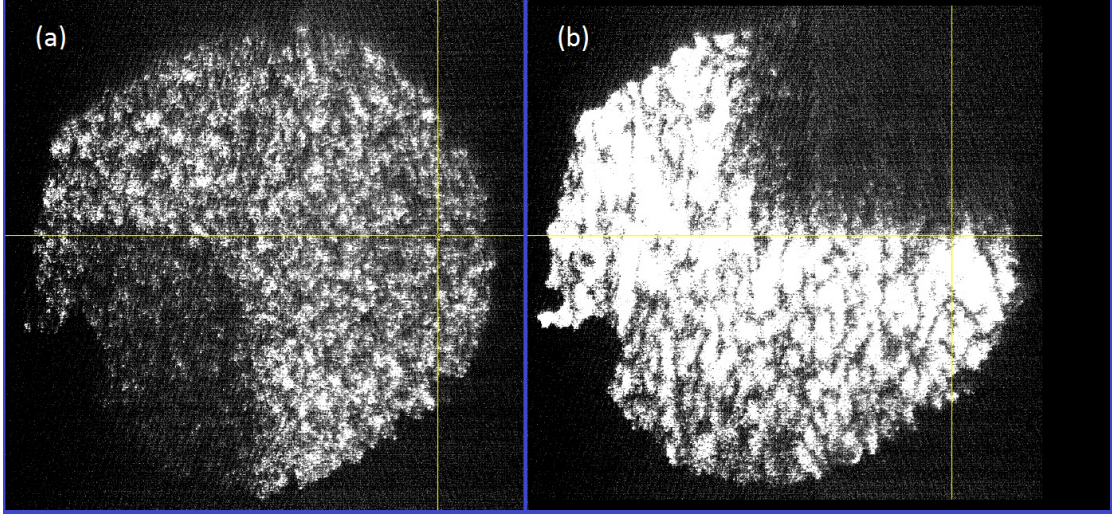


Figure 5.1: (a) Lower left trap corner. (b) Upper right corner. Pin-hole is clearly visible due to high scatter off trap. Burs are due to imperfect drilling.

beams are centered on the ion chain. This can be done by moving the ions across the camera (using the trap voltages to push them in the z-direction), but PMT detection counts are more exact. If one intends to take data using the ICCD, it is important to verify that all ions fall on the active PMT surface as the camera and PMT are independently aligned. There seem to be certain regions on the PMT surface that are not active. If it is suspected that the protection beams require alignment, then the iodine lock must be disengaged and the MBR tuned 400 MHz blue so as to bring those beam frequencies closer to transition resonance.

5.5 Raman Beams

Rough alignment of Raman beams may be done using an independent Ramsey experiment for each beam using a qubit frequency microwave pulse, or an AC Stark shift measurement. For the Ramsey stark shift measurement, the Vanguard feed

forward is unlocked, and an RF switch diverts the microwave reference to via an amplifier to microwave horn (the microwave source frequency is slightly adjusted so as to be exactly on carrier). First, the Rabi oscillation $\pi/2$ time is measured, i.e. the time it takes for the qubit to reach half of maximum brightness (the qubit is then in the x-y plane of spin space). Second, using the Experimental control program we schedule three experimental pulse sequences (“chapters”): a $\pi/2$ pulse, a 355 nm pulse, and another $\pi/2$ pulse. By scanning the duration of the 355 nm pulse, we can see “Ramsey fringes” - oscillations of the qubit due to the Stark shift of the qubit frequency. This method is very sensitive as the pulses can be 10’s of milliseconds long.

Once both beams are roughly aligned we can drive Raman transitions with both beams. At that stage maximizing the Rabi frequency is the fastest way to improve alignment. Finally, we return to Stark shift Ramsey measurements on the beams. We can then perform a long Ramsey experiment with no 355 nm light to measure accurately the carrier frequency, as any mismatch between the $\pi/2$ pulses and the qubit frequency will lead to oscillations where there should be none.

Now we use the Ramsey experiment to validate that the beams are truly centered. We shift the ion a distance on the order of the length of long ion chain, and validate that the Ramsey frequency is symmetric, adjusting the horizontal micrometer to achieve this. Barring suppression by micromotion, coupling to the y-mode, or incorrect polarization our Rabi carrier frequency is now maximized. Both beams should be linearly polarized, with electric fields parallel to table so as to drive the Raman transition with σ^+, σ^+ polarization in the ion’s frame of reference.

Raman spectrum for 10 ions, with 355 nm pulsed laser

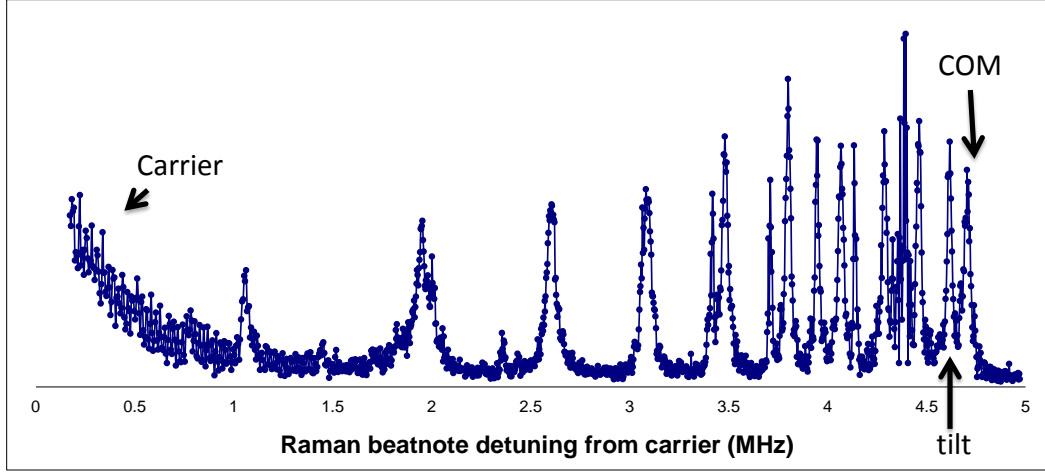


Figure 5.2: 10 ion Raman spectrum. The x-axis is in MHz detuning from carrier, that is centered at 0 MHz. The dominant motional modes are the x-transverse modes. As can be seen here, their width is only on the order of ~ 100 KHz, vs the carrier which is on the order of MHz. The highest frequency mode is the COM, and second is tilt. The lowest is the zig-zag mode, only a MHz away from carrier for these trap settings. Some of the weaker features are axial and y-modes, which have a weak coupling to our beam geometry.

5.6 Calibration

As we have identified our qubit frequency exactly, we are now interested in mapping out the motional modes, as can be seen in figure 5.2. If we do not know the general location of the motional modes (due to changes in trapping voltages, for instance), we may load two ions and measure the COM and tilt modes. That is sufficient to calculate all other modes. This can be done by scanning the modulation frequency of Raman beam 2 with a fixed pulse time. If the pulse duration is long enough and the intensity high enough to drive several oscillation periods for the weakest transition of interest then we can expect to see all resonances.

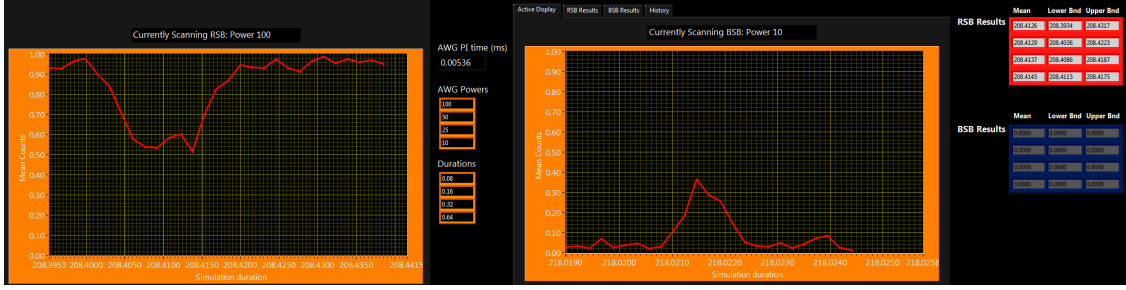


Figure 5.3: Results for two different intensities of the automatic side-band finder. The program finds increasingly accurate RSB and BSB frequencies by finding upper and lower limits for decreasing intensity and lengthier pulse times. Before finding the RSB, a π pulse is applied.

Once we identify the modes, we may preemptively apply two sidebands, roughly 100 KHz red detuned from the COM, with the intensity we expect to use for our Mølmer-Sørensen coupling gate. This will ensure that the following measurements will be immune to higher order Stark shifts. However we must shift all frequencies up by the measured Raman 2 Stark shift (~ 200 KHz , vs ~ 600 KHz for Raman 1), as they were performed at the lowest power possible. After applying side-band cooling to the COM mode, we may activate the automatic sideband finding functionality of the control program, as shown in figure 5.3.

After measuring Rabi oscillations frequencies for the BSB and RSB, we set them equal (equal AWG amplitudes for both frequencies do not necessarily drive equal strength sidebands), and detune them equally from resonance. We then add a carrier frequency, and measure its frequency for three different powers, for AWG amplitudes ~ 80 times lower than the sideband amplitudes. Thus, we have calibrated the AWG amplitudes to real frequencies. The relationship is linear for these low values.

We now add a second ion, and remove the carrier. We optimize the spin-spin

coupling by alternately scanning the amplitude of one the sidebands or a sideband frequency. This should lead to decent (0.1-1.7 ions bright) contrast, and roughly five coherent oscillations at our typical operating parameters. If the coherence is bad it is likely due to the vertical alignment of the Raman beams.

5.7 Imaging Calibration

We may now load all the ions needed for the experiment. After allowing the RF resonator to settle from the power drop needed for loading, we prepare an experiment sequence where the ions will cooled, then pumped dark, and then detected. The number of experiments per point is set to 1000. Then the camera calibration scan is activated, and we select the “Ions Dark” option. We add a π pulse to rotate all ions to bright after the optical pumping, and repeat the calibration procedure, this time selecting “Ions Bright”. The Mathematica script of [appendix D](#) will then automatically start. The control program will display the averaged bright ion images, with ROI boxes and detection parameters.

We are now ready to select our experimental chapters and parameters, and to begin experimenting.

Chapter 6

Summary of Experiments

6.1 Introduction

In this chapter I will summarize the experimental results we have achieved in our group leading up to the work reported in chapter 7¹. The first work I will report was our demonstration and control of spin-spin couplings between the pseudo-spins for two and three ions using global Raman beams. Once that ability was mastered, we were able to proceed with the adiabatic quantum simulation experiments: Measuring the phase diagram of the ground state Hamiltonian for three spins; Creating a frustrated triangle of AFM coupled spins; Creating a phase transition from the paramagnetic state to FM and AFM states with 16 spin. For most of this work, our Raman beams were driven by an the MBR, detuned only 2.7 THz from the $^2S_{1/2} - ^2P_{1/2}$ transition, and with only 200 mW of UV light. These gates were enabled by microwave frequency combs of the EOM modulated laser beams, at roughly half the qubit frequency. These beams were then replaced by the 33 THz detuned 355 nm laser beams, with 4W of UV. This scheme offers the same coupling strengths with much lower unwanted scatter rates.

Using the simulated gates I introduced in chapter 3, we will simulate the

¹This chapter follows closely parts of [55]

Hamiltonian

$$H = \sum_{i < j} J_{i,j} \sigma_x^i \sigma_x^j + B_y \sum_i \sigma_y^i \quad (6.1)$$

The axis of the interactions will be selected by controlling the relative phase of beatnotes generating the interactions.

6.2 Experimental Demonstration of the Ising interaction

We trap $^{171}\text{Yb}^+$ ions in a linear chain along the trap Z -axis, and the axial COM trap frequency is controlled in the range $\nu_z = 0.6 - 1.7$ MHz. The COM mode is set to around ~ 4 MHz. The other transverse Y modes are sufficiently far away from the X modes and do not overlap. Moreover the coupling to these modes is suppressed by a factor of > 10 by rotating the principal Y -axis of motion to be nearly perpendicular to the laser beams, as described in chapter 4.4.6.

We direct two Raman laser beams onto the ions to drive spin-dependent forces, with their wavevector difference aligned along the transverse x -axis of ion motion ($\Delta k = k\sqrt{2}$, where $k = 2\pi/\lambda$). The Raman beams are detuned $0.5 \sim 2.7$ THz to the red of the transition at a wavelength of $\lambda = 369.76$ nm. The Raman beams are phase modulated at a frequency nearly half of the $^{171}\text{Yb}^+$ hyperfine splitting with a 6.32 GHz resonant EOM, and each of the two Raman beams have independent AOM shifters in order to select appropriate optical beatnotes to drive Raman transitions [56]. The Raman beams are focused to a waist of approximately $30 \sim 100 \mu\text{m}$ with a power of up to $10 \sim 20$ mW in each beam. When their beatnote is adjusted to drive the carrier transition at the hyperfine transition ν_{HF} , we observe a carrier Rabi

frequency of $\Omega_i/2\pi \approx 1$ MHz. For the spin-dependent force, we set $\Omega_i/2\pi \approx 0.4$ MHz for each pair of Raman beam and for the transverse field, $\Omega_i/2\pi$ is less than 0.1 MHz. The resonant transition generates the effective transverse field by adjusting the phase with respect to the spin-dependent force. For up to nine ions in a chain, we observe that the outer two ions experience $\sim 2\%$ lower Rabi frequency, and the variation in the differential AC-Stark shift in each qubit of $< 1\%$.

In the experiment, we first Doppler laser cool $^{171}\text{Yb}^+$ ions for 3 ms using a laser tuned red of the $^2S_{1/2} - ^2P_{1/2}$ transition at a wavelength of 369.53 nm. We then Raman sideband cool all m modes of transverse motion along x to mean vibrational indices of $\bar{n}_m < 1$ in about 0.5 ms, well within the Lamb-Dicke limit. Next, the ions are each initialized to the $|\downarrow\rangle$ state through standard optical pumping techniques [1]. We then apply the optical spin-dependent force on the ions for a duration τ by impressing the bichromatic beatnotes at $\nu_{HF} \pm \mu$. Afterward, the spin states are measured by directing resonant laser radiation having all polarizations on the $^2S_{1/2}(F=1) - ^2P_{1/2}(F'=0)$ transition following standard state-dependent fluorescence techniques [1]. We use a charge-coupled-device (CCD) imager (the detection efficiency is, 95 % per spin). We determine the probability of each spin configuration (for example $P_{\uparrow\downarrow}$) by repeating the above procedure more than 1,000 times. We also measure the probability P_n of having n spins in state $|\uparrow\rangle$ by using the PMT, which is useful for higher-efficiency measurements of certain symmetric observables such as entanglement fidelities and witness operators.

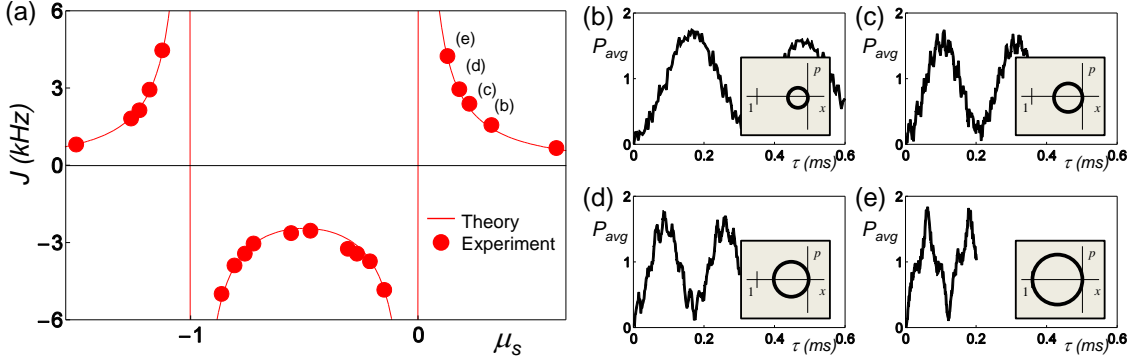


Figure 6.1: (a) Measured coupling J for two ions as a function of detuning μ overlaid with theory (lines) from Eq.(3.22) with no free fit parameters. The detuning is scaled to the axial (ν_z) and transverse (ν_1) COM normal-mode frequencies of motion such that COM, and tilt modes of transverse motion occur at $\mu_S \equiv (\mu^2 - \nu_1^2)/\nu_z^2 = 0$ and -1 , respectively. (b) Time evolution of the average number of ions in the $|\uparrow\rangle$ state under the influence of the bichromatic force in the far-detuned limit, showing the secular oscillation of the Ising spin-spin coupling, where the detuning $\mu/2\pi$ is 80 KHz from the COM motional sideband. (c) Measurements with $\mu - \nu_1 = 2\sqrt{3}\eta_1\Omega/2\pi \approx 56$ KHz. Here the small oscillations from the motional excitation and the coupling to spin states are noticeable on top of the sinusoidal oscillations of the Ising interactions. (d) Measurements at $\mu - \nu_1 = 2\sqrt{2}\eta_1\Omega/2\pi \approx 45$ KHz. (e) Measurements at $\mu - \nu_1 = 2\eta_1\Omega/2\pi \approx 32$ KHz. The insets of (b)-(e) show the respective wavepackets in phase space and the areas enclosed are shaded.

6.2.1 Two spin case

Figure 6.1(a) shows the theoretical values of $J = J_{1,2}$ from Eq.(3.22) and measurements at various detunings μ for two spins with $J = -\Omega_1\Omega_2(\frac{\eta_1^2\nu_1}{\mu^2-\nu_2^2} - \frac{\eta_2^2\nu_2}{\mu^2-\nu_1^2})$, where $\eta_1 = \Delta k/\sqrt{4m\nu_1}$ and $\eta_2 = \Delta k/\sqrt{4m\nu_2}$ are the Lamb-Dicke parameters for COM and tilt modes. The solid theoretical curve is plotted with no adjustable parameters, as the motional mode frequencies and the sideband Rabi frequencies are independently measured.

We measure the strength of J by observing the time evolution between $|\downarrow\downarrow\rangle_z$ and $|\uparrow\uparrow\rangle_z$ after applying the spin-dependent forces on $|\downarrow\downarrow\rangle_z$ states. The evolution

for the two spins is simply described by $U(t) |\downarrow\downarrow\rangle_z = \exp(-iJ\sigma_x^{(1)}\sigma_x^{(2)}t) |\downarrow\downarrow\rangle_z = \cos(Jt) |\downarrow\downarrow\rangle_z + i \sin(Jt) |\uparrow\uparrow\rangle_z$ when we neglect the couplings between internal states and the motion. As shown in figure 6.1(b), the oscillations of the populations are sinusoidal, with frequency $2J$. To detect the sign of the Ising coupling, we applied the same force on the initial state $|\uparrow\uparrow\rangle$ and observe the phase of the oscillations.

When the beatnote detuning μ is close to a vibrational mode, or $|\mu - \nu_{1,2}|$ is within a few sideband linewidths $\eta_{1,2}\Omega$, the coupling between motion and spin states modulates the spin state evolution. Figure 6.1(e) shows the spin state evolution at a detuning $\delta = \mu - \nu_1 = 2\eta_1\Omega$ [3]. In this case, the motional state is displaced in phase space by no more than $|\alpha| = 1$, and at particular times during the evolution $\tau = n/\delta$ ($n = 1, 2, \dots$) the motional degree of freedom is decoupled from the internal state, enabling the generation of pure spin-spin entanglement. As the detuning δ increases as shown in figure 6.1(b)-(d), the maximum displacement decreases and the evolution approaches a pure sinusoid indicative of pure spin-spin interactions. Typical experiments are performed with $\delta \geq 4\eta\Omega$, where the largest displacements in a $\sim 2\%$ modulation in the spin evolution.

6.2.2 Three spin case

For three spins addressed uniformly with the Raman laser beams, we have $J_1 = J_{1,2} = J_{2,3}$ as the nearest-neighbor (NN) interaction and $J_2 = J_{1,3}$ as the next-nearest-neighbor (NNN) interaction as shown in figure 6.2(a). Since the bandwidth of the transverse mode spectrum is relatively small, all modes can be addressed from

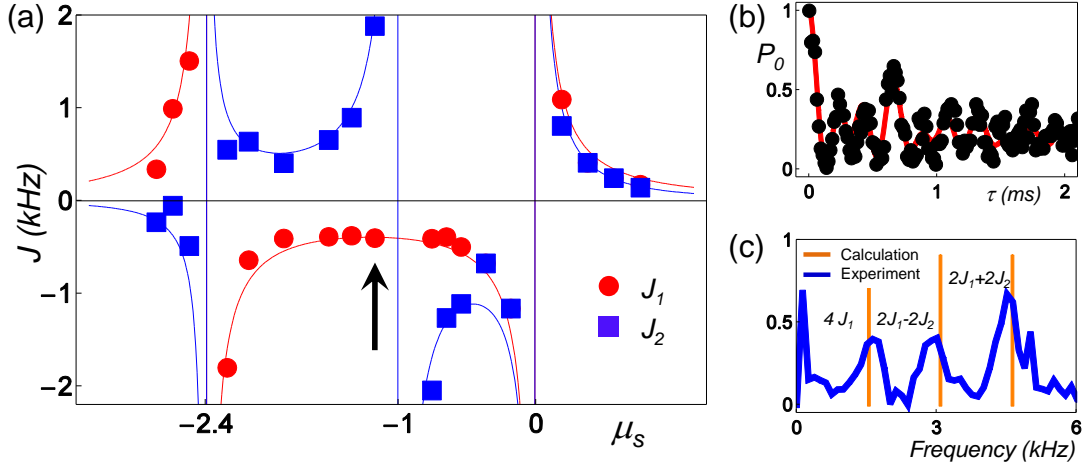


Figure 6.2: (a) Measured couplings $J_1 = J_{1,2} = J_{2,3}$, $J_2 = J_{1,3}$ for three ions as a function of detuning μ overlaid with theory (lines) from Eq.(3.22) with no adjustable parameters. At the scaled detuning μ_S , COM, tilt and zig-zag modes of transverse motion occur at $\mu_S \equiv (\mu^2 - \nu_1^2)/\nu_z^2 = 0, -1$ and -2.4 , respectively. (b) Time evolution of the probability P_0 of all spins $|\downarrow\rangle$ under the bichromatic force in the far-detuned limit. Here, the two couplings J_1 and J_2 are clearly visible. The solid line is a fit to the time evolutions of Eq.(6.1) with an empirical exponential decay. The measurements are performed at the indicated detuning in (a), or -50 kHz from tilt mode. (c) The Fourier transform of the experimental curve shown in (b), where three peaks originate from the frequency components of $4J_1$, $2J_1 - 2J_2$ and $2J_1 + 2J_2$. The orange bars represent the calculated values from Eq.(3.22). The peak near the origin comes from the overall decay of the oscillation due to decoherence with ~ 100 Hz.

a single laser beatnote and the signs and the strengths of J_1 and J_2 are under great control as shown in figure 6.2(a) and Eq.(3.22) [57]. In the region $\mu > \nu_1$, both have anti-ferromagnetic (AFM) interactions ($J_{1,2} > 0$), and in the region of $\nu_2 < \mu < \nu_1$, both have ferromagnetic (FM) couplings ($J_{1,2} < 0$). In the region $\nu_3 < \mu < \nu_2$, the NN interaction is FM ($J_1 < 0$) and the NNN is AFM ($J_2 > 0$). When μ is near the tilt mode, J_2 overpowers J_1 and when μ is closer to the zig-zag mode, J_1 is stronger than J_2 . Finally, for $\mu < \nu_3$, all interactions are FM again.

We measure the J_1 and J_2 couplings by observing the oscillations in the population of state $|\downarrow\downarrow\downarrow\rangle_z$ after applying spin-dependent force on the three spins. This population oscillates as $\cos^2 J_1 t \cos J_2 t - i \sin^2 J_1 t \sin J_2 t$, as shown in figure 6.2(b). We use Fourier analysis on the oscillations and find certain frequency combinations of the couplings $4J_1$, $2(J_1 - J_2)$, and $2(J_1 + J_2)$, as shown in figure 6.2(c). In this figure, we use theoretical values for the signs of J_1 and J_2 .

6.3 Adiabatic quantum simulation

In this section, we describe the adiabatic quantum simulation of the transverse Ising model with three spins, where the exact solution is known, and discuss the criteria for adiabaticity. We then present experimental results for two example Ising interactions strengths and signs.

We experimentally investigate this adiabaticity criterion for the two different types of NNN coupling that were introduced above. We initialize the spins along the B_y -direction through optical pumping ($\sim 1 \mu s$) and a $\pi/2$ rotation about the

$-x$ -axis of the Bloch sphere. Figure 1.3 shows the adiabatic simulation protocol. The simulation begins with a simultaneous and sudden application of both B_y and J_1, J_2 where B_y overpowers J_1 ($B_y/|J_1| \approx 10$). As the spins are aligned along the y -axis, the sudden turn on will not cause diabatic effects. A typical experimental ramp of B_y decays as $B_y(t) = ae^{-t/\tau} + b$ with a time constant of $\tau \sim 30 \mu s$, varying from $a \sim 10$ kHz to a final offset of $b \sim 500$ Hz after $t = 300 \mu s$. By varying the power in only one of the Raman beams, this procedure introduces a change in the differential AC Stark shift of less than 2 Hz. We turn off the Ising interactions and transverse field at different $B_y/|J_1|$ endpoints along the ramp. We then measure the magnetic order along the x -axis of the Bloch sphere by first rotating the spins by $\pi/2$ about the y -axis, and detecting the z -component of the spins.

In figure 6.4(a) all interactions are FM and $J_2/|J_1| \sim -2.4$ (as in figure. 6.3(a)). The dashed lines in the top panel are the adiabaticity parameter from Eq.(1.6) calculated over the trajectory for the two coupled excited states (recall figure 6.3). Due to the 500 Hz final offset of B_y , the simulation stops at $B_y/|J_1| \sim 0.5$. To examine the behavior extended below this value, we calculate the criteria for an exponential ramp with a 100 μs time constant. This profile was chosen to overlap with experimental parameters for large $B_y/|J_1|$ and also reach $B_y = 0$ in a typical simulation time ($\sim 300 \mu s$). The results indicate that Eq.(1.6) is satisfied over the trajectory; $\dot{B}_y(t)\epsilon/\Delta_{ge}^2$ remains much less than one even with a maximum occurring at $B_y/|J_1| \sim 1$. To demonstrate the simulation is indeed adiabatic for these parameters, we plot the measured probability of occupying a FM state $P(\text{FM}) = P_{\uparrow\uparrow\uparrow} + P_{\downarrow\downarrow\downarrow}$ (solid dots) in figure 6.4(a). The black line represents the adiabatic ground state

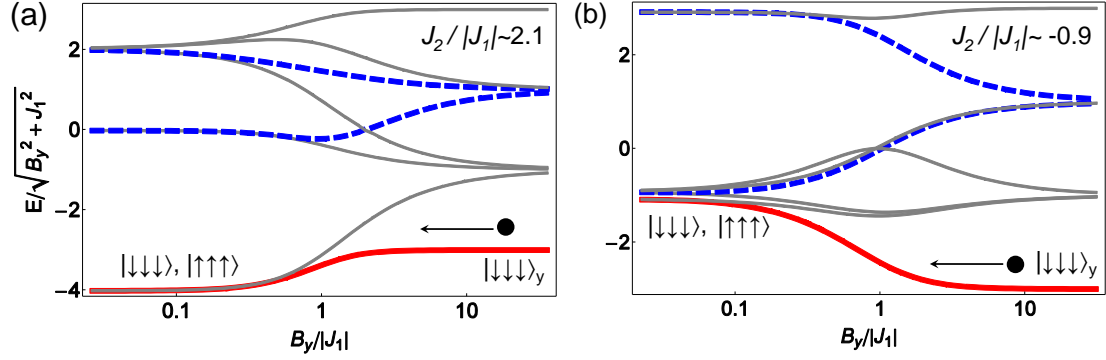


Figure 6.3: Energy level diagrams for Eq.(6.1) with two different types of spin-spin interactions. For both panels, the NN interactions are FM ($J_1 < 0$). (a) The NNN interaction is FM with $J_2/|J_1| \sim -2$ and (b) AFM with $J_2/|J_1| \sim 0.9$. The arrow in both diagrams indicates the trajectory in the simulation, initialized at $B_y/|J_1| \sim 10$. Under this condition, the initial ground state is an eigenstate of second term in Eq.(6.1), a polarized state along B_y . In both examples, at $B \approx J_1$ some high energy states cross, but the ground state (black solid line) has no level crossings with any excited state. Likewise, the highest energy state does not cross any other levels, allowing one to also adiabatically follow this state. The dotted lines represent excited states which are most strongly coupled to the ground state along the path. In the large field limit, the energy difference between ground and excited states Δ_{ge} (here, scaled by $\sqrt{B_y^2 + J_1^2}$) is proportional to B_y , but as $B_y/|J_1|$ decreases the spin-spin couplings determine the energy difference and the form of the ground state. In both (a) and (b), the final ground state is FM (defined along the x-axis of the Bloch sphere), however in the case of (a), the minimum Δ_{ge} is ~ 20 times larger.

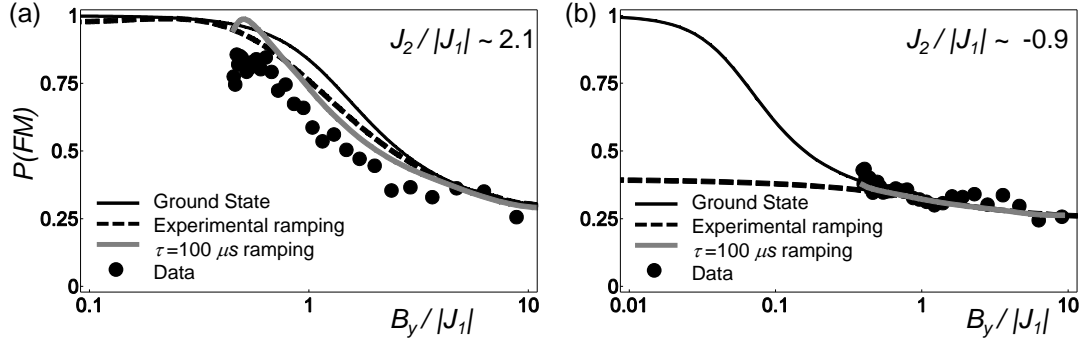


Figure 6.4: (a) The theoretical order from the exact experimental ramp with a $35 \mu\text{s}$ time constant and final offset value given in the text (gray solid line) is in reasonable agreement with the order in the true ground state (black solid line) for $B_y/J_1 > 0.5$. The dotted line is the expected state evolution for a pure exponential decay ramp with a $100 \mu\text{s}$ time constant, allowing $B_y \rightarrow 0$. (b) The data also matches well to theory, as we avoided the regions where diabatic transitions are expected for $B_y/J_1 \ll 1$. According to the calculations, the duration of three-spin experiments near the special point should be on the order of milliseconds.

and the grey line is the theoretical expected probability including the experimental ramp. The dotted line in this figure is the theoretical state evolution using a B_y -field ramp that reaches zero. The predicted evolution does not significantly deviate from the ideal ground state and the data is in good agreement with all three theory curves.

Figure 6.4(b) presents the case when the NNN interaction is AFM and $J_2/|J_1| \sim 0.9$ (as in figure 6.3(b)). When $B_y/|J_1| \ll 1$, $\dot{B}_y(t)\epsilon/\Delta_{ge}^2$ reaches a maximum value of ~ 0.6 , indicating that the probability for excitations will likely increase. This difference is because in this case the gap Δ_{ge} at the 'critical' point is ~ 15 times smaller than that in figure 6.3(a). In contrast to the FM J_2 case, the theoretical probability curves shown in the lower panel of figure 6.4(b) predict significant diabatic effects

when using this B_y -field profile for simulations near the critical point. In fact, to successfully evolve to the true ground state near $B_y = 0$, the simulation time (assuming same initial conditions and an exponential ramp of B_y) should be at least a factor of ten longer.

Because all the data lies outside of the region where the energy gaps are small, the diabatic excitations are minimal, but further experimental study is needed to precisely quantify this effect. One method to probe excitations, which may also be useful as $N \gg 1$, is to perform and then reverse the experimental ramp and measure the probability of returning to the initial state [58].

6.4 Phase diagram

Assuming adiabaticity as described above, we can generate an experimental phase diagram for the transverse Ising model. We will first describe this for the three spin case, and then discuss specific features and scalability in sections 6.6 and 6.7. For the three spin Hamiltonian in Eq. (6.1), the competition between the two spin-spin couplings and the transverse field gives rise to a rich phase diagram. Here we label the 2^3 possible spin configurations as the two FM states, $|\uparrow\uparrow\uparrow\rangle$ and $|\downarrow\downarrow\downarrow\rangle$, two symmetric AFM states, $|\downarrow\uparrow\downarrow\rangle$ and $|\uparrow\downarrow\uparrow\rangle$, and four asymmetric AFM states, $|\uparrow\uparrow\downarrow\rangle$, $|\uparrow\downarrow\downarrow\rangle$, $|\downarrow\uparrow\uparrow\rangle$ and $|\downarrow\downarrow\uparrow\rangle$, all defined along the x -axis of the Bloch sphere.

In figure 6.5(a), we plot a part of the theoretical phase diagram where the nearest-neighbor interactions are always FM ($J_1 < 0$). The order parameter is the probability of occupying a FM state, $P(\text{FM}) = P_{\uparrow\uparrow\uparrow} + P_{\downarrow\downarrow\downarrow}$. For regions where

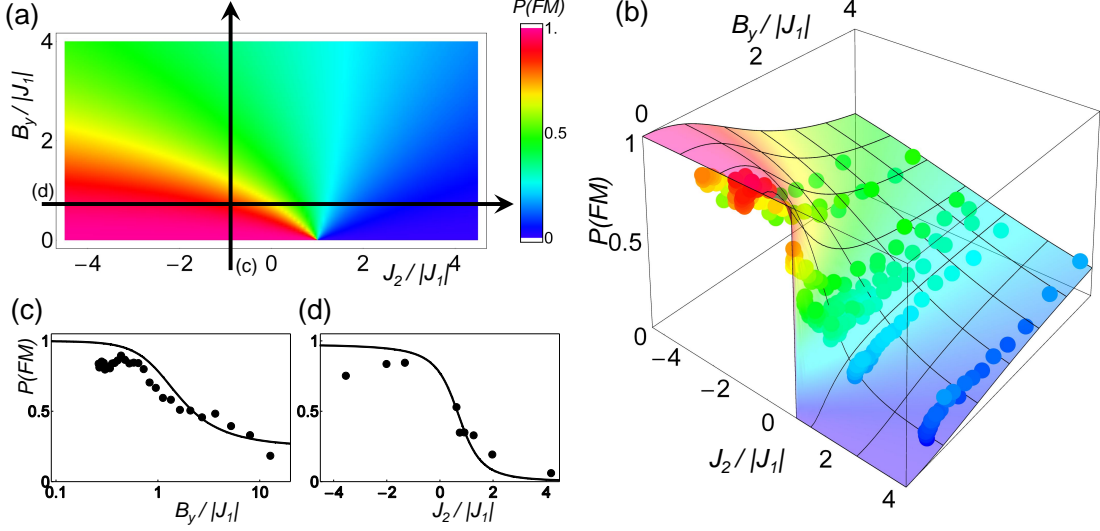


Figure 6.5: (a) Theoretical phase diagram for Eq.(6.1). The color scale indicates the amplitude of the FM order parameter, $P(FM) = P_{|\uparrow\uparrow\uparrow\rangle} + P_{|\downarrow\downarrow\downarrow\rangle}$. Here, J_1 is always negative, yielding FM order in that coupling. In the region where $J_2/|J_1| < 0$, there is a crossover to FM order as $B_y/|J_1|$ is lowered. When $J_2/|J_1| > 0$, the AFM and FM interactions compete. When $J_2/|J_1| = 1$ and $B_y = 0$ the ground state is comprised of 6 states: four asymmetric AFM and two FM states. This creates a special sharpened point where all lines of equiprobable FM order converge. (b) Experimental measurements of the phase diagram for Eq. 6.1 (solid bars) compared to the theoretical prediction from Fig. 6.5 (surface). The vertical amplitude is the FM order parameter $P(FM) = P_{|\uparrow\uparrow\uparrow\rangle} + P_{|\downarrow\downarrow\downarrow\rangle}$. The ratio of $B_y/|J_1|$ was varied from ~ 10 to ~ 0.1 for $J_2/|J_1|$ values of -1.3, -2.0, -3.6, 4.2, 2.0, 1.3, 0.92, 0.74, and 0.62. $J_1 < 0$ for all traces. (c) As $B_y/|J_1| \rightarrow 0$ in the region where $J_2/|J_1| < -1$, we observe a smooth crossover to FM order. The filled circles and solid line are the data and theory for $J_2/|J_1| = -1.3$, respectively. (d) When changing J_2 for a fixed and small value of $B_y/|J_1|$ the system undergoes a sharp transition. The data (filled circles) shown is for a scan of $B_y/J_y = 0.57$. The average deviation per scan of $B_y/|J_1|$ from the exact ground state is ~ 0.09 .

$B_y/|J_1| \gg 1$, the ground state is polarized along B_y with $P(\text{FM}) = 2/2^N = 1/4$, as all states in the x -basis are equally populated and there are two FM states. As $B_y/|J_1|$ decreases, different magnetic phases arise. When the NNN interaction is also FM ($J_2 < 0$), and $B_y/|J_1| \ll 1$ the ground states are the two degenerate FM states. In the region where the NNN interaction is AFM and J_2 overpowers J_1 ($J_2/|J_1| > 1$), the asymmetric AFM states are lowest in energy. A special point appears at $J_2/|J_1| = 1$ and $B_y = 0$, where all the contours of constant FM order meet. Here, the ground state will be a superposition of the FM and asymmetric AFM states. This effect arises because the pairwise interaction energy cannot be minimized individually, leading to a highly degenerate, or frustrated, ground state [59].

To be clear, when $J_1 = J_2$, both the FM and AFM ground states are degenerate. As can be seen in figure 6.3(b), as the transverse field is reduced the energy gap will go to zero, and adiabaticity will be impossible. For the FM case, there is a two fold degeneracy. For the AFM case, there is a six fold degeneracy. However, for our experiments we always have a slight transverse field remaining and the degeneracy is lifted, creating the non-degenerate, superposed ground states we discuss in this paper.

This procedure is performed for nine different combinations of J_1 and J_2 determined by the beatnote detuning μ from Eq.(3.22). In figure 6.5(b) we present the results as a 3D plot of the FM order parameter, with the theoretical phase diagram (surface) from figure 6.5(a) superimposed on the data. The data is in good agreement with the theory (average deviation per trace is ~ 0.09) and shows many of the

essential features of the phase diagram. As $B_y/|J_1|$ decreases, a smooth crossover from a non-ordered state to FM order occurs in the region where $J_2/|J_1| < 1$ (Fig. 6.5(c)). The data (e.g. figure 6.5(c) show small amplitude oscillations in the initial evolution due to the sudden application of the spin-spin interaction, which is held constant during the simulation to minimize variation in the differential AC stark shifts. As the number of spins increases, this is an example of a quantum phase transition. A first order transition due to an energy level crossing is apparent (figure 6.5(d) when changing J_2 for a fixed and small value of $B_y/|J_1| = 0.57$. This transition is sharp, even in the case of three spins [60].

6.5 Spin frustration and entanglement

We also study the properties of the ground states in the case of a frustrated Ising Hamiltonian. Frustration in spin systems occurs when spins cannot find a ground state that minimizes the energy of each pairwise interaction [61, 12]. As shown in figure 6.6(a), this can be simply illustrated by three spins with AFM interactions on a triangular lattice [62]. The situation gives rise to a large ground state degeneracy, leading to magnetic analogues of liquids and the crystal arrangement of ice [63, 64]. For quantum spins, the frustrated ground states are expected to be directly related to entanglement [65, 66].

We realize the textbook example of spin frustration in a unit triangular cell with AFM interactions by setting the Raman beatnotes μ to the blue side of COM mode. For comparison, we also study the ground state property of all FM interac-

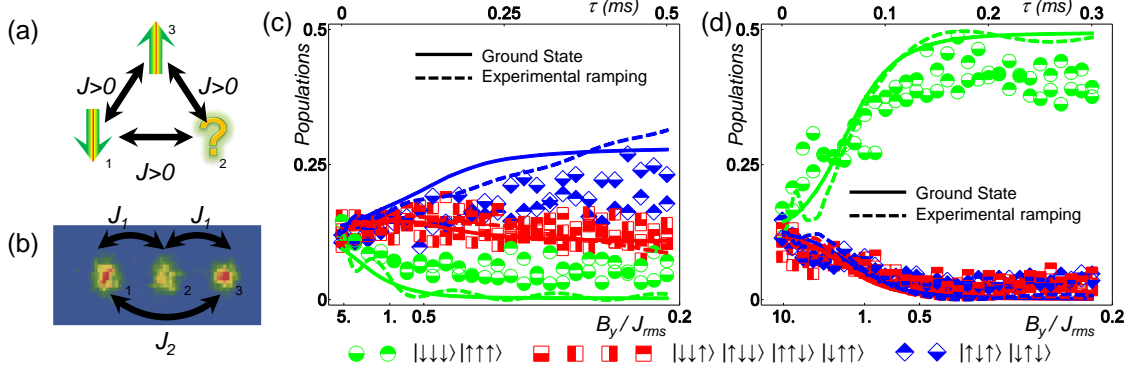


Figure 6.6: (a) Simplest case of spin frustration in a triangular geometry with AFM interactions. (b) Image of three trapped atomic $^{171}\text{Yb}^+$ ions in the experiment, taken with an intensified CCD camera. The spins in the linear ion string have nearest-neighbor (J_1) and next-nearest-neighbor (J_2) interactions mediated through the collective vibrational modes. (c),(d) Evolution of each of the eight spin states, measured with a CCD camera, plotted as B_y/J_{rms} is ramped down in time, with each plot corresponding to a different form of the Ising couplings. The dotted lines correspond to the populations in the exact ground state and the solid lines represent the theoretical evolution expected from the actual ramp, including nonadiabaticity from the initial sudden switch-on of the Ising Hamiltonian. (c) All interactions are AFM. The FM-ordered states vanish and the six AFM states are all populated as $B_y \rightarrow 0$. Because $J_2 \approx 0.8J_1$, a population imbalance also develops between symmetric and asymmetric AFM. (d) All interactions are FM, with evolution to the two ferromagnetic states as $B_y \rightarrow 0$.

tions by setting μ to the red side of COM mode. A linear chain of three ions can have NN and NNN interactions through the collective normal modes discussed in section 3.4 (figure 6.6(b)). The experimental procedure to prepare the ground states of the Hamiltonian with all AFM interactions and all FM interactions is the same as the description in the section 4. Figure 6.6(c) shows the time evolution for the Hamiltonian frustrated with nearly uniform AFM couplings and gives almost equal probabilities for the six AFM states (three-quarters of all possible spin states) at $B_y \approx 0$. Because $J_2 < 0.8J_1$ for this data, a population imbalance also develops between symmetric and asymmetric AFM states. Figure 6.6(d) shows the evolution to the two ferromagnetic states as $B_y \rightarrow 0$, where all interactions are FM.

The adiabatic evolution of the ground state of Hamiltonian (6.1) from $B_y \gg J_{rms}$ to $B_y \ll J_{rms}$ should result in an equal superposition of all classical ground states and therefore carry entanglement. For instance, for the FM case, we expect a GHZ ground state $|\downarrow\downarrow\downarrow\rangle - |\uparrow\uparrow\uparrow\rangle$. For the isotropic AFM case, we expect the ground state to be $|\downarrow\downarrow\uparrow\rangle + |\uparrow\downarrow\downarrow\rangle + |\downarrow\uparrow\uparrow\rangle - |\uparrow\uparrow\downarrow\rangle - |\downarrow\uparrow\downarrow\rangle - |\uparrow\downarrow\uparrow\rangle$. We characterize the entanglement in the system at each point in the adiabatic evolution by measuring particular entanglement witness operators [67]. This is accomplished by performing various global rotations to the three spins before measurement, and combining the results of many identical experiments. When the expectation value of such an operator is negative, this indicates entanglement of a particular type defined by the witness operator. For the FM case, we measure the expectation of the symmetric GHZ witness operator $W_{GHZ} = 9\hat{I}/4 - \hat{\mathcal{J}}_x^2 - \sigma_y^{(1)}\sigma_y^{(2)}\sigma_y^{(3)}$ [68, 67], where \hat{I} is the identity operator and $\hat{\mathcal{J}}_i \equiv \frac{1}{2}(\sigma_i^{(1)} + \sigma_i^{(2)} + \sigma_i^{(3)})$ is proportional to

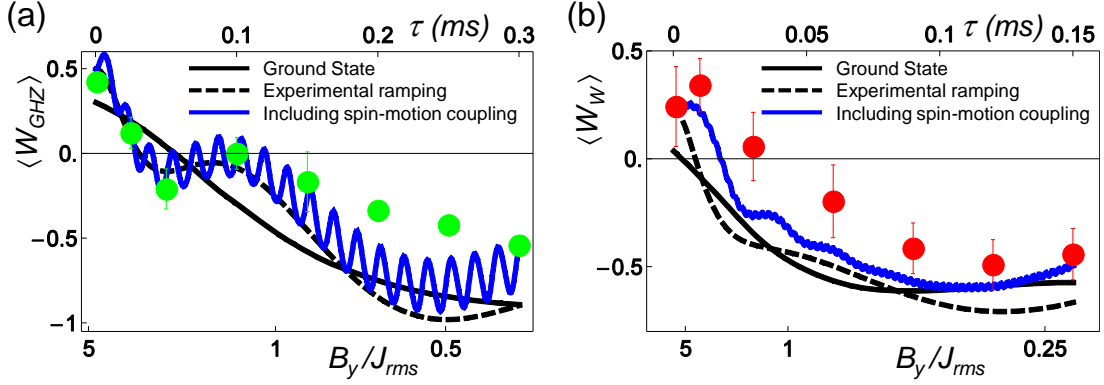


Figure 6.7: (a) Entanglement generation through the quantum simulation for the all FM interactions. We measure the entanglement by observing the expectation of a particular operator that indicates the presence of entanglement, called the entanglement witness [67]. For the case of all FM interactions we use the GHZ witness [67], sensitive to the state $(|\downarrow\downarrow\downarrow\rangle - |\uparrow\uparrow\uparrow\rangle)/\sqrt{2}$. We find that entanglement occurs when $|B_y|/J_{rms} < 1$. (b) Entanglement generation for the case of all AFM interactions. Here, we use the symmetric W-state witness, sensitive to the state $(|\downarrow\downarrow\uparrow\rangle + |\downarrow\uparrow\downarrow\rangle + |\uparrow\downarrow\downarrow\rangle - |\downarrow\uparrow\uparrow\rangle - |\uparrow\downarrow\uparrow\rangle - |\uparrow\uparrow\downarrow\rangle)/\sqrt{6}$ and we find that entanglement emerges for $B_y/J_{rms} < 1.1$. In both (a) and (b) the error bars represent the spread of the measured expectation values for the witness, likely originating from the fluctuations of experimental conditions. The black solid lines are theoretical witness values for the exact expected ground states, and the black dashed lines describe theoretically expected values at the actual ramps of the transverse field B_y . The blue lines reveal the oscillation and suppression of the entanglement due to the remaining spin-motion couplings, showing better agreement to the experimental results. Note that the residual spin-motion couplings do not appear to impact on the FM order of each state, as shown in Fig. 6.6. In the theoretical curves we do not include other possible errors such as state detection inefficiency or errors due to spontaneous scattering or fluctuations in control parameters.

the l th projection of the total effective angular momentum of the three spins. For the AFM (frustrated) case, we measure the expectation of the symmetric W state witness, $W_W = (4 + \sqrt{5})\hat{I} - 2(\hat{\mathcal{J}}_x^2 + \hat{\mathcal{J}}_y^2)$ [67]. In both cases, as shown in figure 6.7, we find that entanglement of the corresponding form develops during the adiabatic evolution.

In macroscopic systems, the global symmetry in the Ising Hamiltonian (6.1) is spontaneously broken, and ground-state entanglement originating from this symmetry is expected to vanish for the non-frustrated FM case [6]. However, for the frustrated AFM case, the resultant ground state after symmetry-breaking (e.g., $|\uparrow\uparrow\downarrow\rangle + |\uparrow\downarrow\uparrow\rangle + |\downarrow\uparrow\uparrow\rangle$) is still entangled. While spontaneous symmetry-breaking does not occur in a small system of three spins, we can mimic its effect by adding a weak effective magnetic field $-B_x \sum_i \sigma_x^{(i)}$ to the Hamiltonian during the adiabatic evolution [69, 70]. We experimentally observed that the frustrated ground state carries entanglement even after global symmetry is broken by using appropriate witness in the Ising model, and thereby establishes a link between frustration and an extra degree of entanglement [59].

In the presence of transverse field, however, the disentanglement between motional states and spin states becomes imperfect and is accumulated during the adiabatic evolution. Fortunately, the residual entanglement does not have an influence on the probabilities of spin product states measured in the direction of the Ising model axis [37]. Therefore we do not see the effects on the experiments generating the phase diagram shown in section 6.4. The influence of spin-motion coupling becomes noticeable in the witness measurements, since the motional degrees of free-

dom are traced out during the spin state detections. As shown in the blue curves of figure 6.7, the entanglement of the spin states is suppressed because of the remaining spin coupling to motions.

6.6 Scalability of the quantum simulation

As the number of spins N grows, the technical demands on the apparatus are not forbidding [59, 57]. In particular, the expected adiabatic simulation time for the spin models is inversely proportional to the 'critical' gap in the energy spectrum; for instance, in a fully-connected uniform ferromagnetic transverse Ising model in a finite-size system, this gap decreases as $N^{-1/3}$ [71]. Scaling this system to accommodate long ion chains will allow the investigation of critical behavior depending on the system size, which is intractable in classical numerical simulation.

We perform a benchmarking experiment where all interactions $J_{i,j}$ are ferromagnetic regardless of number of spins in the system by tuning the Raman beatnote detuning close to the COM mode. We carefully investigate deviations of experimental simulations from theoretical predictions as the system size increases and discuss possible solutions overcoming the limitations. We observe a crossover from paramagnetic to ferromagnetic spin order, and the crossover sharpens as the number of spins is increased, prefacing the expected quantum phase transition [6] in the thermodynamic limit. We find that particular order parameters of the system can be quite insensitive to the imperfections of the quantum simulations, and the extraction of intensive variables such as the magnetization are much less susceptible

to decoherence compared with full tomographic characterizations of the resulting quantum state.

In the experiment, we produce the strength of $J_{i,j}$ close to 1 kHz by setting the Raman beatnote detuning $\mu \approx \nu_1 + 4\eta_1\Omega$, where ν_1 are the Lamb-Dicke parameter and the frequency of COM motional mode, respectively. The strength of the couplings are pretty uniform among the pairs, since the COM mode dominates the interactions. The non-uniformity in the Ising couplings arises from other vibrational modes, which produce around 30% differences in the strength at the most. We note that for larger detunings, the range of the interaction falls off even further with distance, approaching the limit $J_{i,j} \sim 1/|i-j|^3$ for $\mu \gg \nu_1$ [81, 72].

The experiment is performed according to the adiabatic quantum simulation protocol, as described in section 1.3. We initially start with strong effective transverse field $B_y \approx 5N J_{rms}$ ($N = 2, 3, \dots, 9$) after preparing the ground state of the B_y Hamiltonian. We transfer it to the Ising Hamiltonian with weak transverse field by exponentially ramping down B_y with time constant $\tau = 80 \mu s$. We observe the evolution of state step by step as we proceed the experiment. For the measurements, we use the PMT and obtain the probability P_s of having s spins in state $|\uparrow\rangle$ from a histogram of fluorescence counts, constructed by the more than $\sim 1000 \times N$ times repetition of the experiments [73]. The final states of the adiabatic evolution are the superposition of two perfect FM states $|\uparrow\uparrow \dots \uparrow\rangle$ and $|\downarrow\downarrow \dots \downarrow\rangle$, called GHZ state, since we implement FM couplings for all the pairs of spins and begin with the ground state of the transverse field. Therefore we measure the density matrix of the GHZ state as the simulation evolves. We also use other observables such as

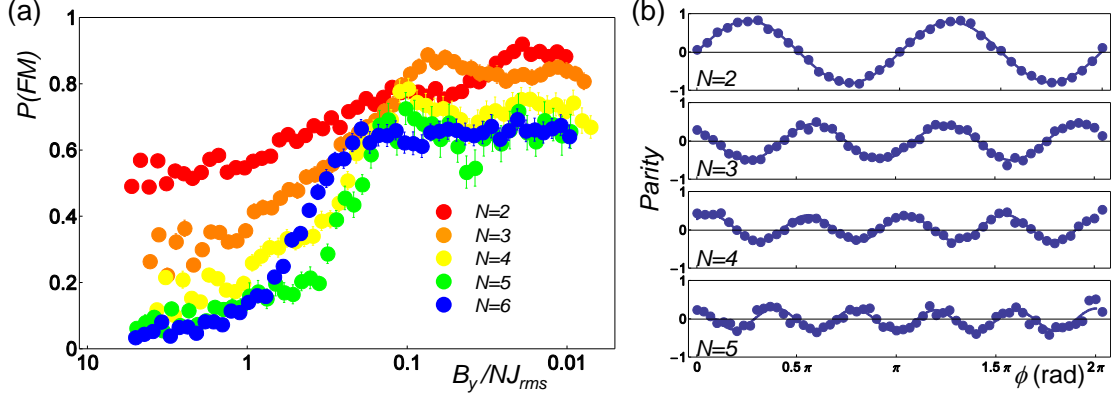


Figure 6.8: Experimental results of adiabatic quantum simulation depending on the system size. Here all pairs of spins have FM interactions. (a) The FM order $P(FM)$ evolutions as the system size increases. Initially $P(FM)$ starts $2/2^N$, since $P(FM)$ is the probabilities of two states $P_{|\uparrow\uparrow\cdots\uparrow\rangle}$ and $P_{|\downarrow\downarrow\cdots\downarrow\rangle}$ over equally distributed 2^N states. As the spin-spin interactions J overpowers B_y ($B_y \rightarrow 0$), $P(FM)$ are developed. Here J is the average strength of all interactions. The red, orange, yellow, green and blue dots represent the experiments for the total number of spins $N=2, 3, 4, 5$, and 6 , respectively. Ideally $P(FM)$ should be close to 1 at the end. However, $P(FM)$ clearly reduces as the number of spins increases in the system from 2 to 6. The sources and amounts of errors are discussed in the text. (b) The parity oscillations for the final states of the simulation depending on the number of spins, obtained from the population difference between the even number of $|\uparrow\rangle$ state and the odd number of $|\uparrow\rangle$ state after applying analysis $\pi/2$ pulse and swipping its phase ϕ . The contrast of the oscillations provide the lower bound of the coherence, the off-diagonal element of the density matrix for the GHZ state $(|\uparrow\uparrow\cdots\uparrow\rangle \pm |\downarrow\downarrow\cdots\downarrow\rangle)/\sqrt{2}$. The coherences decrease to 0.8, 0.47, 0.35, 0.27 much faster than $P(FM)$ as the number of spins increase from 2 to 5, because of spin-motional couplings during the simulation as discussed in the text.

magnetization to characterize the time evolutions and the phase transitions.

We analyze the reliability of the simulation depending on the system size by using the fidelity of GHZ state, $|\langle \psi_{SIM} | GHZ \rangle|^2 = \frac{1}{2}(P_{\downarrow\downarrow\cdots\downarrow} + P_{\uparrow\uparrow\cdots\uparrow}) + |C_{\downarrow\downarrow\cdots\downarrow, \uparrow\uparrow\cdots\uparrow}|$. Here $P(FM) = P_{\downarrow\downarrow\cdots\downarrow} + P_{\uparrow\uparrow\cdots\uparrow}$ and the GHZ coherence $|C_{\downarrow\downarrow\cdots\downarrow, \uparrow\uparrow\cdots\uparrow}|$ is the coefficient of the $|\downarrow\downarrow\cdots\downarrow\rangle\langle\uparrow\uparrow\cdots\uparrow|$ in the density matrix [68]. We measure coherence of GHZ state by observing the contrast of the oscillating parity signals [Figure 6.8(b)], obtained by applying analysis $\pi/2$ pulse with different phase ϕ and taking the differences in populations of the even number bright states and odd number bright states ($P(0) + P(2) + \dots - P(1) - P(3) - \dots$).

Figure 6.8 shows the experimental results of the quantum simulation as the number of spins increases in the system. Initially $P(FM)$ starts $2/2^N$, since $P(FM)$ is the total probabilities of two states ($|\uparrow\uparrow\cdots\uparrow\rangle, |\downarrow\downarrow\cdots\downarrow\rangle$) and the ground state of $B_y \sum \sigma_y^{(j)}$, $|\downarrow\downarrow\cdots\downarrow\rangle_y$ are equally distributed in a total 2^N states in the x -basis. Ideally $P(FM)$ should be close to 1 at the end of the simulation. However, we observe that the final states are increasingly deviated from the ideal situation as the number of spins grows as shown in figure 6.8(a). We also observe that the GHZ coherence decreases much more rapidly than $P(FM)$ shown in figure 6.8(b). After 6 spins, we did not measure any significant GHZ entanglement for the final state due to the large suppression of the coherence compared to the populations. In the following subsections, we discuss the reason of these deviations and we summarize the expected experimental imperfections in quantum simulations as the system size grows.

6.7 Scaling of imperfections

6.7.1 Spin-motion coupling

As discussed in section 3.4, the effective spin-spin coupling Hamiltonian that we assume to describe the system is only valid when the detuning of the beatnote is much larger than the sideband strength. As our detuning is limited by the coherence time of the system, i.e. the need for strong coupling strengths, the spin-motion entanglement does not completely vanish during the simulation. In fact, the spin-motion coupling increases in the presence of the transverse field. The transverse field mixes the spin states along the axis where the spin-dependent force is applied, therefore this coupling induces phonon excitations, modifying the final state from the ideal GHZ state to $(|\uparrow\uparrow\cdots\uparrow\rangle|\alpha\rangle \pm |\downarrow\downarrow\cdots\downarrow\rangle|-\alpha\rangle)/\sqrt{2}$. Here $|\alpha\rangle$ is a motional coherent state and $\langle n \rangle = |\alpha|^2$ increases as the amount of state mixing grows. According to numerical calculations corresponding to the experiment, $\langle n \rangle$ increases to ≈ 0.5 for the five spin experiment. The effective phonon excitation occurs primarily in the early stages of the simulation evolution, where the strength of the transverse field is much larger than the frequency of spin rotations. In the experimental conditions, the Raman beatnote is detuned $\sim 4\eta_1\Omega$ from the COM mode, which results in an increment of $|\alpha|$, because of the required large initial transverse field. However, the population $P(FM)$ and the evolution is not sensitive to these spin-motion couplings.

6.7.2 Diabaticity

The finite ramping speed of parameters in the Hamiltonian leads to excitations out of the ground state and can lead to oscillations in the observed order parameter. This diabaticity in the evolution, along with errors in the initialization to the original ground state is estimated to suppress the final value of $P(FM)$ by $\sim 4\%$ for $N = 5$ shown in the orange line of figure 6.9(a). As discussed in section 6.7.2, the diabaticity is related to the minimum gap over the trajectory of the Hamiltonian as well as the ramping time. We note that the gap between the ground and first-excited state of the fully-connected uniform FM model scales as $N^{-1/3}$, implying that the simulation time by a factor of ten when the number of spins grows by a factor of one thousand.

6.7.3 Spontaneous Emission

One of major error sources is the spontaneous emission from Raman beams which amounts to a $\sim 10\%$ spontaneous emission probability per spin in 1 ms for a detuning of $\Delta \approx 2.7$ THz [74]. Spontaneous emission dephases and randomizes the spin state, and thus introduces entropy into the system. In addition, each spontaneous emission event populates other states outside of the Hilbert space of each spin with a probability of $1/3$. Spontaneous emission errors grow with increasing system size, which also suppresses $P(FM)$ order with increasing N , as seen in figure 6.9. We theoretically estimate the suppression of $P(FM)$ due to spontaneous emission by averaging over quantum trajectories and solving density matrix equations to be $\sim 5\%$ for $N = 2$ spins and $\sim 13\%$ for $N = 5$ spins. The error contributions are the

same for both populations and coherences.

6.7.4 Intensity fluctuations

Intensity fluctuations on the Raman beams during the simulation induce an fluctuating AC Stark shift on the spins. The AC stark shifts produce an imbalance on the blue and red sideband detuning, which give rise to imperfections in the spin-spin interactions. According to our numerical calculations, the imbalance fluctuations of ~ 150 Hz ($\sim 1.5\%$ intensity fluctuations in our experimental conditions) can explain the suppressions of $P(FM)$ at the end of the experimental simulations shown in figure 6.9. We investigate the non-uniformity of the laser beams that induces different AC shifts on the spins by measuring the AC shift on each location, which is introducing position dependent B_z -field with at most ~ 200 Hz difference. According to the numerical calculation, the additional small B_z -field does not noticeably suppress $P(FM)$.

6.7.5 Detection Errors

Imperfect spin detection efficiency contributes 5–10 % uncertainties in $P(FM)$. Fluorescence histograms for $P(0)$ and $P(1)$ have a $\sim 1\%$ overlap (in detection time of 0.8 ms) due to off-resonant coupling of the spin states to the $^2P_{1/2}$ level. This prevents us from increasing detection beam power or photon collection time to separate the histograms. In the experiment, the average photon number from a single bright spin is 12. The uncertainty in fitting the observed fluorescence histograms to

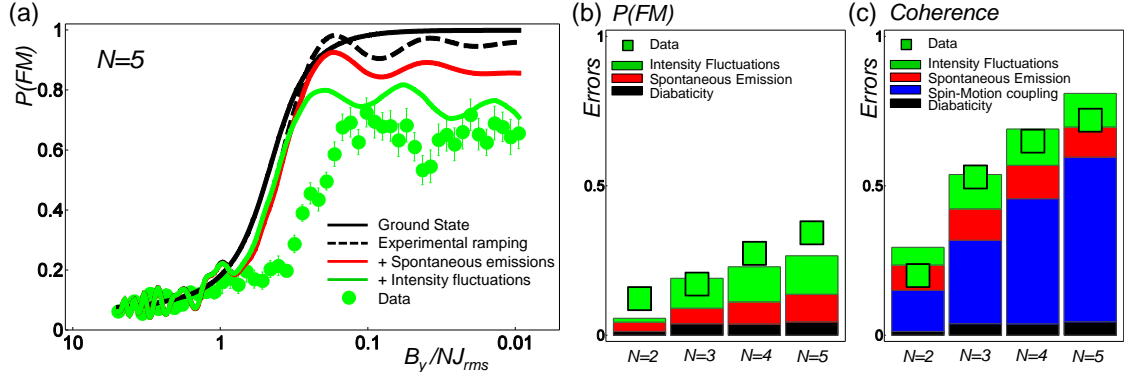


Figure 6.9: (a) The comparison of experimental results of $P(FM)$ to the theoretical expectations including various imperfections of experiments for the 5 spins. The black line represents the evolution of the perfect adiabatic evolution, and the dashed line shows the actual time evolution including the actual ramping of the transverse field with the imperfections of initial state preparations. The red line is obtained from the theory with spontaneous emissions and the green line is calculated by adding intensity fluctuations of 1.5 %. The overall populations of $P(FM)$ are in agreement with the green theoretical curve including all the above mentioned imperfections. The horizontal shift B_y/J comes from the inaccuracy of the calibration that is not fully understood yet. (b) The amount of errors in $P(FM)$ (the diagonal parts of the density matrix) from the ideal ground states for the case of $N=2,3,4$ and 5. (c) The amount of errors in coherence (the off-diagonal parts). In both (b) and (c), the green squares represent the total errors measured in the experiment and the bars illustrate the numerically estimated errors from the various sources of experimental imperfections. The black, red and green bars show the error amounts from non-perfect adiabatic evolutions, spontaneous emissions and intensity fluctuations. The blue bars stand for deviations from the spin-motion couplings. The spin-motion coupling reduces the coherence significantly as the system size grows, while it does not have any influence on the $P(FM)$.

determine $P(s)$ increases. The histograms are also affected by the intensity fluctuations of detection laser beams and the finite widths. This problem can be eliminated by detecting each spin individually with an imaging detector.

Figure 6.9 (a) shows the experimental results and the theoretical calculations including a few steps of imperfections discussed above for $N=5$ spin case as an example. In the population $P(FM)$ also shown in figure 6.9 (b), the main deviations come

from the spontaneous emissions and the intensity fluctuations. As discussed, small amounts of intensity fluctuations degrade the performance of the experimental simulations. One of the solutions for those imperfections is to implement a high power laser with a detuning far from the 2P energy levels, which would minimize spontaneous emission while maintaining the same level of Ising couplings. This would also allow versatility in varying the Ising interaction (together with the effective external field) during the simulation, as the differential AC stark shift between spin states is negligible for a sufficiently large detuning. The coherence time increases in the absence of spontaneous emission, allowing for a longer simulation time necessary to preserve adiabaticity as the system grows in size. Recently Raman transitions have been driven using a mode-locked high power pulsed laser at a wavelength of 355 nm, which is optimum for $^{171}\text{Yb}^+$ wherein the ratio of differential AC Stark shift to Rabi frequency is minimized and spontaneous emission probabilities per Rabi cycle are $< 10^{-5}$ per spin [51, 75].

Figure 6.9(c) shows the measured and numerically estimated errors in the magnitude of coherence, $|C_{\downarrow\downarrow\ldots\downarrow,\uparrow\uparrow\ldots\uparrow}|$, at the final state of the quantum simulation. We can clearly see that the errors of the coherence much more rapidly increase than those of $P(FM)$. According to the numerical study, the dominant source for the errors of $|C_{\downarrow\downarrow\ldots\downarrow,\uparrow\uparrow\ldots\uparrow}|$ is the non-vanishing spin-motion couplings in the experimental simulation, shown as the blue area of the figure 6.9(c). In principle, we can eliminate the effect of the spin-motion coupling by alternating the transverse field and Ising interactions [76]. The adiabatic evolution can be discretized by the Trotter

expansion written by

$$\begin{aligned}
U_{TIM}(\tau) &= T \exp \left(-i \int_0^\tau dt' [H_I(t') + H_B(t')] \right) \\
&\approx [\exp(-iH_I(\tau/N)) \exp(-iH_B(\tau/N))]^N, \tag{6.2}
\end{aligned}$$

where H_I and H_B are the Ising Hamiltonian and the transverse field Hamiltonian, respectively. In the experiment, we can choose τ/N as the special duration ($1/\delta$), where the spin-motion couplings vanish. We can also reduce the errors of the Trotter expansion by increasing the Raman beatnote detuning δ from the motional mode.

In condensed matter, phase transitions are typically described in terms of order parameters or correlations instead of the density matrices of particular states. We use a absolute magnetization $\langle |m| \rangle = \sum_m |m|/N P(m)$ per site along the Ising direction. Actually we rescale the magnetization $\langle |m| \rangle$ from 0 to 1 regardless of the number of spins to make a fair comparison even for small size systems. We find that the deviation between experiment and theory for this order parameter does not grow substantially as the system is scaled up in size. Figure 6.10 shows the scaled magnetization, $\langle |m_S| \rangle$ for $N = 2$ to $N = 9$ spins, showing a final value of $\sim 80\%$ (figure 6.10) regardless of number of spins. Moreover as shown in figure 6.10(a) we observe the sharpening of the crossover curves from paramagnetic to ferromagnetic spin order with increasing system size. The continued sharpening of this transition is of great interest to the understanding of finite size effects in phase transitions and can be used to compare various numerical techniques in studying critical phenomena.

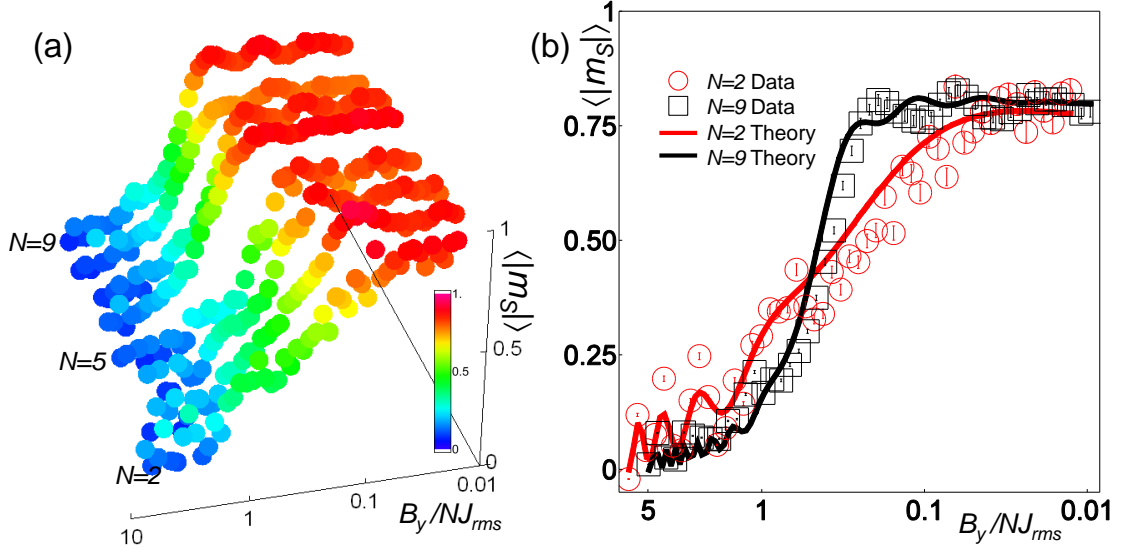


Figure 6.10: (a) Scaled average absolute magnetization per site, $\langle |m_S| \rangle$ vs B/NJ_{rms} is plotted for $N = 2$ to $N = 9$ spins. As B/NJ_{rms} is lowered, the spin ordering undergoes a crossover from a paramagnetic to ferromagnetic phase. The crossover curves sharpen as the system size is increased from $N = 2$ to $N = 9$, anticipating a QPT in the limit of infinite system size. The oscillations in the data arise due to imperfect initial state preparation and non-adiabaticity due to finite ramping time. (b) Magnetization data for $N = 2$ spins (circles) is contrasted with $N = 9$ spins (squares). The data deviate from unity at B/NJ_{rms} by $\sim 20\%$, predominantly due to spontaneous emissions in Raman transitions and intensity fluctuations of Raman laser beams, as discussed in the text. Here, the theoretical time evolution curves (red line for $N = 2$ and black line for $N = 9$ spins) are calculated by averaging over 10,000 quantum trajectories.

6.8 Conclusion and Outlook

Trapped atomic ions represent a promising platform for the quantum simulation of intractable Hamiltonian systems. There have been several theoretical proposals in this direction, largely following schemes in the realm of quantum computing, and recent experiments have shown that the system can be scaled to a degree where all classical simulations become impossible [59, 70, 77]. This paper has shown both theoretically and experimentally that the quantum simulation of quantum magnetism and the emergence of spin order can be controlled through external laser beams up to 9 spins and can further be scaled to much larger numbers of spins. The stable confinement of larger numbers of ions may require novel ion trap architectures such as anharmonic axial potentials [78] for a linear chain or two-dimensional trap geometries [79, 80], but there are no known fundamental limitations in this scaling. As discussed here, for a fixed level of total laser power, the errors associated with decoherence from spontaneous Raman scattering from the lasers is expected to grow only as $N^{1/3}$ for the linear chain, holding errors from phonon creation and diabatic transitions to excited states at fixed levels. Alternatively, all of these errors can be held at a fixed value independent of N so long as the laser power increases by $N^{1/3}$. In either case the required time for adiabatic ramping grows as $N^{1/3}$, so slowly drifting errors such as (real) magnetic fields and motional heating of the ions must be kept under control for very large N as discussed in the supplementary information of Ref. [59]

This system can also be extended to Heisenberg or XYZ spin models [81] or

spin-1 systems by adding a few more laser beams. As the system grows, the transverse motional modes that mediate the Ising couplings can give rise to higher levels of frustration and complex phases of magnetic ordering. For instance, by preparing a ground state of a highly frustrated collection of trapped ion spins, it should be possible to create localized topological excitations and guide their transport through the system [82]. This example of topological matter is of great interest for the robust representation and manipulation of quantum information [83, 84]. But more generally, the trapped ion system is poised to be the first to determine ground state features of Hamiltonians where no solution can be obtained otherwise.

Chapter 7

Quantum Simulation of the Devil’s Staircase

7.1 Introduction

Recent efforts in quantum simulation, motivated by its promise as a tool for advancing understanding of condensed matter systems, solving difficult optimization problems, and simulating other physical systems while providing an in-situ insight previously unattainable have seen significant advances. These include simulation of the nearest -neighbor anti-ferromagnetic Ising model [85], and the long-range anti-ferromagnetic Ising model. Recent theoretical interest in the simulation of the complete Devil’s Staircase [86] using cold, trapped ion quantum simulators [87] have motivated us to simulate this system for six and ten spins.

In this chapter I report a quantum simulation experiment¹, similar to those in chapter 6. In this experiment a linear chain of trapped, cold ions are irradiated by lasers far detuned from resonant transitions to simulate and control an Hamiltonian of AFM coupled Ising spins with long range, frustrated interactions. We add to this effective interaction a combined axial and transverse simulated fields, and by scanning the strength of the axial field we explore $N/2$ phase transitions in the ground state of the zero transverse field spin chain of N spins. Site resolved imaging, as described in section 4.4.8 allows us to extract ground state order parameters and

¹Manuscript in preparation.

state probabilities, amplified over the background by the post-processing techniques of section 4.4.8. We compare the experimental results to theoretical predictions.

7.2 Overview

We perform a quantum simulation of the AFM Ising model with a tunable axial biasing field B_a :

$$H = \sum_{i,j}^N J_{ij} \sigma_x^i \sigma_x^j + B_x \sum_i^N \sigma_x^i + B_y \sum_i^N \sigma_y^i \quad (7.1)$$

Where H is the simulated Hamiltonian of the system, σ_x^i the Pauli spin operator on spin i , and $J_{i,j}$ is the spin-spin coupling between spin i and spin j as defined in 3.22. The $|\uparrow\rangle$ and $|\downarrow\rangle$ states are defined as presented in 2.4, and the ions are radially confined with a transverse collective COM mode frequency $\omega_1 = 2\pi 4.863 \text{ MHz}$, and a tilt frequency $\omega_2 = 2\pi 4.813 \text{ MHz}$. This Hamiltonian has been Identified as a physical model for several real world systems, such as graphite intercalation compounds, and exhibits the much investigated complete Devil's staircase behavior for a macroscopic number of spins [88].

Just as in the experiments described in chapter 6, we will initialize the spin system in the ground state of a trivial Hamiltonian, where the magnetic fields overwhelm the \mathbf{J} component of the Hamiltonian. Unlike the simulations of chapter 6, we cannot simply rotate the spins to align with transverse field B_y , rather we will have to apply a Raman pulse that rotates the spins into the superposition of $B_x + B_y$. Thus, for each value of B_x the phase of the initialization pulse relative to the simu-

lation frequency phases will be different. For our selected simulation pulse phases, the phase of the initialization pulse will be

$$\theta = 180^\circ - \tan^{-1}(B_x/B_y) \quad (7.2)$$

As all components of \mathbf{J} are positive for our red beatnote detuning from the transverse COM, initializing in the ground state (along the total B field) will simulate AFM coupling.

After initializing, we will apply all components of the Hamiltonian simultaneously, and proceed to ramp down B_y with an exponential envelope (with no offset). The duration of the time constant of the envelope is a compromise - the ideal time constant would satisfy the adiabatic condition [89] with a large safety margin. However, we are constrained by the coherence time of the ions, which for us was found to be roughly 3 ms. Therefore, we chose our time constant so as to achieve as low a B-field as possible in the available time without causing severe oscillations or excitations towards the end of the simulation.

Finally, we apply a Raman rotation to measure the spin state in the measurement basis (the z-axis of the Bloch sphere). Repeating this experiment with different B_x values allows us to map the phase diagram of this Hamiltonian.

7.3 Experiment

As described in section 3.4, we control the dynamics [57] by applying far detuned global Raman beams with a wavenumber difference δk along the transverse

Coupling	Strength
$J_{1,2}$	660 Hz
$J_{1,3}$	368 Hz
$J_{1,4}$	235 Hz
$J_{1,5}$	158 Hz
$J_{1,6}$	106 Hz
$J_{2,3}$	621 Hz
$J_{2,4}$	373 Hz
$J_{2,5}$	242 Hz
$J_{2,6}$	158 Hz
$J_{3,4}$	609 Hz
$J_{3,5}$	373 Hz
$J_{3,6}$	235 Hz
$J_{4,5}$	621 Hz
$J_{4,6}$	368 Hz
$J_{5,6}$	660 Hz

Table 7.1: Calculated spin-spin couplings for 6 ions with our trap, detuning, and laser intensity parameters

(perpendicular to chain alignment - “x” direction) direction of the ion chain.

To create the the spin-spin coupling matrix \mathbf{J} , we detune two Raman beams 80 KHz to the blue and red of the COM mode, so that the beatnote μ is red of the COM mode. This is done while verifying that the strengths of the beams drive sideband transitions on a single ion with equal strength, are symmetrically detuned from the carrier transition, and the beams are centered on the center of the spin chain (the position of a single ion in the trap).

To diagnose the intensity of our 355 nm center wavelength 80 MHz pulsed laser Raman beams, we measure a two ion spin-spin coupling strength of 66.5 KHz . Assuming equal intensity across our ion chain, the spin-spin coupling matrix \mathbf{J} is calculated and presented in table 7.1. The single ion RSB or BSB strength for this intensity on resonance is calculated to be 23 KHz , so our detuning $\delta \approx 3\eta\Omega$.

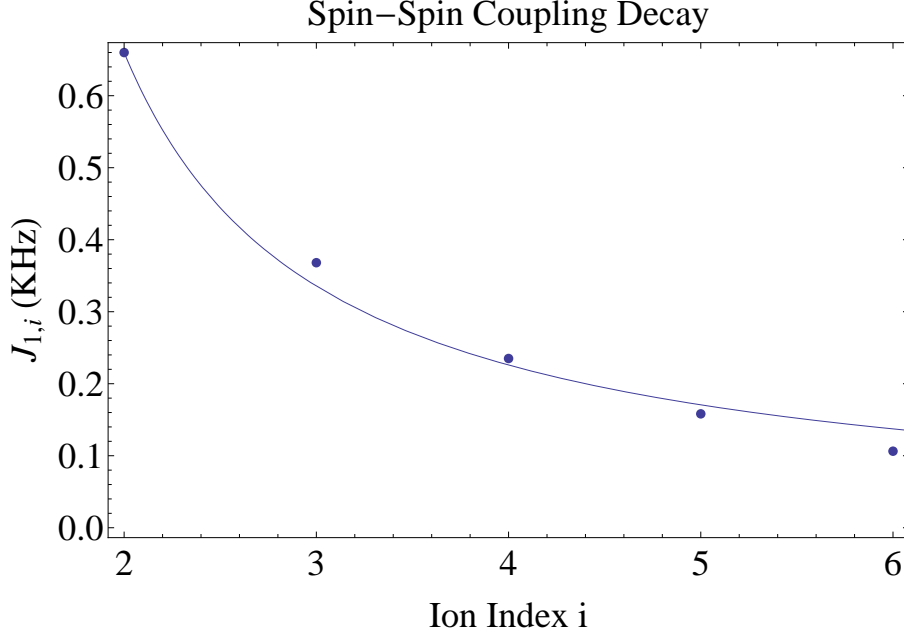


Figure 7.1: Power law fit for the for the first ion. The curve was fitted with only the exponent as a parameter.

As in our other experiments where we tuned to the red of the COM, the couplings are decaying according to a power law with exponent α

$$J_{i,j} \approx \frac{J_{i,i+1}}{|i-j|^\alpha} \quad (7.3)$$

This exponent α depends only on trap conditions - it is a feature of the motional mode bandwidth. For our current trap conditions and six ions, $\alpha = 0.976$, as shown in figure 7.1. In previous work, we have explored the effect of changing this parameter on the correlations of the final AFM state for $B_x = 0$.² α characterizes the range of the spin-spin coupling, and for longer range AFM interactions we can expect to see more frustration in the ground state with smaller energy gaps.

²Accepted for publication in “Science”, R. Islam et al *Emergence and Frustration of Magnetism with Variable-Range Interactions in a Quantum Simulator*

The characteristic power law decay arises due to the non-negligible contribution of the tilt mode as well as smaller contributions from the remaining transverse x-modes. y-modes are suppressed by beam alignment and control of the trap principal-axes, so that the y-mode sidebands are at least 10 times suppressed compared to the x-modes. We further suppress the y COM mode by lowering its frequency relative to the x COM mode, by adjusting trap anisotropy.

As described in 4.4.6, to generate the Raman beams we use two lasers, modulated by two AOMs. The first AOM is driven by an oscillator stabilized by an error signal from the beating of a Microwave source and the frequency component of the pulsed laser near the qubit frequency. The second AOM is driven by an AWG. During the simulation, the AWG drives the AOM with three different frequencies: one to drive the qubit Rabi oscillations, and two symmetrically detuned from this central frequency to drive the Mølmer-Sørensen spin-spin coupling gate. It is only when these frequencies interfere on the ion with the light modulated by the first AOM that transitions are driven.

The AWG and the driver of the stabilized AOM are phase locked to a Rubidium clock, outputting a reference signal at 10 MHz . We select and define the Pauli vector component via the relative phase of the different beatnotes. We set the phases as elucidated in table 7.2

As demonstrated in section 3.4 it is only the phase difference of the BSB and RSB ϕ_m^i that affects the Mølmer-Sørensen spin-spin coupling. Therefore, we arbitrarily set the phase of the RSB to 0, and set only the phase of the BSB to control the axis of the interaction. As ϕ_m^i is equal to half the difference of BSB and

Pulse	Phase	Result
Initialization	θ	$B_x \sigma_i^x + B_y \sigma_i^y$
B_x	90^0	σ_i^x
B_y	0^0	σ_i^y
RSB	0^0	Combined with BSB we get
BSB	180^0	
Final	90^0	
		$J_{ij} \sigma_i^x \sigma_j^x$
		σ_i^y

Table 7.2: Pulses for axial simulation experiment. Initial pulse θ is defined in 7.2. For example, with no axial field $\theta = 180^0$. The final rotation of the spins into the measurement basis can alternatively be set to 90^0 , as this will only result in flipping the spins in the final state and does not change the physics.


RSB phases, setting θ to 180^0 sets the interaction axis to be the x-axis. The control panel for the AWG chapter phases, frequencies and amplitudes is shown in figure 7.2.

All the lasers used in the experiment are global - we do not use individual addressing. This simplifies optical setup and reduces sensitivity to beam steering, however this prevents us from measuring the elements of the density matrix that require operations that are not a global rotation.

The experiment proceeds as follows. The ions are Doppler cooled for $\sim 3\text{ms}$, and optically pumped to the $|\downarrow\rangle$ state by a $8\mu\text{s}$ laser pulse resonant with the $^2S_{1/2} |F=1\rangle \rightarrow ^2P_{1/2} |F=1\rangle$ transition, as shown in figure 2.3.

30 cycles of alternating red-sidebands resonant with the x COM mode and $3\mu\text{s}$ long optical pumping pulses reduce the occupation number of this phonon mode to ~ 0.1 phonons, so that state is initialized in the spin as well as motion sub-spaces.

We then rotate our spins to the trivial ground state of a Hamiltonian dominated by a transverse magnetic field, where our initial transverse field B_y is 5 times

Auto Carrier 

AWG Exp/Linear Simulation

Frequency (MHz)

204.865157505

Car

199.804500001

Red

209.925815

Blue

Phase (Deg)

180

-1st Car

90

- Trans. B field

180

- J

0

- Axial B field

180

-2nd Car

Duration (ms)

0.0026

-1st Car

0.0001

-Flat line

0.1

-QSim

0

-QSim 2

0.0001

-Flat line

0.0014

-2nd Car

Amplitude (Max2047)

200

-1st Car

0

-Initial Bfield

1E+11

-Ramp Rate
(1step/ns)

500

-Red SB

0

-Blue SB

0

-2nd Car

0

-Axial B field

Figure 7.2: Control panel for quantum simulation AWG waveform in the Labview control program. The phase of **J** is the phase of the BSB.

larger than the largest spin-spin coupling J_{MAX} .

We ramp down the transverse field B_y with an exponential time constant of $600\mu\text{s}$. This value was found by numerically evolving the Schrödinger equation (SE) for our experimental parameters and maximizing the resemblance of the magnetization order parameter of the evolving state to that of the adiabatic perfect ground state of Hamiltonian 7.1 at time t of the simulation. The magnetization order parameter is defined here as $M = 1/2 + \frac{n_{|\uparrow\rangle} - n_{|\downarrow\rangle}}{2N}$.

When the ramping is complete, we rotate our spins back to the measurement basis, and measure each spin using a resonant beam with a Princeton PI-MAX 3 ICCD with a 3ms exposure time, as described in 4.4.8. Thus, we are able to measure the distribution of spin eigenstates for this process, with a $\sim 93\%$ readout fidelity per ion. This fidelity is reduced from the theoretically attainable fidelity of $\sim 99.5\%$ by electronic readout noise and the 0.23 numerical aperture of the imaging system. In order to correct the biasing of the state probabilities, we redistribute them as described in 4.4.8.

For 6 ions, we map out a phase diagram by stopping the simulation at three different final times of $306\mu\text{s}$, $960\mu\text{s}$ and 3ms corresponding to B_y/J_{MAX} values of $\sim 3.00, 1.01$ and 0.034 . We measure the final state 4000 times for 61 equally spaced values of B_x/J_{MAX} between 0 and 4. Figure 7.3 displays the phase diagram of the magnetization order parameter. The surface plot is the perfect adiabatic order parameter for the ground state, whereas the points are experimental results. The theoretical plot shows three first-order [88] phase transitions at $B_y/J_{MAX} = 0$. We have also attempted to repeat the experiment for points close to the phase transition

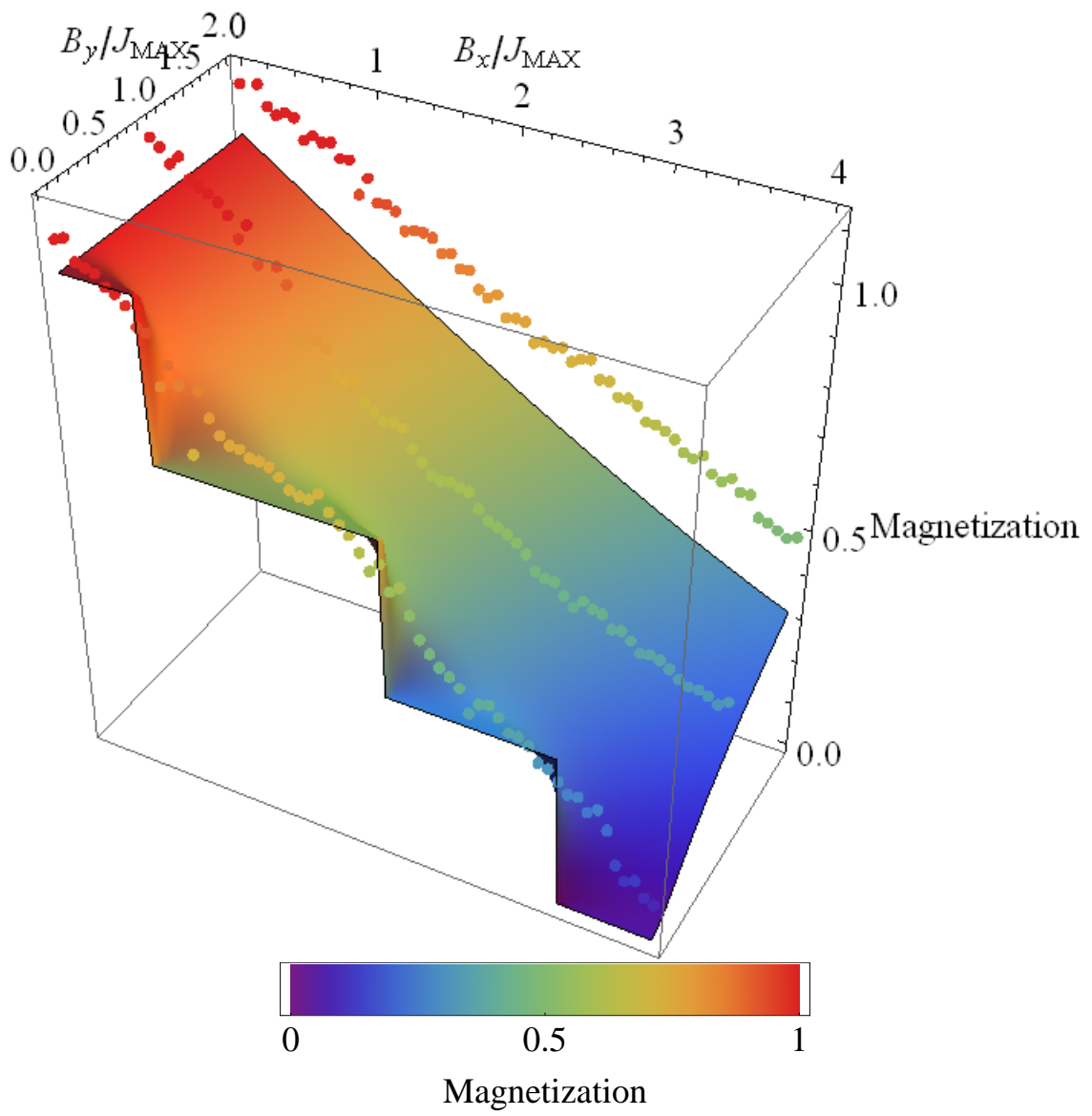


Figure 7.3: Magnetization Phase Diagram for 6 Ions.

once our measurements indicated their location. However, our control of the system parameters did not seem to be stable enough over the duration of the data taking.

Our dominant measured states at $B_y/J_{MAX} \approx 0$ are displayed in figure 7.4 and further investigated. Comparing only the dominant states to theoretical evolution of Schrödinger equation (solid lines) we see the data for the dominant states closely follows. However, the simulation is not sufficiently adiabatic and the data is too noisy to clearly show the sharpness of the phase transitions.

This is accentuated when we compare the magnetization parameter for the adiabatic solution, the evolved solution and the data, as in figure 7.5.

The lack of adiabaticity at the phase transition can be investigated theoretically from multiple aspects. One aspect is that of the adiabaticity parameter, which for our system roughly corresponds to the inverse of the minimum energy gap between the ground state and the first coupled excited state for the trajectory of the simulation [22]. For the Hamiltonian 7.1, there are eigen-energy crossings zero at the phase transitions, as can be seen in figure 7.6 and 7.7.

Another interesting feature of the phase transitions is its relation to an inverse pseudo-temperature. Currently, there is ongoing theoretical and experimental investigation of thermalization in closed, coherent quantum systems [90]. According to the currently developing Eigenstate Thermalization Hypothesis (ETH)³ [91], some classes of closed quantum systems display steady-state observables that correspond to the micro-canonical expected observables for analogous classical systems. For the Hamiltonian at hand, we will see that in the low axial field limit the state

³I would like to thank Chao Shen for introducing me to this work.

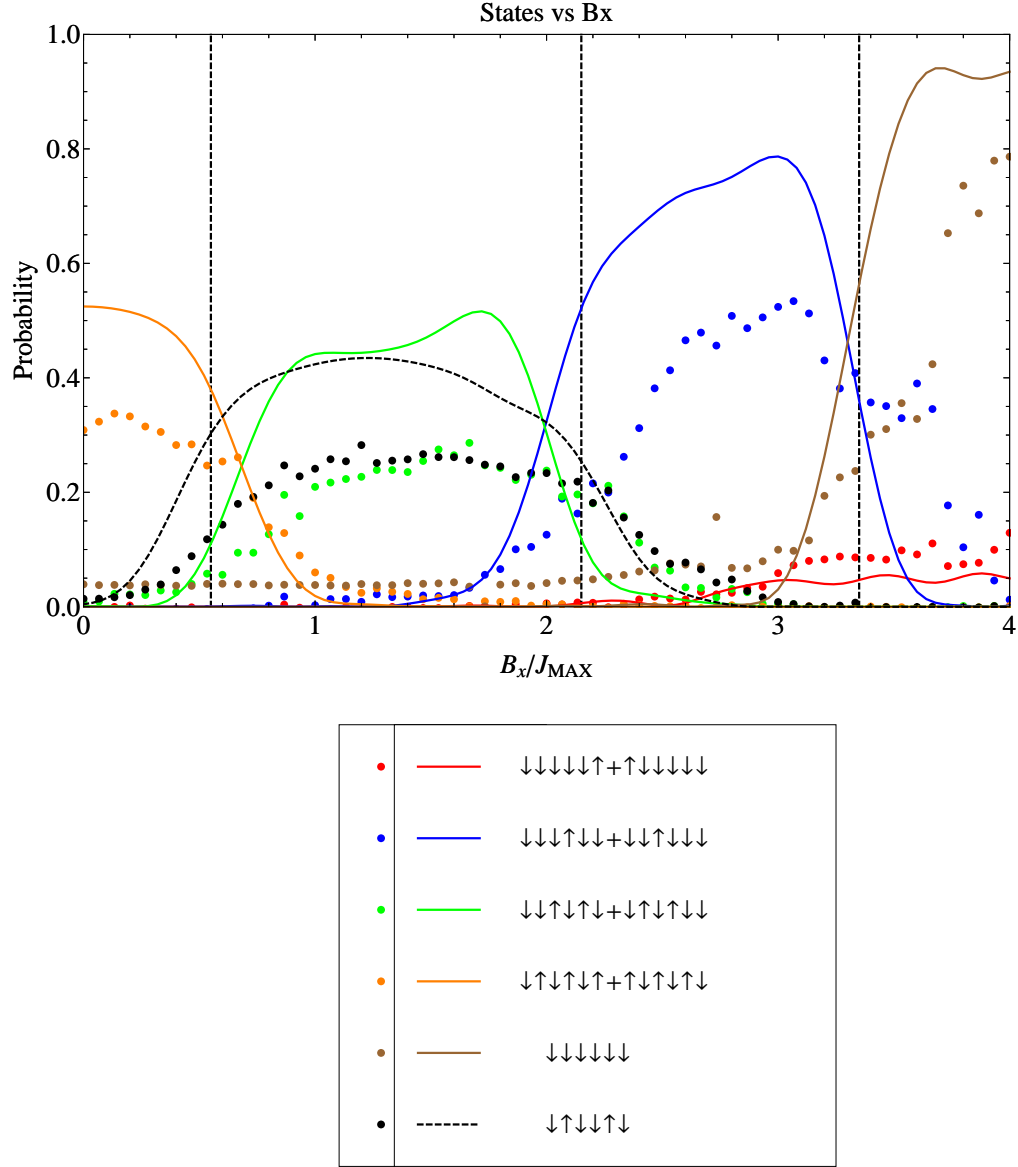


Figure 7.4: Results and simulation of dominant states. The phase transitions in the adiabatic limit are marked with dashed lines. The non-adiabaticity causes the states to bleed out of their phase in the adiabatic case. Some excited states are populated significantly. The red and green curves and data are noticeably excited states for their respective regimes. The first excited state for each stair is a kink in the ground state - the spins are all flipped relative to the ground state at a point in the spin chain that requires the least energy. Typically this is close to the edge chain, as the couplings there are weakest.

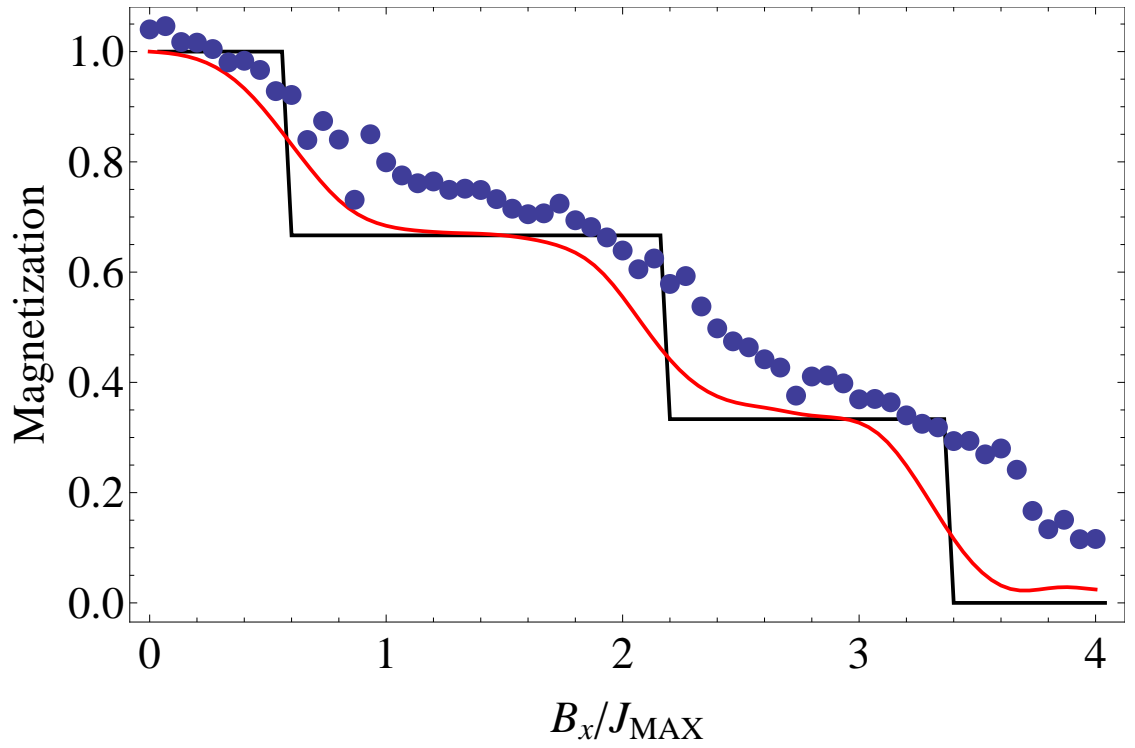


Figure 7.5: 6 ion staircase. Black solid line is perfect adiabatic magnetization, red solid line is numerically integrated Schrödinger equation, and dots are calculated from data.

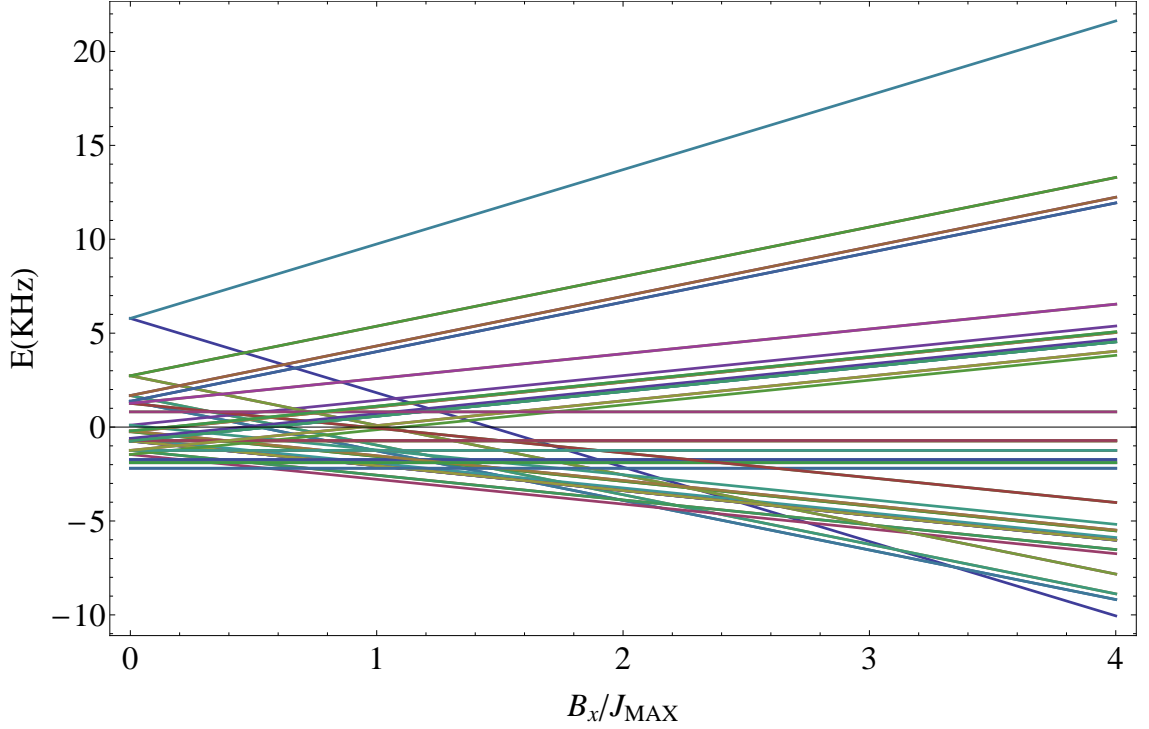


Figure 7.6: Complete eigen-energy spectrum for our Hamiltonian. On the left hand side, the pure AFM case, the lowest energy states are the AFM states, which are degenerate, and the highest states are the FM states. As the axial bias is increased, the FM states degeneracy is lifted. The FM state counter aligned to the field increases in energy and remains the highest, while the FM state aligned with the field becomes the lowest energy state at high axial field limit. At the high axial field limit, the energy states converge into 6 degenerate levels, corresponding to number of spins aligned with the field.

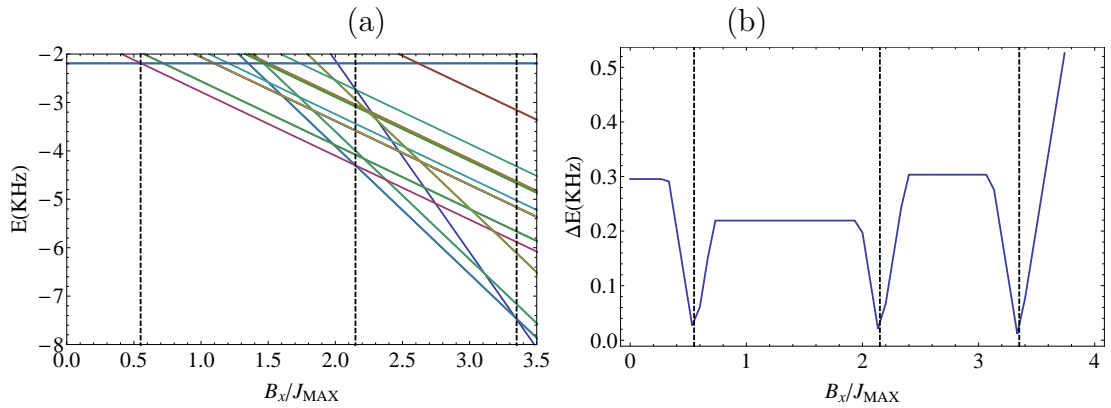


Figure 7.7: (a) Low lying energy levels and crossing points. The dashed lines mark the energy crossings. (b) Energy difference between the two lowest lying states. These lead to the first-order transitions seen in 7.5

probabilities will be occupied with a probability that is roughly proportional to an exponential function of the energy of the eigenstate:

$$P_i = e^{-(E_i - E_0)T} \quad (7.4)$$

Where E is the energy of the state, E_0 is a normalizing factor, and T is the inverse pseudo-temperature. By fitting to the simulated histograms, we can extract T for the final states at all B_x values and $B_y = 0$, as shown in figure 7.8. For six ions, this treatment is not very convincing, as only the first peak aligns itself with the first phase transition. Nevertheless, I will use this treatment to define a pseudo-temperature lowering filter. The filter will succeed to amplify the dominant ground state in the regime where the pseudo-temperature picture is not valid as well, as long as the most dominant state is the true ground state - a reasonable assumption when $B_y = 0$.

We define an amplifying parameter A , which for $A=1$ leaves the probabilities unchanged, and for increasing A will suppress the weaker states compared to the most dominant states. For each state probability for a given B_x and B_y , we define a new probability $P'_i = P_i^A$. Then $\sum_{i=1}^N P'_i$ is renormalized to 1. The effect can be compared to removing excess energy from the system, as can be seen in figure 7.10. In this figure, we compare the effect of increasing A for a simulated final evolved state to increasing the total simulation time while keeping the ratio of simulation time to exponential decay time constant fixed. Starting with a simulated state from the evolved Schrödinger equation with $0.8 \mu\text{s}$ time constant and our experimental

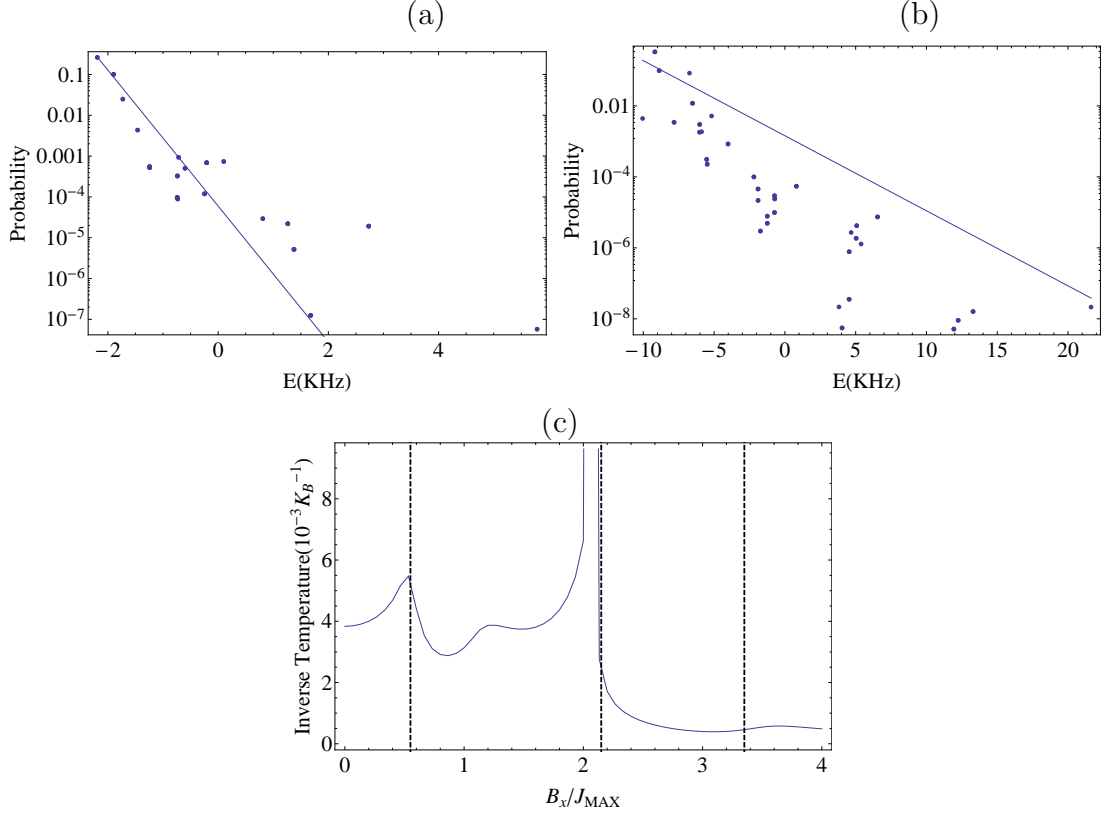


Figure 7.8: (a) Exponential fit of probability of state as a function of state energy, for $B_x = 0$. The fit slope is the inverse pseudo-temperature. (b) Exponential fit for $B_x/J_{MAX} = 4$. (c) The temperature coefficient for all fits. The fit fails rather quickly after showing a correspondence to the first phase transition. Phase transitions are marked with dashed lines.

J, we gradually increase A , and then compare the individual states for increasing A and decay time. Scaling the A axis for all states and values of B_x equally, we see that for most values of B_x the amplified and the slowed evolution states match well.

Applying the filter to our data with increasing amplification (or “cooling”), we can retroactively slow down the simulation. Figure 7.9 demonstrates this effect.

We repeat the same experiment, this time for 10 ions, and only for a final simulation time of 3 ms. Our initial value of B_y is set to $3J_{max}$, and we perform the

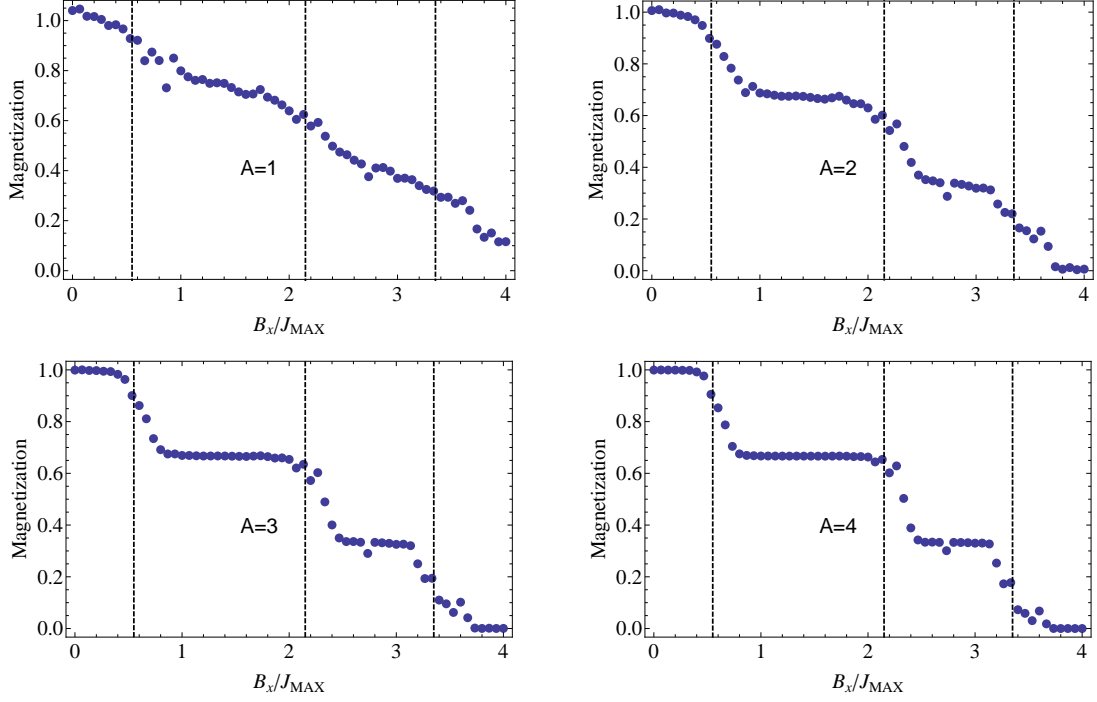


Figure 7.9: Power filter with increasing strength on 6 ion magnetization for $B_x = 0$. When filter strength is $A=1$, the state probabilities are unchanged. When $A=4$, the adiabatic magnetization staircase emerges from the data.

adiabatic simulation procedure for $B_x/J_{MAX} = 0 \rightarrow 5.5$, in step of 0.05, and repeat each simulation 4000 times. As \mathbf{J} is of the same order of magnitude and range as before, as shown in figure 7.11, we can expect to see smaller energy gaps. As we cannot extend simulation time, the expected effect will be much worse diabaticity, i.e. stronger excitation of low lying energy states. We can also expect a lower ratio of signal to noise, as decoherence and detection error for overall state will increase for a larger number of spins. This can be seen in a comparison of our detected states to simulated states in figure 7.12. Here we must rescale the y-axis for the data to compensate for different scales for data and theory.

Interestingly, for 10 ions the pseudo-temperature treatment works far better. As seen in figure 7.13, the exponential fit lies next to many more points, improving

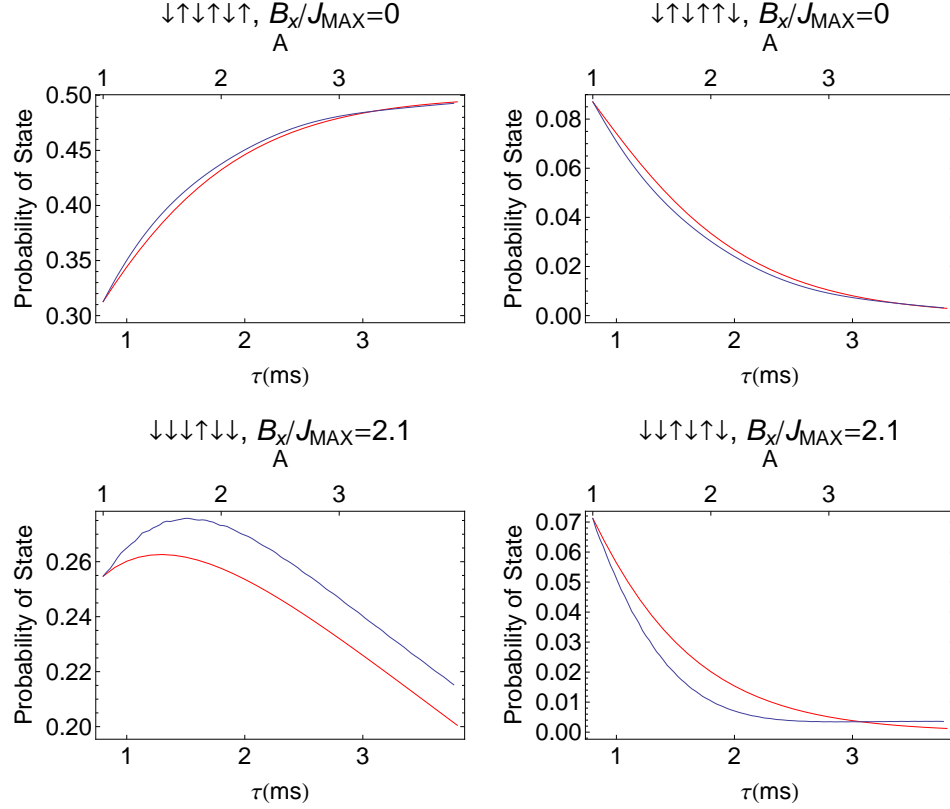


Figure 7.10: Figure above demonstrates effect of power filter versus improved adiabaticity, for two states for two values of B_x . Red line is power filter on $0.8 \mu\text{s}$ evolved state. Blue line is evolved state with increasing exponential decay constant τ , with fixed ratio of $\frac{\tau}{T_{final}}$. For some values of B_x this procedure will fail, as close to a phase transition there may be population oscillations.

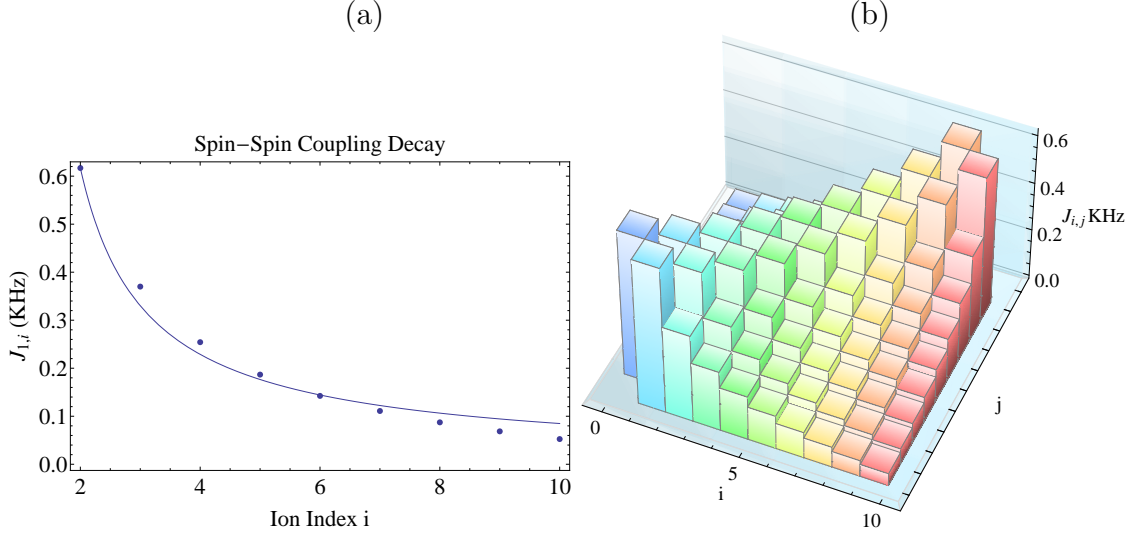


Figure 7.11: (a) Power law decay for 10 ions, shown for spin 1. (b) The \mathbf{J} coupling matrix. Note that it is symmetric across the chain and across the diagonal. The diagonal elements are meaningless.

the validity of the fit. When we extract all the pseudo-temperature coefficients for the B_x domain of the simulation, we see more temperature cusps corresponding to the adiabatic regime phase transitions.

Applying the same filtering method to our 10 ion magnetization data, we see how the staircase emerges again. However, for this data the filtering is much more aggressive, as could be expected for a more diabatic simulation. It is less successful as well, which is likely due to increased overall noise and decoherence [92].

7.4 Conclusion

Despite the technical challenges faced by this experiment, the sharp phase transitions at near zero transverse field can be observed. Here we rely on the fact that when our transverse field is extinguished, the dominant state will be the ground state. As can be seen in figure 7.14, the staircase signal can be extracted from the

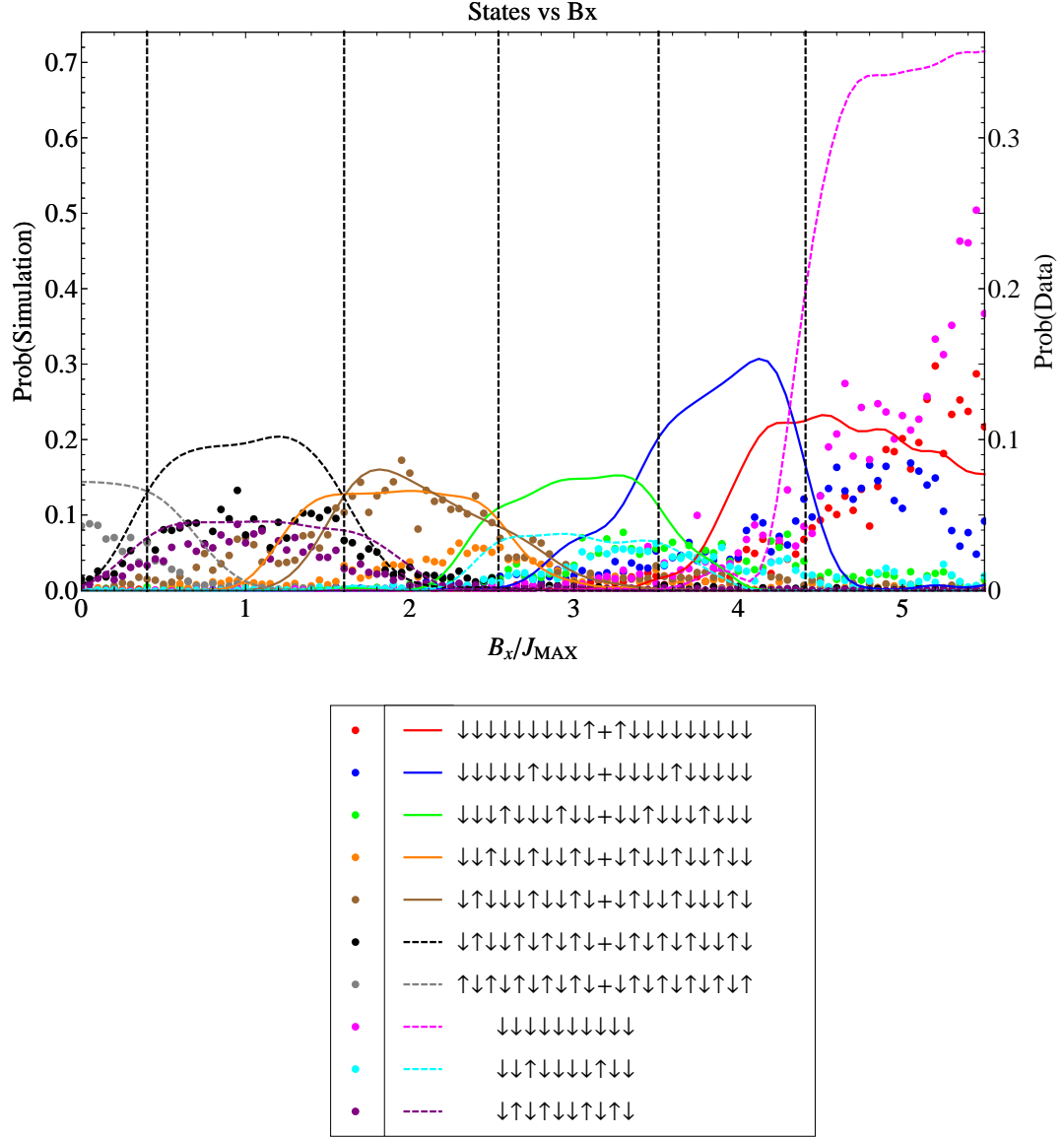


Figure 7.12: Results and simulation of dominant states. The phase transitions in the adiabatic limit are marked with dashed lines. The non-adiabaticity causes the states to bleed out of their phase in the adiabatic case. Dashed lines mark phase-transitions, found from energy crossings. Here the y-axis of the data and theory are to different scales, as the data is suppressed by noise and increased decoherence [92]

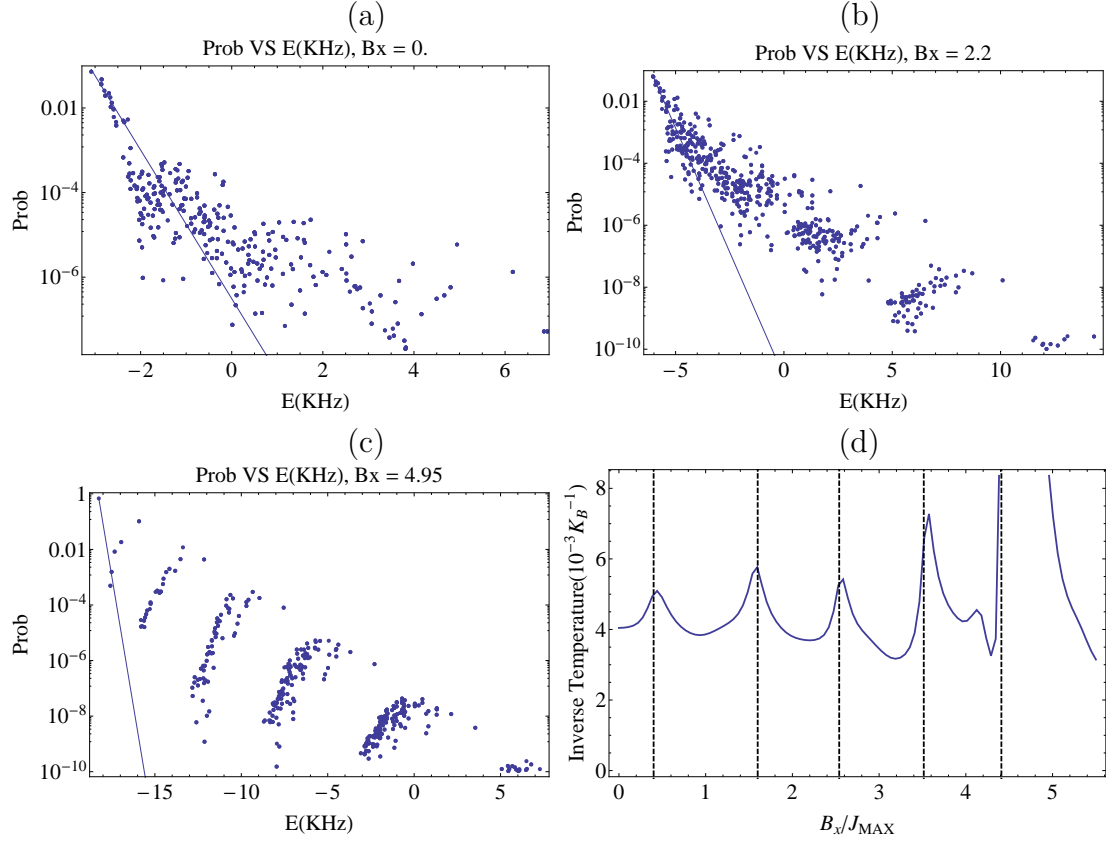


Figure 7.13: (a) Exponential fit of probability of state as a function of state energy, for $B_x = 0$. The fit slope is the inverse pseudo-temperature. (b) Exponential fit for $B_x/J_{MAX} = 2.2$. The higher energy states are beginning to separate into energy bands. (c) Exponential fit for $B_x/J_{MAX} = 4.95$. The higher energy states are now strongly separated into gaps, corresponding to the number of spins aligned with the axial field. This causes the psuedo-temperature picture to fail.(d) The temperature coefficient for all fits. This time the fit shows reliably the phase transition points, and only following the second to last transition. Phase transitions are marked with dashed lines.

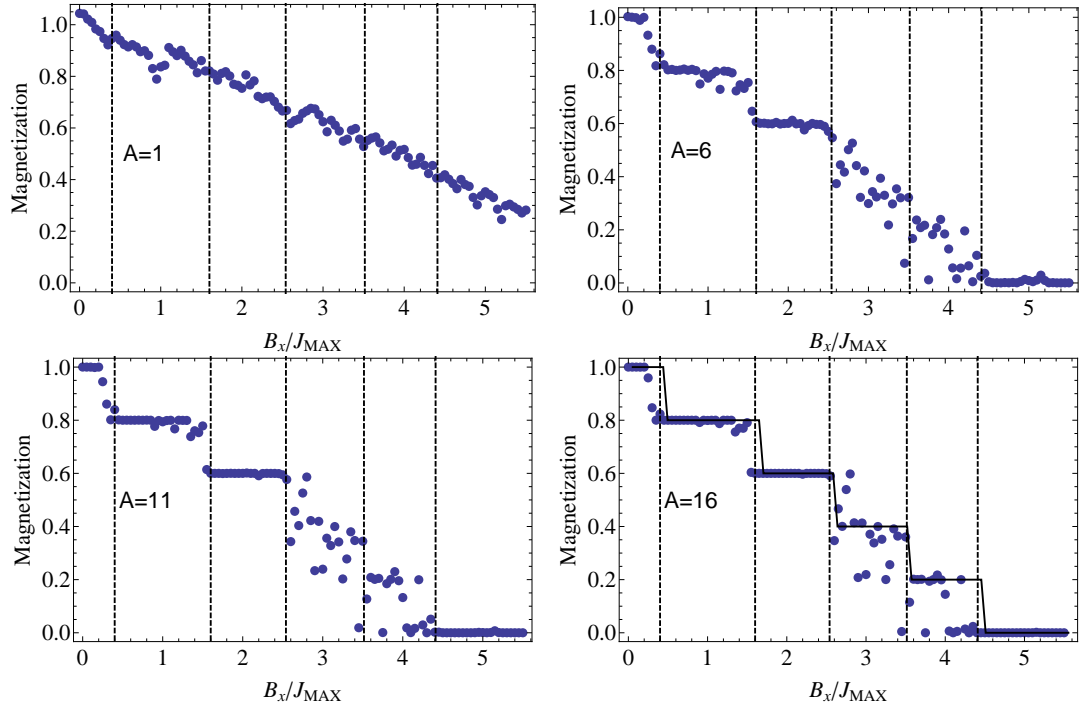


Figure 7.14: 10 ion data power filtered with power A , increasing from no filtering to $A=16$. $A=16$ plot has a solid black curve that is the adiabatic ground state solution. Dashed lines are phase transition location for adiabatic ground state.

data. However, this filter will fail to amplify the correct states close to a phase transition, as the exact ground state will not dominate for all simulation times and diabatic parameters.

As quantum simulators are scaled to higher numbers of spins and more complex Hamiltonians, extraction of the desired signal[93] will be challenged by increased decoherence [92], readout error for the total state, and diabatic effects. However, these issues may be overcome by data processing methods catered to the Hamiltonian simulated and guided by theoretical understanding of certain classes of Hamiltonians.

This work was supported by the US Army Research Office through funds from the DARPA Optical Lattice Emulator Program and the IARPA MQCO Program; the NSF Physics at the Information Frontier Program, and the NSF Physics Frontier Center at JQI.

Chapter 8

Simulating the Ising Model with Arbitrary Control of the Couplings

8.1 Introduction

In previous chapters I have discussed work where we applied global spin-dependent optical dipole forces to generate trivial forms of the spin couplings, such as a uniformly decaying ferromagnet or anti-ferromagnet. Now I will present my proposal¹ for how to tailor optical forces to generate arbitrary fully-connected networks of N spins that uniquely specify each of the $N(N - 1)/2$ pairwise interactions.

The scheme is independent of the spatial geometry of the ion crystal and is compatible with one-dimensional arrays of trapped ions used in current experiments.

We start with the arbitrary fully-connected Ising Hamiltonian on N spins,

$$H = \sum_{i < j} J_{i,j} \sigma_x^{(i)} \sigma_x^{(j)}, \quad (8.1)$$

with the same conventions we have used in previous chapters.

As in the previous work in this thesis, the spins are coherently manipulated through a pair of counter-propagating laser beams that drive stimulated Raman transitions in the far detuned limit between the spin states while also coupling off-resonantly to the collective motion of the atomic chain [95, 96]. The atoms

¹The discussion in this chapter closely follows [94]

are arranged in a linear array, as is typical in a linear radiofrequency ion trap, although this scheme can also apply to other spatial geometries [97, 98, 99]. When the difference frequency between the Raman fields is bichromatic, with two spectral components tuned symmetrically at $\omega_s \pm \mu$ with $\mu \ll \omega_s$, the effective spin-spin interaction of Eq. 8.1 emerges, mediated by the Coulomb-coupled motion of the atomic ions crystal [3, 33, 100, 32]. Just as we drove transverse modes previously, we will assume the Raman lasers have wave vector difference δk along the principal X -axis of transverse motion of the ion crystal [101], and that we are cool the ions sufficiently for us to operate in the Lamb-Dicke limit [95, 102], and the symmetric detuning μ is set sufficiently far from all motional sidebands ($|\omega_m - \mu| \gg \eta_{i,m}\Omega_i$), so that the phonon states can be adiabatically eliminated, leaving the pure spin-spin coupling above [3, 33, 57].

8.2 Control of an Arbitrary Lattice Hamiltonian

The above expression has $N + 1$ control parameters in the set of Rabi frequencies $\{\Omega_i\}$ and the global beatnote detuning μ . In order to generate an arbitrary Ising coupling matrix $J_{i,j}$ however, it is necessary to have at least $N(N - 1)/2$ independent controls [103]. Additional control parameters can be introduced by adding multiple spectral beatnote detunings to the Raman beams, one near each motional mode (see Fig. 8.1), with a unique pattern of spectral components on each ion. There are several ways to achieve this, all involving some form of individual ion addressing. For simplicity, we retain the same set of N Raman beatnote detunings μ_m on each

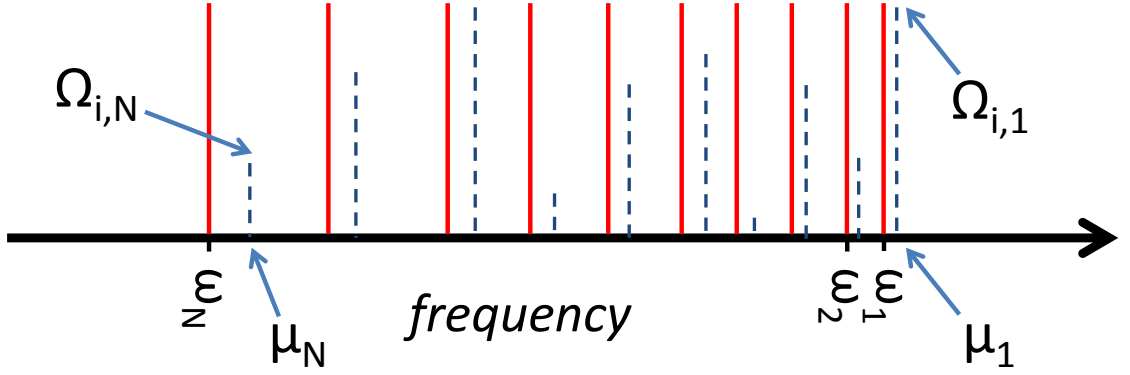


Figure 8.1: Spectrum of transverse mode frequencies ω_m for $N = 10$ ions in an anisotropic harmonic linear trap (solid lines), with the highest mode frequency ω_1 corresponding to center-of-mass motion. Raman beatnote detunings μ_m from the qubit frequency ω_s are denoted by the $N = 10$ dashed lines, with each spectral feature near a given motional sideband. The height of the dashed lines represents the intensity of each beatnote for ion i . In general each ion will be illuminated with a different set of intensities.

ion and allow the spectral amplitude pattern to vary between ions, all characterized by the $N \times N$ Rabi frequency matrix $\Omega_{i,n}$ of spectral component n at ion i . Note that the relative signs of the Rabi frequency matrix elements can be controlled by adjusting the phase of each spectral component. This individual spectral amplitude addressing provides N^2 control parameters, and the general Ising coupling matrix becomes

$$J_{i,j} = \sum_{n=1}^N \Omega_{i,n} \Omega_{j,n} \sum_{m=1}^N \frac{\eta_{i,m} \eta_{j,m} \omega_m}{\mu_n^2 - \omega_m^2} \quad (8.2)$$

$$\equiv \sum_{n=1}^N \Omega_{i,n} \Omega_{j,n} F_{i,j,n}, \quad (8.3)$$

where $F_{i,j,n}$ characterizes the response of Ising coupling $J_{i,j}$ to spectral component n . An exact derivation of the effective Hamiltonian given a spectrum of spin-dependent forces gives rise to new off resonant cross terms, which can be shown to be negligible

in the rotating wave approximation, as long as the bandwidth is fixed and the transverse center of mass mode is set to a frequency smaller than twice the transverse zig-zag mode frequency. Thus sums and differences of beatnotes do not directly encroach any sideband features in the motional spectrum of the crystal [101].

We tune each beat note frequency near a unique normal mode so that $F_{i,j,n}$ has independent contributions for each n . Given a desired Ising coupling matrix $J_{i,j}$, we use standard constrained nonlinear optimization to find the corresponding Rabi frequency matrix $\Omega_{i,n}$, while minimizing the total beam intensity. The deviation between the desired and the attained coupling was less than typical round-off errors.

However, Eq. 8.3 depends nonlinearly on the Rabi frequencies, and it is not clear that a solution exists or how the resulting total optical power scales with N .

We first describe a formal method to invert Eq. 8.3, showing the existence of a solution. For simplicity we force the control matrix to be lower triangular, or set $\Omega_{i,n} = 0$ for $i < n$, with $\Omega_{i,i} \equiv \omega_s$ (this still leaves $N(N-1)/2$ independent parameters). Isolating the $n = i$ term in the sum of Eq. 8.3, we find

$$\Omega_{j,i} = \frac{J_{i,j} - \sum_{n < i} \Omega_{i,n} \Omega_{j,n} F_{i,j,n}}{\omega_s F_{i,j,i}} \quad (i < j). \quad (8.4)$$

The left hand side defines column i of the Rabi frequency matrix, while the right hand side depends only on matrix elements in columns to the left of column i ($n < i$), resulting in a recursive definition for successive columns of $\Omega_{i,n}$. If the response functions $F_{i,j,n}$ are small however, the resulting Rabi frequencies will become unreasonably large and we find that the required total optical power in this simple

procedure generally grows exponentially with N .

We now show how to obtain a solution to inverting Eq. 8.3 that scales efficiently with N . If we neglect the effect of each beatnode μ_n on modes with $n \neq m$, $F_{i,j,n}$ is separable in i and j and we can write $J_{i,j} = \sum_n R_{i,n} R_{j,n}$, or in matrix form, $\mathbf{J} = \mathbf{R}\mathbf{R}^T$ where the matrix $R_{i,n} = \Omega_{i,n} \eta_{i,n} \sqrt{\frac{\omega_n}{\mu_n^2 - \omega_n^2}}$. This quadratic equation can be inverted by diagonalizing the symmetric matrix \mathbf{J} with some orthogonal matrix \mathbf{U} so that $\mathbf{J}_{\text{diag}} = \mathbf{U}^T \mathbf{J} \mathbf{U}$, then we simply write $\mathbf{R} = \mathbf{U}^T \sqrt{\mathbf{J}_{\text{diag}}}$. As long as the eigenvalues of \mathbf{J} are not too large, the matrix elements $R_{i,n}$ will be bounded². In practice we can impose an upper bound on the total optical power (proportional to $\sum_{i,n} |\Omega_{i,n}|$) and implement numerical optimization techniques. These produce very accurately the desired coupling matrix, much more than the approximation above, as the non-close modes for each detuning have a non-negligible effect on the solution. However, the above approximation can be used to quickly calculate an initial guess for \mathbf{R} .

8.3 Examples

We now present two example solutions for $\Omega_{i,n}$ that produce interesting interaction graph topologies. First we calculate a Rabi frequency matrix that results in a 2D square lattice of nearest-neighbor antiferromagnetic couplings with $N = 25$ ions (5×5 grid with periodic boundary conditions), shown in Figs. 8.2a-b. Next we produce a 2D Kagome lattice of antiferromagnetic interactions, a geometry that can support high levels of geometrical frustration [104], shown in Figs. 8.2d-e. In

²To avoid negative values in \mathbf{J}_{diag} we may redefine $\mathbf{J}' = \mathbf{J} + E\mathbf{1}$ with no effect on the physics

both cases we assume the center-of-mass (COM) mode to be $\omega_1/2\pi = 5$ MHz , and a fixed total optical intensity corresponding to $\sum_{i,n} |\Omega_{i,n}| = 1$ MHz . The beatnote frequencies μ_m are each tuned blue of the mode m sideband by a fraction f_s of the spacing $\omega_1 - \omega_2$ between the most closely-spaced modes (the COM and “tilt” modes, see Fig. 8.1), which itself scales as $\log N/N^2$. In these examples, the sparse nearest-neighbor nature of the interaction graphs require that most of the Ising interactions vanish, indicating a high level of coherent control over all of the Ising couplings.

8.4 Implementation

In order to generate a unique spectrum of Raman beams for each of N ions, some type of individual addressing is necessary. For simplicity, we assume one of the two Raman beams is uniform and monochromatic, and the high frequency beatnote near the qubit frequency ω_s or other global offset frequencies can be set by tuning this monochromatic beam. We focus attention on providing the requisite frequencies of the second beam, spread over a range given by the bandwidth of the transverse motional mode frequencies of the ion chain, typically in the range 1 – 5 MHz . We suggest three possible methods for providing spatial dependent frequency modulation to one of the Raman beams. The first method (Fig. 8.3 and Fig.8.4) splits a single beam with a linear chain of N individual optical modulators (e.g., acoustooptic or electrooptic devices), driven by N independent arbitrary waveform generators.

The second method splits a single monochromatic beam into a $N \times N$ square

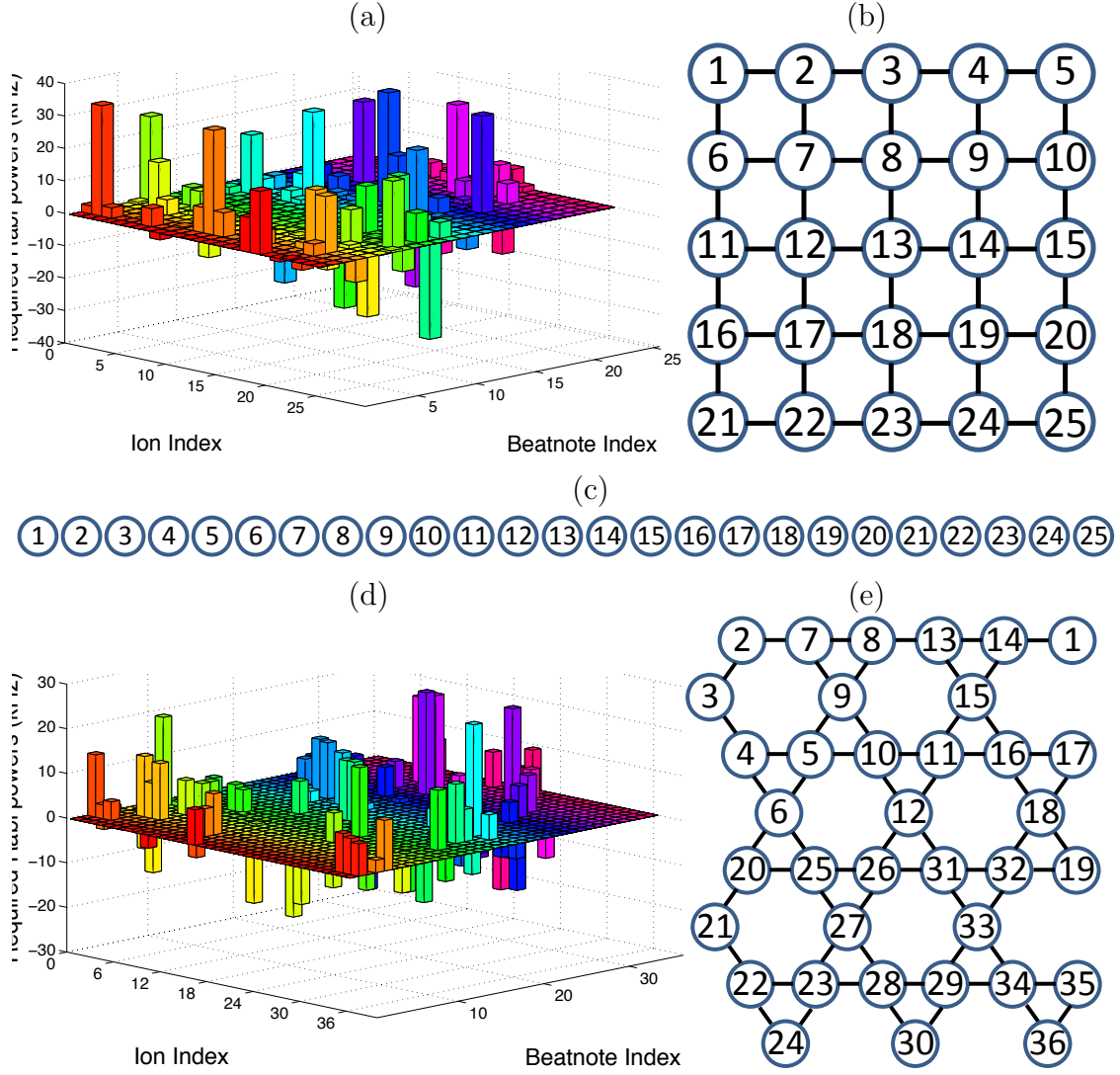


Figure 8.2: (a) Calculated Rabi frequency matrix $\Omega_{i,n}$ to generate 2D square lattice shown in (b), using the linear chain of $N = 25$ ions shown in (c). The ion index refers to the order in the linear chain. The attained $J_{i,j}$ nearest-neighbor is 27.6 Hz for $f_s = 0.1$. (d) Calculated Rabi frequency matrix $\Omega_{i,n}$ to generate 2D Kagome lattice shown in (e) using a linear chain of $N = 36$ ions. The attained $J_{i,j}$ nearest-neighbor is 93.4 Hz for $f_s = 0.03$. In both cases the total optical intensity corresponds to a Rabi frequency of 1 MHz if focused on a single ion, the nearest-neighbor couplings are antiferromagnetic and we impose periodic boundary conditions.

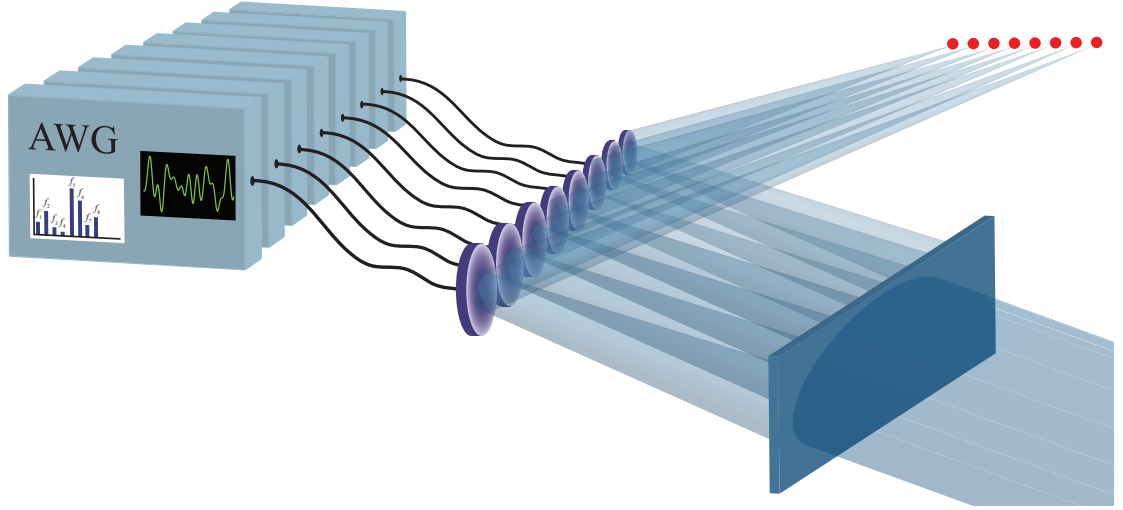


Figure 8.3: Schematic for individual spectral addressing a linear chain of N ions. A laser beam is split into a linear array of spots that each traverse N independent AOMs or EOMs, driven by N independent AWGs. Alternatively, as discussed in the text, the beam can be broken into an array of N^2 beams that strike a $N \times N$ array of micromirrors[105] each independently modulated, or a spatial light modulator.

grid and directs them onto a 2D array of N^2 micromirrors [105] that are each individually phase modulated at a single frequency (and phase) [106] and finally focused on the ion chain. The third method again splits the beam into an $N \times N$ grid of beams, this time with the vertical direction split by a single AOM, correlating beam position to frequency. This beam is then directed into a spatial light modulator that acts to mask (or phase shift) each of the $N \times N$ beams independently, and again focused onto the ion chain, as shown in figure 8.5. In these implementations, it may be desirable to work with a uniformly spaced array of ions in the linear trap, so that the modulating elements are also uniformly spaced. This can be accomplished by using a quartic or higher order linear trap [78, 107].

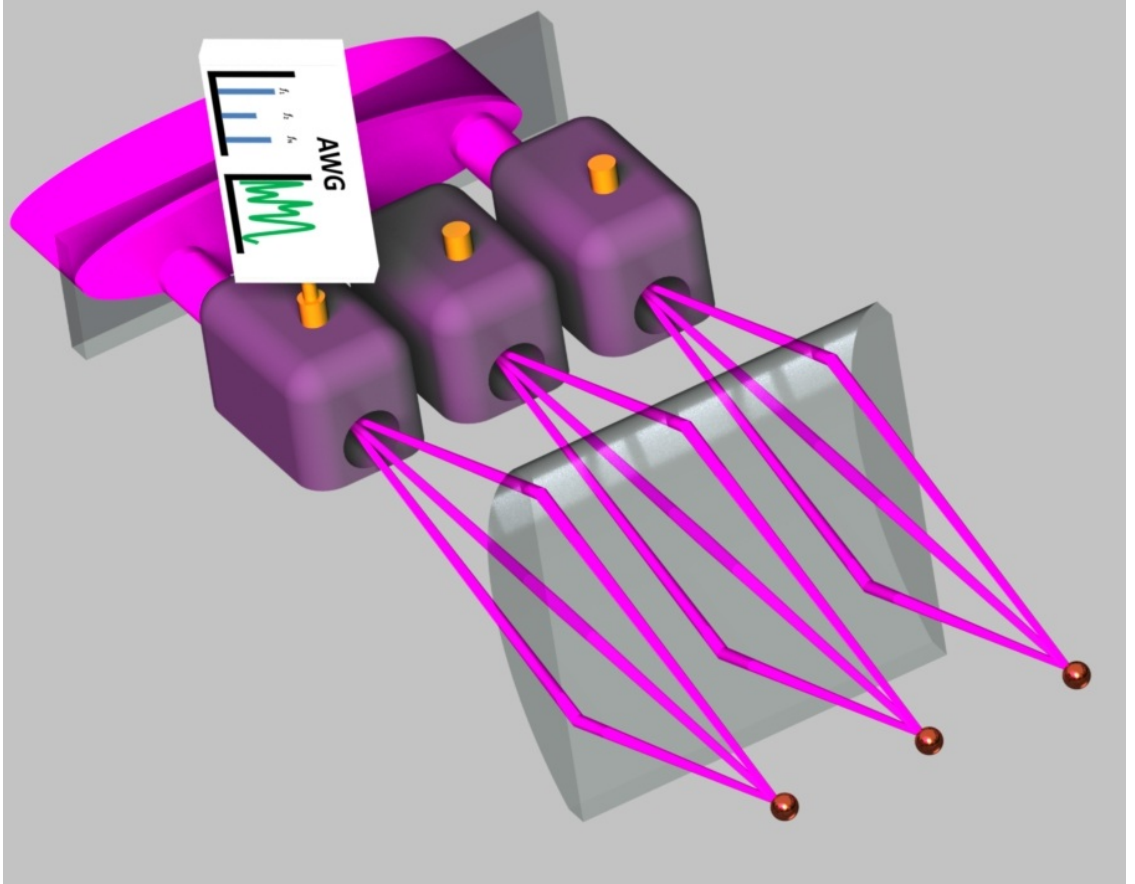


Figure 8.4: A phase mask splits a single beam into N beams, which are then modulated by N independent AOMs, each one driven with N independent amplitudes and phases (but the same frequencies, to imprint the same detunings for each mode for each ion). The modulated and deflected beams are then imaged onto the ions.

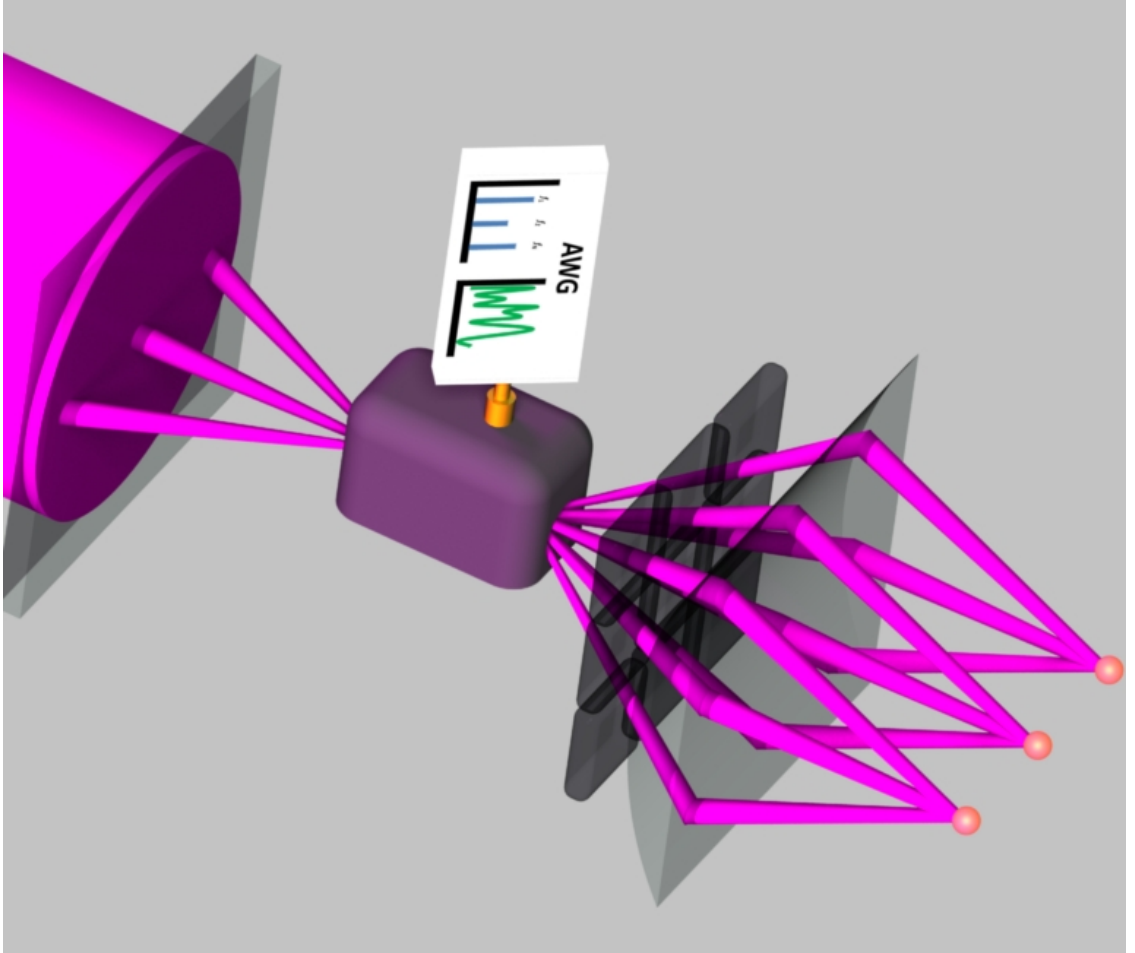


Figure 8.5: Schematic for individual spectral addressing a linear chain of N ions. The beam is again split into a $N \times N$ array, this time with a single acoustooptic modulator providing the vertical fanout, correlating spatial row with optical frequency. The grid of beams then enters a spatial light modulator, which can be a static or reconfigurable liquid crystal mask, that attenuate and/or phase shift each pixel appropriately before the columns are imaged onto the ions.

8.5 Scalability

As the number of spins N grows, the optical modulation scheme becomes more complex, with either N or N^2 elements required. However, our schemes restrict most of the resources' overhead to the design and fabrication of the micro-mirrors or phase modulator. As the ions are equally spaced, the modulator can simply be imaged onto the ion chain without changing imaging optics.

We now estimate how the Ising couplings are expected to scale with the number of spins along with errors due to experimental fluctuations, phonon creation and spontaneous emission scattering, assuming a fixed transverse mode bandwidth. The probability of phonon creation scales as $p_{ph} = \sum_{i,m} \left(\frac{\eta_{i,m} \Omega_{i,m}}{\omega_m - \mu_m} \right)^2$. The off-resonant optical dipole forces are accompanied by a finite rate of spontaneous emission scattering, given by $\Gamma = \epsilon \sum_{i,m} |\Omega_{i,m}|$, where $\epsilon \ll 1$ is the ratio of excited state linewidth to Raman detuning. The scaling of these potential errors depends upon the particular graph, so we consider two extremes. A uniform fully-connected interaction graph can be trivially generated with a single spectral component tuned close to the COM mode with a detuning $|\omega_1 - \mu|/\omega_1 \ll \log N/N^2$. For a fixed level of phonon error, the total optical intensity should be reduced as $\log N/N$, taking into account the intensity reduction per ion as the beam is expanded to accommodate the linearly expanding chain in space. In this case the uniform Ising coupling is expected to scale as $N|J_{i,j}| \propto \log N/N^2$, and the spontaneous emission rate per spin actually decreases with N . For a sparse interaction graph, such as a 1D (nearest-neighbor) Ising model, all modes are involved, and this time for a fixed phonon error the total

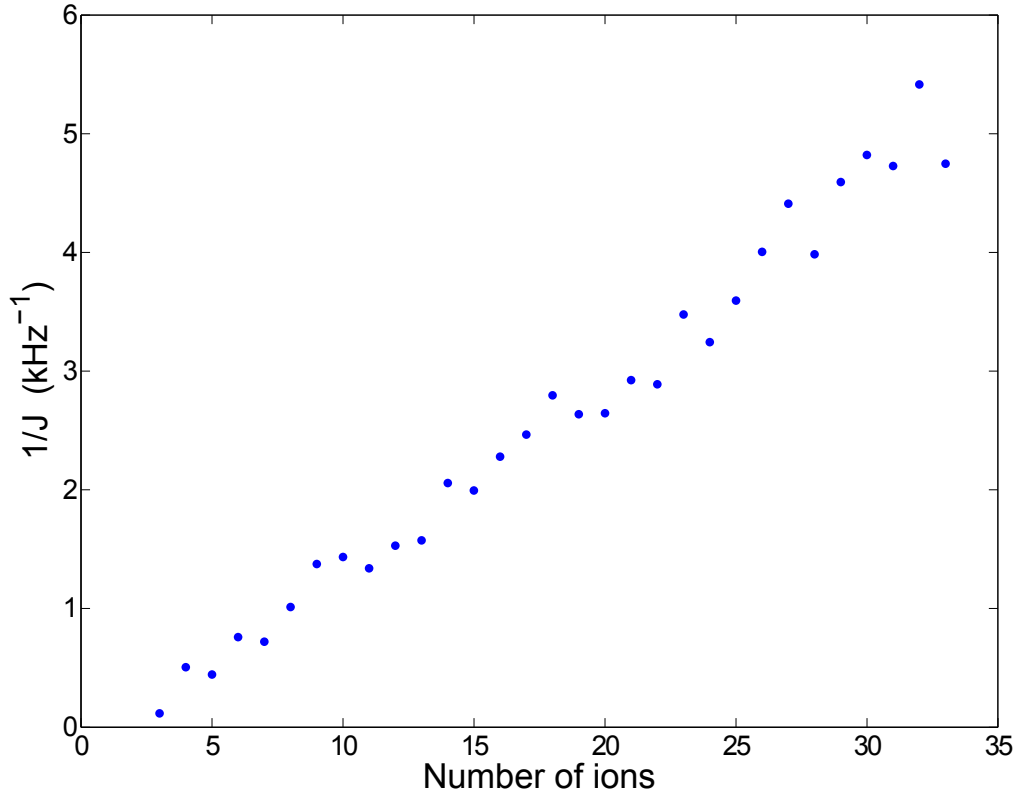


Figure 8.6: Scaling of the nearest-neighbor coupling for the case of the production of a 1D Ising chain for $N = 3$ to $N = 33$ ions. The total optical intensity is fixed with $\sum_{i,n} |\Omega_{i,n}| = 1$ MHz, and each spectral component is detuned from its motional sideband by a fraction $f_s = 0.03$ of smallest mode splitting, with a center-of-mass (COM) frequency $\omega_1/2\pi = 5$ MHz. We find that the resulting Ising coupling scales roughly as $1/N$.

optical intensity can remain fixed, since the typical mode splitting falls only as $1/N$, while spontaneous emission per ion is fixed. The calculation in Fig. 8.6 shows that the resulting nearest-neighbor interaction scales as $J_{i,i+1} \propto 1/N$. In either case of fully-connected or local Ising model, we thus expect to be able to support significant Ising interaction strengths with up to a few hundred spins.

For a general Ising graph, from Eq. 8.3 we find that each pairwise interaction $J_{i,j}$ depends upon a balance of N terms, and errors will accumulate with N from

fluctuations of relative optical intensities of the various spectral components of the beam (which should be stable if the spectral components are generated with high quality RF sources and modulators as shown in Fig. 8.3) or their detunings from the motional sidebands. The most important source will likely be fluctuations in the motional trap frequencies, where we expect the fractional error in the Ising coupling to grow as $\sqrt{N}(\delta\omega_m/\omega_m)$, so that a typical fractional fluctuation in the motional trapping frequencies of $\sim 10^{-3}$ might be expected to cause Ising coupling errors at a level of about 1% for $N \sim 100$ ions.

The final limitation on simulation time is effective spin coherence. Assuming the qubits experience Markovian noise, the coherence time of the ensemble will go as $1/N$, so that a qubit coherence time of ~ 10 s (as is typical for hyperfine qubits) will allow for a simulation time on order ~ 100 ms for ~ 100 ions.

8.6 Conclusion

The scheme presented here can also be applied to more general Heisenberg spin models involving other noncommuting spin-spin interactions, such as the XY model or the 2D hexagonal Kitaev model relevant to topological quantum degrees of freedom [108]. Here, additional Raman beams that couple to the other axes of motion can be exploited. This scheme may also be used to study phase transitions in a quantum transverse magnetic field [109]. Alternatively, a single direction of motion can be used as discussed above, with a stroboscopic alternation between Raman laser beams with different beat note phases as the various Ising interactions

in the Hamiltonian are applied sequentially. Here, we employ the Trotter expansion of the evolution operator [5, 110] and switch the various Ising terms rapidly enough so that higher order terms in the expansion can safely be neglected. Although this discussion concentrated on a linear array of ions in space, these ideas apply in general to any stable ion crystal where the motional sidebands are resolved and prepared in the Lamb-Dicke limit, and should be useful for higher-dimensional trap geometries such as trap arrays [98, 99] or Penning traps [97, 111].

Appendix A

Linear Trap External Pi Filter

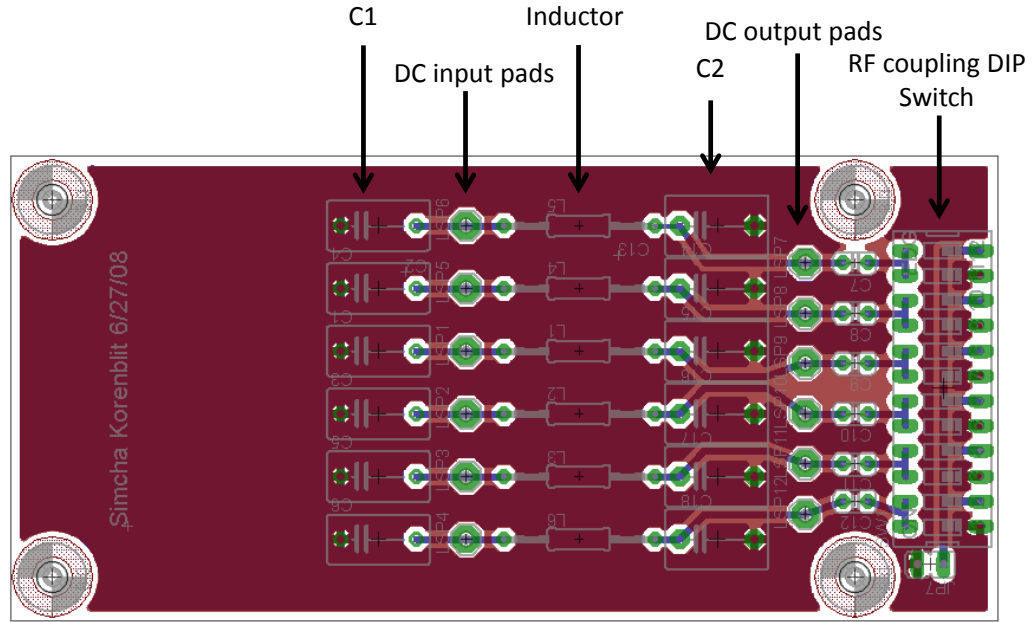


Figure A.1: PCB mask, pads and traces for linear trap pi-filter. C1 and C2 are high voltage ceramic capacitors of $0.1\mu F$ each; the inductors are $100\mu H$ each.

In [A.1](#) the Printed Circuit Board (PCB) mask is presented. There are several things to take note of in this design:

1. This filter is based upon a Pi filter design, where the RF rejecting component is an inductor (an alternate design uses a resistor instead). However numerical simulations indicated that the addition of a resistor in series with the inductor

gave a sharper frequency response. Therefore a resistor was added to the actual circuit, however the mask in [A.1](#) was the one ordered and therefore the resistor is not indicated in the silkscreen.

2. The circuit includes a DIP switch near the output end. This switch selects between coupling the RF pickup on a DC channel to an output, through a capacitor to ground, or to an output. This is useful for measuring the RF pickup on the DC electrodes through capacitive coupling to the RF electrode.

Appendix B

Optical Diagram Legend

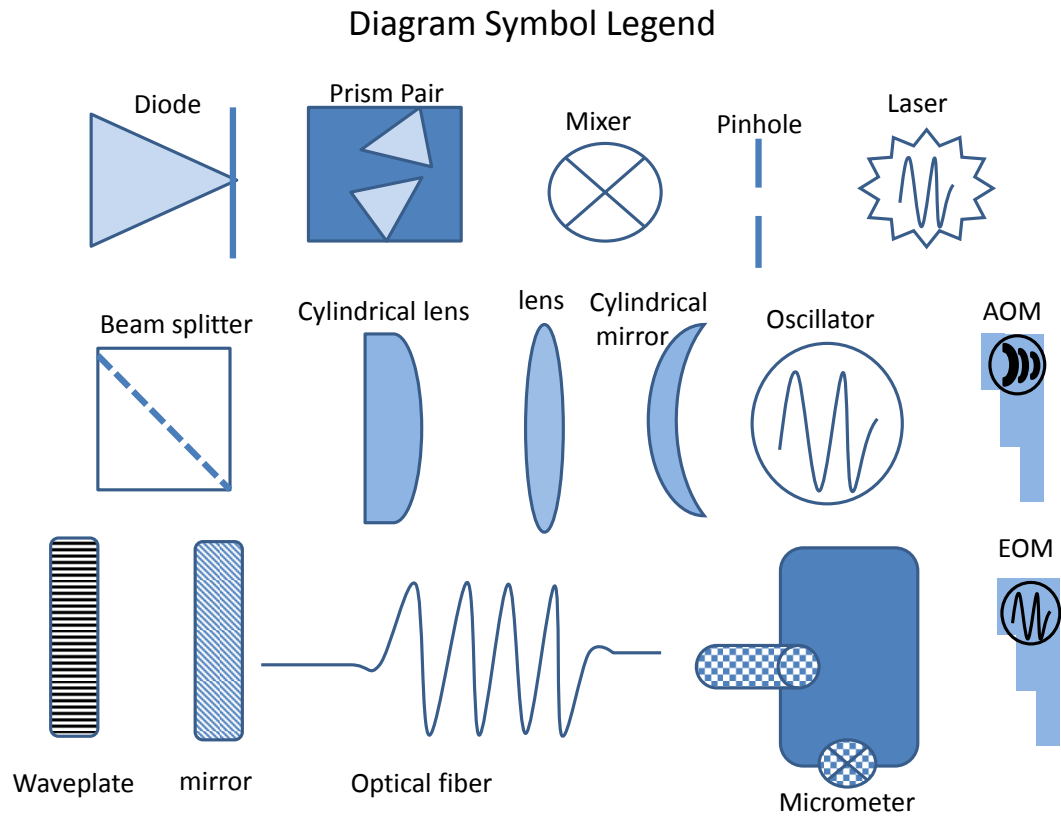


Figure B.1: This is the legend of all symbols used in optical diagrams in this work.

Appendix C

AWG Function Library

```
1 // AWG_dll.cpp : Defines the exported functions for the DLL application
2
3
4
5
6
7
8
9 const double num=2*3.14159265358979323846/1000; /*for speed, frequenecy
    in MHz */
10
11 struct SegmentStruct //need to build an array of these
12 {
13     DWORD SegmentNum; // Current Segment Number
14     unsigned short *SegmentPtr; // Pointer to current user segment
15     DWORD NumPoints; // Number of points in segment
16     DWORD NumLoops; // Number of times to repeat segment (applies to next
        segment)
17     DWORD BeginPadVal; // Pad value for beginning of triggered segment
18     DWORD EndingPadVal; // Pad value for ending of triggered segment
19     DWORD TrigEn; // If > 0 then wait for trigger before going to next
```

```

    segment.

20 DWORD NextSegNum; // Next segment to jump to after completion

21 // of current segment activities

22 };

23

24 struct wave

25 {

26     double f;

27     double phase;

28     double amp;

29 };

30

31 struct linear_param

32 {

33

34     double f1 , p1 , f2 , p2 , f3 , p3;

35     float a1 , a2 , a3;

36     double slope;

37 };

38

39 struct sb_param

40 {

41     unsigned long modes;

42     double *f;

43     double *duration;

44     unsigned long Optime;

45     unsigned short pulses;

```

```

46 };

47

48 int make64x(unsigned long size)
49 {
50     div_t result=div(size,64);
51     if (result.rem>0)
52         return(64-result.rem);
53     else
54         return(0);
55 }

56

57 __declspec (dllexport) long side_band_cooling_sequential(unsigned
    short *a, unsigned long modes, double *f,
58
    unsigned long *duration, unsigned long OPtime,
    unsigned short pulses)
59 {
60     unsigned long i,j,m,t=0;
61
62     for (i=0;i<pulses;i++)
63         for(m=0;m<modes; m++)
64             {
65                 for (j=0; j<round(sqrt((double)((double)pulses/(double)(pulses-i)
    ))*(double)duration[m])); j++) /*time is in NANOSECONDS */
66                     {
67                         a[t] = (unsigned short)round(2048-2048*sin(num*f[m]*t));
68                         t++;
69                     }

```

```

70     for (j=0; j<OPtime; j++)
71     {
72         a[t]=2048;
73         t++;
74     }
75 }
76 //Dirty hack to delay wave to match Raman 1
77
78 for (i=0;i<150;i++)
79 {
80     a[t]=(unsigned short)(2048);
81     t++;
82 }
83
84 unsigned long pad=make64x(t);
85 for (j=0; j<pad; j++)
86 {
87     a[t]=2048;
88     t++;
89 }
90 return (t);
91 }
92
93 __declspec (dllexport) unsigned long  calculate_sbc_array_size(unsigned
        long modes, double *f,unsigned long *duration, unsigned long
        OPtime, unsigned short pulses)
94 {

```

```

95  unsigned long i , j , m , t = 0;
96
97      for ( i = 0 ; i < pulses ; i ++ )
98  for ( m = 0 ; m < modes ; m ++ )
99  {
100      for ( j = 0 ; j < round ( sqrt ( ( double ) ( ( double ) pulses / ( double ) ( pulses - i )
          ) ) * ( double ) duration [ m ] ) ; j ++ ) /* time is in NANoseconds */
101          t ++ ;
102      t += OPTime ;
103  }
104      t += 150 ;
105      t += make64x ( t ) ;
106      return ( t ) ;
107 }
108
109 __declspec ( dllexport ) long flat ( unsigned short * a , unsigned long & t ,
          unsigned long duration )
110 {
111     for ( unsigned long i = 0 ; i < duration ; i ++ )
112     {
113         a [ t ] = 2048 ;
114         t ++ ;
115     }
116     return ( t ) ;
117 }
118
119 __declspec ( dllexport ) unsigned long exp_simulation ( unsigned short * a ,

```



```

        double *f, double *p, double *amp,
120                                     unsigned long *duration)
121 //amp has 6 values
122 //| - | - | - | - | - | - | - | - |
123 // 0 Ci:1, Cf:2,3,4 5
124 //duration has 5 :| - | - | - | - | - | - | - | - |
125 //          0 1      2      3 4
126 //CAREFUL! Labview calls a function to find the length of this waveform
        . Update this function in the control program if
127 //you change this function
128 {
129     unsigned long i;
130     int pad;
131     double slope=-abs(amp[2]);
132
133     unsigned long t=0;
134
135     for (i=0;i<duration[0];i++)
136     {
137         a[t]=(unsigned short)(2048.5+amp[0]*sin(num*f[0]*t+p[0]));
138         t++;
139     }
140     for (i=0;i<duration[1];i++)
141     {
142         a[t]=2048;
143         t++;
144     }

```

```

145   for (i=0;i<duration[2];i++)
146   {
147       a[t]=(unsigned short)(2048.5+amp[7]*sin(num*f[4]*t)//comp2
148           amp[6]*(1-exp(i/slope))*sin(num*f[3]*t)//comp1 for carrier
149           exp(i/slope)*amp[1]*sin(num*f[0]*t+p[1])//carrier
150           amp[3]*sin(num*f[1]*t)//rsb
151           amp[4]*sin(num*f[2]*t+p[2]));//bsb
152       t++;
153   }
154   for (i=0;i<duration[3];i++)
155   {
156       a[t]=2048;
157       t++;
158   }
159   for (i=0;i<duration[4];i++)
160   {
161       a[t]=(unsigned short)(2048.5+amp[5]*sin(num*f[0]*t+p[3]));
162       t++;
163   }
164
165   for (i=0;i<150;i++)
166   {
167       a[t]=(unsigned short)(2048);
168       t++;
169   }
170
171   pad=make64x(t);

```

```

172  for (i=0;i<(unsigned long)pad;i++)
173  {
174      a[t]=2048;
175      t++;
176  }
177
178  return(t);
179 }
180
181 __declspec (dllexport) unsigned short * find_address(unsigned short *a
        )
182 {
183  return(a);
184 }
185
186 __declspec (dllexport) unsigned long BuildArray(SegmentHdl *S, unsigned
        short *a)
187 {
188  unsigned long i,j,t=0;
189  /*
190   struct SegmentStruct //need to build an array of these
191  {
192  DWORD SegmentNum; // Current Segment Number
193  unsigned short *SegmentPtr; // Pointer to current user segment
194  DWORD NumPoints; // Number of points in segment
195  DWORD NumLoops; // Number of times to repeat segment (applies to next
        segment)

```

```

196 DWORD BeginPadVal; // Pad value for beginning of triggered segment
197 DWORD EndingPadVal; // Pad value for ending of triggered segment
198 DWORD TrigEn; // If > 0 then wait for trigger before going to next
    segment.
199 DWORD NextSegNum; // Next segment to jump to after completion
200 // of current segment activities
201 };*/
202
203
204     for (i=0;i<(unsigned long)(**S)->NumOfSegments;i++)
205     {
206         for (j=0;j<(unsigned long) (*(**S)->segment[i].SegmentPtr)->
            WaveSize;j++)
207         {
208             a[t]=(*(**S)->segment[i].SegmentPtr)->wave[j];
209             t++;
210         }
211     }
212     return((unsigned long)(**S)->NumOfSegments);
213 }
214
215 __declspec(dllexport) unsigned long BuildDA11000Array(SegmentHdl *S,
    SegmentStruct *a)
216 {
217     unsigned long i;
218     /*
219     struct SegmentStruct //need to build an array of these

```

```

220 {
221 DWORD SegmentNum; // Current Segment Number
222 unsigned short *SegmentPtr; // Pointer to current user segment
223 DWORD NumPoints; // Number of points in segment
224 DWORD NumLoops; // Number of times to repeat segment (applies to next
    segment)
225 DWORD BeginPadVal; // Pad value for beginning of triggered segment
226 DWORD EndingPadVal; // Pad value for ending of triggered segment
227 DWORD TrigEn; // If > 0 then wait for trigger before going to next
    segment.
228 DWORD NextSegNum; // Next segment to jump to after completion
229 // of current segment activities
230 };*/
231   for (i=0;i<(unsigned long)(**S)->NumOfSegments;i++)
232   {
233     a[i].BeginPadVal=(**S)->segment[i].BeginPadVal;
234     a[i].EndingPadVal=(**S)->segment[i].EndingPadVal;
235     a[i].NextSegNum=(**S)->segment[i].NextSegNum;
236     a[i].NumLoops=(**S)->segment[i].NumLoops;
237     a[i].SegmentNum=(**S)->segment[i].SegmentNum;
238     a[i].TrigEn=(**S)->segment[i].TrigEn;
239     a[i].NumPoints=(**S)->segment[i].SegmentPtr->WaveSize;
240     a[i].SegmentPtr=(**S)->segment[i].SegmentPtr->wave;
241   }
242   return((unsigned long)(**S)->NumOfSegments);
243 }
244

```

```

245 __declspec(dllexport) bool LoadSegmentHdl(SegmentHdl *S)
246 {
247     bool error=false;
248     SegmentStruct *a= new SegmentStruct[(**S)->NumOfSegments]; // don't
        forget delete [(**S)->NumOfSegments]
249     BuildDA11000Array(S,a);
250     // INITIALIZE BOARD
251     da11000_SetTriggerMode(1,0,0);
252     da11000_CreateSegments(1,1,(**S)->NumOfSegments,a);
253
254     delete [(**S)->NumOfSegments] a;
255     return(error);
256 }

```

Appendix D

Mathematica ROI and Discriminator Selection Script

The following script is called after taking 1000 shots of the ions pumped dark and then 1000 shots of the ions rotated to bright.

It is called from the Labview control program automatically after the shots have been taken, run as a command line script with the following parameters -

“dark.csv” - “bright.csv” - Nions - Nimages - cutoff (0 - 1)

The script (“ROI auto selection.m”) is created and run from the directory of the data files. example :

```
math - script “ROI auto selection.m” “dark Shots.csv” “bright Shots.csv” 4 1000  
0.5
```

```
DarkDataT = Transpose[Import[$CommandLine[[4]]];
```

```
dataT = Transpose[Import[$CommandLine[[5]]];
```

```
Nions = ToExpression[$CommandLine[[6]];
```

```
MaxDataT = Max[dataT];
```

```
Nimages = ToExpression[$CommandLine[[7]];
```

```
width = Dimensions[dataT][[2]]/Nimages;
```

```
height = Dimensions[dataT][[1]];
```

This section sums all the frames and then normalizes the image. It also calculates the average value of both the dark and bright pixels.

```
NormImageDark = Sum[DarkDataT[[All, widthx + 1;;(x + 1)width]], {x, 0, Nimages - 1}];
```

```
NormImage = Sum[dataT[[All, widthx + 1;;(x + 1)width]], {x, 0, Nimages - 1}];
```

```

NormImageSubtracted = NormImage - NormImageDark;
NormImageSubtracted /= Max[NormImageSubtracted];
IonImage = NormImageSubtracted/.x_/;x < ToExpression[$CommandLine[[8]]]->0;

```

Here we find the vertical Region for ion1, VertStart and VertEnd that define the vertical edges. We find VertStart by starting at 0, and then scan the horizontal pixels, looking for brightness > threshold. If no non-zero pixels are found, VertStart is shifted by 1 and we scan again ...VertEnd starts from the height, and we scan along the horizontals, if no bright pixel is found we shift to height - 1 and scan again and so on ...

```

VertStart = 0;
VertEnd = height;
For[n = 1, n < height + 1, n++,
  For[i = 1, i < width + 1, i++,
    If[IonImage[[n, i]] > 0, VertStart = n; i = width + 1; n = height + 1]]]
For[n = height, n > VertStart, n--,
  For[i = 1, i < width + 1, i++,
    If[IonImage[[n, i]] > 0, VertEnd = n; i = width + 1; n = 1]]]

If[VertEnd > height, VertEnd = height];
VertStart = If[VertStart > 0, VertStart, 1];

```

```

Export["uncutoff image " <> DateString[{ "Year", "Month", "Day" }] <> ".jpg",
Image[IonImage[[All, All]]]]

```

```

HEdge = Join[{ {1, 0} }, Table[{1, 1}, {i, 1, Nions}]]
center = VertStart + Floor[(VertEnd - VertStart)/2];

```



```

For[i = 1, i <= Nions, i++,
  For[j = HEdge[[i, 2]] + 1, j < width, j++,
    If[Count[Table[N[IonImage[[v, j]]], {v, VertStart, VertEnd, 1}], 0.]
    < (3(VertEnd - VertStart))/4, HEdge[[i + 1, 1]] = j;
    For[k = j, k < width, k++,
      If[Count[Table[N[IonImage[[v, k]]], {v, VertStart, VertEnd, 1}], 0.] >
      (3(VertEnd - VertStart))/4, HEdge[[i + 1, 2]] = k - 1; k = width; j = width
    ];]]
HEdge = Delete[HEdge, 1]

dataFrames = Table[dataT[[VertStart;;VertEnd, widthx + 1;;(x + 1)width]],
  {x, 0, Nimages - 1, 1}];
darkFrames = Table[DarkDataT[[VertStart;;VertEnd, widthx + 1;;(x + 1)width]],
  {x, 0, Nimages - 1, 1}];
HistogramDataBright = Table[Total[Flatten[dataFrames[[j, All, HEdge[[i, 1]];;
HEdge[[i, 2]]]]], {i, Nions}, {j, 1, Nimages}];
HistogramDataDark = Table[Total[Flatten[darkFrames[[j, All, HEdge[[i, 1]];;
HEdge[[i, 2]]]]], {i, Nions}, {j, 1, Nimages}];
Export["Histograms " <> DateString[{ "Year", "Month", "Day" }] <> ".pdf",
Table[Histogram[{HistogramDataDark[[i]], HistogramDataBright[[i]]},
{500}, ImageSize->300], {i, Nions}]]//TableForm]

Export["Histogram tables dark" <> DateString[{ "Year", "Month", "Day" }] <> ".xls",
Table[Table[{#[[1, i]], #[[2, i]]}, {i, Length[#[[2]]]}]&
[HistogramList[HistogramDataDark[[j]]], {j, Nions}]]
Export["Histogram tables bright" <> DateString[{ "Year", "Month", "Day" }]
<> ".xls", Table[Table[{#[[1, i]],

```

```
#[[2, i]], {i, Length#[[2]]}]&[HistogramList[HistogramDataBright[[j]]], {j, Nions}]]
```

```
ErrorThreshold = Table[{0, 0}, {i, Nions}];
```

```
Steps = 50;
```

```
For[i = 1, i < Nions + 1, i++,
```

```
DL = HistogramList[HistogramDataDark[[i]], {Steps}];
```

```
BL = HistogramList[HistogramDataBright[[i]], {Steps}];
```

```
    We match the histogram dimensions
```

```
DiffL = Min[BL[[1]]] - Min[DL[[1]]];
```

```
DiffU = Max[BL[[1]]] - Max[DL[[1]]];
```

```
If[DiffL >= 0,
```

```
{BLNew1 = Join[Table[Min[BL[[1]]] - Abs[DiffL] + (n - 1) * Steps,
```

```
{n, 1, Floor[Abs[DiffL]/Steps]}], BL[[1]]];
```

```
BLNew2 = Join[Table[0, {n, 1, Floor[DiffL/Steps]}], BL[[2]]];
```

```
BLNewInt = Join[{BLNew1}, {BLNew2}];
```

```
DLNewInt = DL; },
```

```
{DLNew1 = Join[Table[Min[DL[[1]]] - Abs[DiffL] + (n - 1) * Steps,
```

```
{n, 1, Floor[Abs[DiffL]/Steps]}], DL[[1]]];
```

```
DLNew2 = Join[Table[0, {n, 1, Floor[Abs[DiffL]/Steps]}], DL[[2]]];
```

```
DLNewInt = Join[{DLNew1}, {DLNew2}];
```

```
BLNewInt = BL; }];
```

```
If[DiffU >= 0,
```

```
{DLNew3 = Join[DLNewInt[[1]], Table[Max[DLNewInt[[1]]] + n * Steps,
```

```
{n, 1, Floor[DiffU/Steps]}]]];
```

```
DLNew4 = Join[DLNewInt[[2]], Table[0, {n, 1, Floor[DiffU/Steps]}]]];
```

```
DLNew = Join[{DLNew3}, {DLNew4}];
```

```
BLNew = BLNewInt; },
```

```

{BLNew3 = Join[BLNewInt[[1]], Table[Max[BLNewInt[[1]]] + n * Steps,
{n, 1, Floor[Abs[DiffU]/Steps]}]];
BLNew4 = Join[BLNewInt[[2]], Table[0, {n, 1, Floor[Abs[DiffU]/Steps]}]];
BLNew = Join[{BLNew3}, {BLNew4}];
DLNew = DLNewInt};];

```

```

TDL = Table[Total[DLNew[[2, 1;;j]]], {j, 1, Dimensions[DLNew[[2]]][[1]]};
TBL = Table[Nimages - Total[BLNew[[2, 1;;j]]],
{j, 1, Dimensions[BLNew[[2]]][[1]]};
Diff = TDL - TBL;

```

Now we find the unbiased thresholds and export our findings for the control program to use

```

x = Position[Abs[Diff], Min[Abs[Diff]]][[1, 1]];
Error = N[(Sum[BLNew[[2, n]], {n, 1, x}]/Nimages) * 100];
ErrorThreshold[[i]] = {VertStart - 1, VertEnd, HEdge[[i, 1]] - 1,
HEdge[[i, 2]], Error, BLNew[[1, x]]};]
Export["ROI Error and Thresholds.csv", ErrorThreshold]

```

```

ErrorThreshold = Prepend[ErrorThreshold, {"Lower Vertical Edge", "Upper Vertical Edge",
"Left Edge", "Right Edge", "State detection error", "Threshold"}]
Export["ROI Error and Thresholds " <> DateString[{ "Year", "Month", "Day" }]
<> ".xls", ErrorThreshold]

```

Bibliography

- [1] S. Olmschenk, K. C. Younge, D. L. Moehring, D. N. Matsukevich, P. Maunz, and C. Monroe. Manipulation and detection of a trapped yb^{+} hyperfine qubit. *Phys. Rev. A*, 76(5):052314, 2007.
- [2] M. J. Madsen, W.K. Hensinger, D. Stick, J.A. Rabchuk, and C. Monroe. Planar ion trap geometry for microfabrication. *Appl. Phys. B*, 78:639, 2004.
- [3] A. Sørensen and K. Mølmer. Quantum computation with ions in thermal motion. *Phys. Rev. Lett.*, 82(9):1971–1974, 1999.
- [4] Richard Feynman. Simulating physics with computers. *Intl J Theo Phys*, 21(6/7):467, 1982.
- [5] S. Lloyd. Universal quantum simulators. *Science*, 273(5278):1073–1078, 1996.
- [6] S. Sachdev. *Quantum Phase Transitions*. Cambridge University Press, 2011.
- [7] K. Binder and A. P. Young. Spin glasses: Experimental facts, theoretical concepts, and open questions. *Rev. Mod. Phys.*, 58:801–976, 1986.
- [8] L. Balents. Spin liquids in frustrated magnets. *Nature*, 464:199–208, 2010.
- [9] B A Cipra. The ising model is np-complete. *SIAM News*, 33(6):1–3, 2000.
- [10] Satish Damaraju, Varghese George, Sanjeev Jahagirdar, Tanveer Khondker, Robert Milstrey, Sanjib Sarkar, Scott Siers, Israel Stolerio, and Arun Subbiah. A 22nm ia multi-cpu and gpu system-on-chip. In *Solid-State Circuits Conference Digest of Technical Papers (ISSCC), 2012 IEEE International*, pages 56–57. IEEE, 2012.
- [11] M. A. Nielsen and I. L. Chuang. *Quantum Computation and Quantum Information*. Cambridge University Press, Cambridge, UK, 2000.
- [12] R. Moessner and A. P. Ramirez. Geometrical frustration. *Phys. Today*, 59:24, Feb 2006.
- [13] Leon Balents. Spin liquids in frustrated magnets. *Nature*, 464:199, 2010.
- [14] Tru Moriya and Kazuo Ueda. Antiferromagnetic spin fluctuation and superconductivity. *Reports on Progress in Physics*, 66(8):1299, 2003.
- [15] S. Sachdev. Order and quantum phase transitions in the cuprate superconductors. *Rev. Mod. Phys.*, 75:913–932, 2003.
- [16] Jacob D. Biamonte and Peter J. Love. Realizable hamiltonians for universal adiabatic quantum computers. *Phys. Rev. A*, 78(1):012352, 2008.

- [17] D. Aharonov, W. van Dam, J. Kempe, Z. Landau, S. Lloyd, and O. Regev. Adiabatic quantum computation is equivalent to standard quantum computation. *SIAM Review*, 50(4):755–787, 2008.
- [18] John M Martinis, M Ansmann, and J Aumentado. Energy decay in superconducting josephson-junction qubits from nonequilibrium quasiparticle excitations. *Physical review letters*, 103(9):097002, 2009.
- [19] J Majer, JM Chow, JM Gambetta, Jens Koch, BR Johnson, JA Schreier, L Frunzio, DI Schuster, AA Houck, A Wallraff, et al. Coupling superconducting qubits via a cavity bus. *Nature*, 449(7161):443–447, 2007.
- [20] Edward Farhi, Jeffrey Goldstone, Sam Gutmann, and Michael Sipser. Quantum computation by adiabatic evolution. *arXiv preprint quant-ph/0001106*, 2000.
- [21] Anders W. Sandvik. Ground states of a frustrated quantum spin chain with long-range interactions. *Phys. Rev. Lett.*, 104:137204, Mar 2010.
- [22] E. Farhi and S. Gutmann. Analog analogue of a digital quantum computation. *Physical Review A*, 57(4):2403–2406, 1998.
- [23] DM Tong, K Singh, LC Kwek, and CH Oh. Sufficiency criterion for the validity of the adiabatic approximation. *Physical review letters*, 98(15):150402, 2007.
- [24] D F. James and J Jerke. Effective hamiltonian theory and its applications in quantum information. *Canadian Journal of Physics*, 85(6):625–632, 2007.
- [25] WC Martin and WL Wiese. Atomic, molecular and optical physics handbook. *American Institute of Physics: Woodbury, New York*, 1996.
- [26] S A King, R M Godun, S A Webster, H S Margolis, L A M Johnson, K Szymaniec, P E G Baird, and P Gill. Absolute frequency measurement of the $2s\ 1/2 - 2f\ 7/2$ electric octupole transition in a single ion of 171 yb^+ with 10–15 fractional uncertainty. *New Journal of Physics*, 14(1):013045, 2012.
- [27] Kazuhiko Sugiyama and Jun Yoda. Production of yb^+ by chemical reaction of yb^+ in excited states with h_2 gas. *Phys. Rev. A*, 55:R10–R13, Jan 1997.
- [28] D. J. Wineland, R. E. Drullinger, and F. L. Walls. Radiation-pressure cooling of bound resonant absorbers. *Phys. Rev. Lett.*, 40:1639–1642, Jun 1978.
- [29] Q. A. Turchette, Kielpinski, B. E. King, D. Leibfried, D. M. Meekhof, C. J. Myatt, M. A. Rowe, C. A. Sackett, C. S. Wood, W. M. Itano, C. Monroe, and D. J. Wineland. Heating of trapped ions from the quantum ground state. *Phys. Rev. A*, 61:063418, May 2000.
- [30] D. J. Berkeland and M. G. Boshier. Destabilization of dark states and optical spectroscopy in zeeman-degenerate atomic systems. *Phys. Rev. A*, 65:033413, Feb 2002.

- [31] M Acton, K.-A. Brickman, P. C. Haljan, P. J. Lee, L. Deslauriers, and C. Monroe. Near-perfect simultaneous measurement of a qubit register. *Quantum Info. Comput.*, 6(6):465–482, September 2006.
- [32] P J Lee, K-A Brickman, L Deslauriers, P C Haljan, L-M Duan, and C Monroe. Phase control of trapped ion quantum gates. *Journal of Optics B: Quantum and Semiclassical Optics*, 7(10):S371, 2005.
- [33] A. Sørensen and K. Mølmer. Entanglement and quantum computation with ions in thermal motion. *Phys. Rev. A*, 62:022311, 2000.
- [34] J. I. Cirac and P. Zoller. Quantum computation with cold trapped ions. *Phys. Rev. Lett.*, 74:4091–4094, 1995.
- [35] J. J. García-Ripoll, P. Zoller, and J. I. Cirac. Speed optimized two-qubit gates with laser coherent control techniques for ion trap quantum computing. *Phys. Rev. Lett.*, 91:157901, 2003.
- [36] D. F. V. James. Quantum dynamics of cold trapped ions, with application to quantum computation. *Appl. Phys. B*, 66:181–190, 1998.
- [37] C.-C. Joseph Wang and J. K. Freericks. Intrinsic phonon effects on analog quantum simulators with ultracold trapped ions. *Phys. Rev. A*, 86:032329, Sep 2012.
- [38] D. L. Moehring, P. Maunz, S. Olmschenk, K. C. Younge, D. N. Matsukevich, L.-M. Duan, and C. Monroe. Entanglement of single-atom quantum bits at a distance. *Nature*, 449:68, 2007.
- [39] P. Maunz, D. L. Moehring, S. Olmschenk, K. C. Younge, D. N. Matsukevich, and C. Monroe. Quantum interference of photon pairs from two remote trapped atomic ions. *Nature Physics*, 3(8):538–541, June 2007.
- [40] Wolfgang Paul. Electromagnetic traps for charged and neutral particles. *Rev. Mod. Phys.*, 62:531–540, Jul 1990.
- [41] S. Earnshaw. On the nature of the molecular forces which regulate the constitution of the luminiferous ether. *Trans. Camb. Phil. Soc.*, 7:97–112, 1842.
- [42] D. J. Berkeland, J. D. Miller, J. C. Bergquist, W. M. Itano, and D. J. Wineland. Minimization of ion micromotion in a paul trap. *Journal of Applied Physics*, 83(10):5025–5033, 1998.
- [43] HG Dehmelt. Radiofrequency spectroscopy of stored ions i: Storage. *Advances in Atomic and Molecular Physics*, 3:53–72, 1967.
- [44] DJ Wineland, C. Monroe, WM Itano, D. Leibfried, BE King, and DM Meekhof. Experimental issues in coherent quantum-state manipulation of trapped atomic ions. *Journal of Research of the National Institute of Standards and Technology*, 103(3), 1998.

- [45] R.R.A. Syms, T.J. Tate, M.M. Ahmad, and S. Taylor. Design of a microengineered electrostatic quadrupole lens. *Electron Devices, IEEE Transactions on*, 45(11):2304–2311, 1998.
- [46] A. Zverev and H. Blinchikoff. Realization of a filter with helical components. *Component Parts, IRE Transactions on*, 8(3):99–110, 1961.
- [47] Andrew Chew. *Doppler-Free Spectroscopy of Iodine at 739nm*. Undergraduate honors thesis, The University of Michigan, 2008.
- [48] Pierre Dubé and Michael Trinczek. Hyperfine-structure splittings and absorption strengths of molecular-iodine transitions near the trapping frequencies of francium. *JOSA B*, 21(6):1113–1126, 2004.
- [49] Michael Mond, Holger Schoene, Andreas Dienes, Guenter Hollemann, and Wolf Seelert. Highly stable uv-mode-locked lasers with an output power of 35 w at 355 nm. In *Proc. SPIE*, volume 7193, page 71930W, 2009.
- [50] Mingwei Li D. James Kafka. Method and apparatus for laser micro-machining of polymeric articles using a mode-locked laser. *Patent*, (EP 1490195 A1), 12 2004.
- [51] D. Hayes, D. N. Matsukevich, P. Maunz, D. Hucul, Q. Quraishi, S. Olmschenk, W. Campbell, J. Mizrahi, C. Senko, and C. Monroe. Entanglement of atomic qubits using an optical frequency comb. *Phys. Rev. Lett.*, 104(14):140501, 2010.
- [52] Louis Deslauriers. *Cooling and heating of the quantum motion of trapped Cd^+ ions*. PhD thesis, University of Michigan., 2006.
- [53] Aaron Christopher Lee. *Ytterbium Ion Qubit State Detection On An ICCD Camera*. Undergraduate honors thesis, University of Maryland, 2012.
- [54] C Shen and L-M Duan. Correcting detection errors in quantum state engineering through data processing. *New Journal of Physics*, 14(5):053053, 2012.
- [55] K Kim, S Korenblit, R Islam, EE Edwards, MS Chang, C Noh, H Carmichael, GD Lin, LM Duan, CC Joseph Wang, et al. Quantum simulation of the transverse ising model with trapped ions. *New Journal of Physics*, 13(10):105003, 2011.
- [56] P. J. Lee, B. B. Blinov, K.-A. Brickman, L. Deslauriers, M. Madsen, R. Miller, D. L. Moehring, D. Stick, and C. Monroe. Atomic qubit operations with an electro-optic modulator. *Opt. Lett.*, 28:1582, 2003.
- [57] K. Kim, M.-S. Chang, R. Islam, S. Korenblit, L.-M. Duan, and C. Monroe. Entanglement and tunable spin-spin couplings between trapped ions using multiple transverse modes. *Phys. Rev. Lett.*, 103(12):120502, 2009.

- [58] H T Quan and W H Zurek. Testing quantum adiabaticity with quench echo. *New Journal of Physics*, 12:093025, 2010.
- [59] K. Kim, M.-S. Chang, S. Korenblit, R. Islam, E. E. Edwards, J.K. Freericks, G.D. Lin, L.-M. Duan, and C. Monroe. Quantum simulation of frustrated ising spins with trapped ions. *Nature*, 465:590–593, 2010.
- [60] G-D Lin, C Monroe, and L-M Duan. Sharp phase transitions in a small frustrated network of trapped ion spins. *Physical Review Letters*, 106(23):230402, 2011.
- [61] P Lecheminant and HP Diep. Frustrated spin systems, 2005.
- [62] GH Wannier. Antiferromagnetism. the triangular ising net. *Physical Review*, 79(2):357, 1950.
- [63] MJ Harris, ST Bramwell, DF McMorro, Th Zeiske, and KW Godfrey. Geometrical frustration in the ferromagnetic pyrochlore $\text{Ho}_2\text{Ti}_2\text{O}_7$. *Physical Review Letters*, 79(13):2554–2557, 1997.
- [64] Steven T Bramwell and Michel JP Gingras. Spin ice state in frustrated magnetic pyrochlore materials. *Science*, 294(5546):1495–1501, 2001.
- [65] Christopher M Dawson, Henry L Haselgrove, and Michael A Nielsen. Noise thresholds for optical cluster-state quantum computation. *Physical Review A*, 73(5):052306, 2006.
- [66] Bruce Normand and Andrzej M Oleś. Frustration and entanglement in the t_{2g} spin-orbital model on a triangular lattice: Valence-bond and generalized liquid states. *Physical Review B*, 78(9):094427, 2008.
- [67] Otfried Gühne and Gza Tth. Entanglement detection. *Physics Reports*, 474(16):1 – 75, 2009.
- [68] C. A. Sackett, D. Kielpinski, B. E. King, C. Langer, V. Meyer, C. J. Myatt, M. Rowe, Q. A. Turchette, W. M. Itano, D. J. Wineland, and C. Monroe. Experimental entanglement of four particles. *Nature*, 404:256, 2000.
- [69] H Schmitz, A Friedenauer, Ch Schneider, R Matjeschk, M Enderlein, T Huber, J Glueckert, D Porras, and T Schaetz. The arch of simulating quantum spin systems with trapped ions. *Applied Physics B*, 95(2):195–203, 2009.
- [70] E. E. Edwards, S. Korenblit, K. Kim, R. Islam, M.-S. Chang, J. K. Freericks, G.-D. Lin, L.-M. Duan, and C. Monroe. Quantum simulation and phase diagram of the transverse-field ising model with three atomic spins. *Phys. Rev. B*, 82:060412, 2010.
- [71] Tommaso Caneva, Rosario Fazio, and Giuseppe E Santoro. Adiabatic quantum dynamics of the lipkin-meshkov-glick model. *Physical Review B*, 78(10):104426, 2008.

- [72] X. L. Deng, D. Porras, and J. I. Cirac. Effective spin quantum phases in systems of trapped ions. *Physical Review A*, 72(6):063407, 2005.
- [73] Dietrich Leibfried, Emanuel Knill, Signe Seidelin, Joe Britton, R Brad Blakestad, John Chiaverini, David B Hume, Wayne M Itano, John D Jost, Christopher Langer, et al. Creation of a six-atom schrödinger catstate. *Nature*, 438(7068):639–642, 2005.
- [74] R Ozeri, WM Itano, RB Blakestad, J Britton, J Chiaverini, JD Jost, C Langer, D Leibfried, R Reichle, S Seidelin, et al. Errors in trapped-ion quantum gates due to spontaneous photon scattering. *Physical Review A*, 75(4):042329, 2007.
- [75] W. C. Campbell, J. Mizrahi, Q. Quraishi, C. Senko, D. Hayes, D. Hucul, D. N. Matsukevich, P. Maunz, and C. Monroe. Ultrafast gates for single atomic qubits. *Phys. Rev. Lett.*, 105:090502, 2010.
- [76] Craig R Clark, Tzvetan S Metodi, Samuel D Gasster, and Kenneth R Brown. Resource requirements for fault-tolerant quantum simulation: The ground state of the transverse ising model. *Physical Review A*, 79(6):062314, 2009.
- [77] R. Islam, E.E. Edwards, K. Kim, S. Korenblit, C. Noh, H. Carmichael, G.-D. Lin, L.-M. Duan, C.-C. Joseph Wang, J.K. Freericks, and C. Monroe. Onset of a quantum phase transition with a trapped ion quantum simulator. *Nat Commun*, 2(377), 2011.
- [78] Lin, G.-D., Zhu, S.-L., Islam, R., Kim, K., Chang, M.-S., Korenblit, S., Monroe, C., and Duan, L.-M. Large-scale quantum computation in an anharmonic linear ion trap. *Euro. Phys. Lett.*, 86:60004, 2009.
- [79] Roman Schmied, Janus H Wesenberg, and Dietrich Leibfried. Optimal surface-electrode trap lattices for quantum simulation with trapped ions. *Physical review letters*, 102(23):233002, 2009.
- [80] Robert J Clark, Tongyan Lin, Kenneth R Brown, and Isaac L Chuang. A two-dimensional lattice ion trap for quantum simulation. *Journal of Applied physics*, 105(1):013114–013114, 2009.
- [81] D. Porras and J. I. Cirac. Effective quantum spin systems with trapped ions. *Phys. Rev. Lett.*, 92(20):207901, 2004.
- [82] Y.-J. Han, R. Raussendorf, and L.-M. Duan. Scheme for demonstration of fractional statistics of anyons in an exactly solvable model. *Phys. Rev. Lett.*, 98(15):150404, 2007.
- [83] A. Kitaev. Fault-tolerant quantum computation by anyons. *Ann. Phys.*, 303:2–30, 2003.

- [84] Chetan Nayak, Steven H Simon, Ady Stern, Michael Freedman, and Sankar Das Sarma. Non-abelian anyons and topological quantum computation. *Reviews of Modern Physics*, 80(3):1083, 2008.
- [85] Jonathan Simon, Waseem S. Bakr, Ruichao Ma, M. Eric Tai, Philipp M. Preiss, and Markus Greiner. Quantum simulation of antiferromagnetic spin chains in an optical lattice. *Nature*, 472:307–312, 2011.
- [86] Per Bak. The devil’s staircase. *Physics Today*, 39:38–45, 1986.
- [87] Philipp Hauke, Fernando M Cucchietti, Alexander Müller-Hermes, Mari-Carmen Bañuls, J Ignacio Cirac, and Maciej Lewenstein. Complete devil’s staircase and crystal–superfluid transitions in a dipolar xxz spin chain: a trapped ion quantum simulation. *New Journal of Physics*, 12(11):113037, 2010.
- [88] Per Bak and R Bruinsma. One-dimensional ising model and the complete devil’s staircase. *Physical Review Letters*, 49(4):249–251, 1982.
- [89] Zhaohui Wei and Mingsheng Ying. Quantum adiabatic computation and adiabatic conditions. *Phys. Rev. A*, 76:024304, Aug 2007.
- [90] Marcos Rigol, Vanja Dunjko, and Maxim Olshanii. Thermalization and its mechanism for generic isolated quantum systems. *Nature*, 452(7189):854–858, 2008.
- [91] JM Deutsch. Quantum statistical mechanics in a closed system. *Physical Review A*, 43(4):2046, 1991.
- [92] T. Monz, P. Schindler, J. T. Barreiro, M. Chwalla, D. Nigg, W. A. Coish, M. Harlander, W. Hänsel, M. Hennrich, and R. Blatt. 14-Qubit Entanglement: Creation and Coherence. *Physical Review Letters*, 106(13):130506, April 2011.
- [93] Alejandro Perdomo-Ortiz, Neil Dickson, Marshall Drew-Brook, Geordie Rose, and Alán Aspuru-Guzik. Finding low-energy conformations of lattice protein models by quantum annealing. *Scientific Reports*, 2, 2012.
- [94] S Korenblit, D Kafri, W C Campbell, R Islam, E E Edwards, Z-X Gong, G-D Lin, L-M Duan, J Kim, K Kim, and C Monroe. Quantum simulation of spin models on an arbitrary lattice with trapped ions. *New Journal of Physics*, 14(9):095024, 2012.
- [95] D. J. Wineland, C. Monroe, W. M. Itano, D. Leibfried, B. E. King, and D. M. Meekhof. Experimental issues in coherent quantum-state manipulation of trapped atomic ions. *J. Res. Nat. Inst. Stand. Tech.*, 103:259–328, 1998.
- [96] D. Wineland and R. Blatt. Entangled states of trapped atomic ions. *Nature*, 453:1008–1014, 2008.

- [97] J. M. Taylor and T. Calarco. Wigner crystals of ions as quantum hard drives. *Phys. Rev. A*, 78:062331, 2008.
- [98] R. J. Clark, T. Linb, K. R. Brown, and I. L. Chuang. A two-dimensional lattice ion trap for quantum simulation. *J. Appl. Phys.*, 105:013114, 2009.
- [99] Roman Schmied, Janus H. Wesenberg, and Dietrich Leibfried. Optimal surface-electrode trap lattices for quantum simulation with trapped ions. *Phys. Rev. Lett.*, 102:233002, 2009.
- [100] P. C. Haljan, K.-A. Brickman, L. Deslauriers, P. J. Lee, and C. Monroe. Spin-dependent forces on trapped ions for phase-stable quantum gates and entangled states of spin and motion. *Phys. Rev. Lett.*, 94:153602, 2005.
- [101] Shi-Liang Zhu, C. Monroe, and L.-M. Duan. Trapped ion quantum computation with transverse phonon modes. *Phys. Rev. Lett.*, 97, 2006.
- [102] D. Leibfried, R. Blatt, C. Monroe, and D. Wineland. Quantum dynamics of single trapped ions. *Rev. Mod. Phys.*, 75:281–324, 2003.
- [103] J. J. Garca-Ripoll, P. Zoller, and J. I. Cirac. Coherent control of trapped ions using off-resonant lasers. *Phys. Rev. A*, 71:062309, Jun 2005.
- [104] R. Moessner and A. P. Ramirez. Geometrical frustration. *Phys. Today*, 59:24, Feb 2006.
- [105] C. Knoernschild, X. L. Zhang, L. Isenhower, A. T. Gill, F. P. Lu, M. Saffman, and J. Kim. Independent individual addressing of multiple neutral atom qubits with a micromirror-based beam steering system. *Appl. Phys. Lett.*, 97(13):134101, 2010.
- [106] C. Knoernschild, T. Kim, P. Maunz, S. Crain, and J. Kim. Stable optical phase modulation with micromirrors. *arXiv:1108.5782*, 2011.
- [107] F. Shaikh, A. Ozakin, J. M. Amini, H. Hayden, C.-S. Pai, C. Volin, D. R. Denison, D. Faircloth, A. W. Harter, and R. E. Slusher. Monolithic microfabricated symmetric ion trap for quantum information processing. *arXiv:1105.4909*, 2011.
- [108] A. Kitaev. Anyons in an exactly solved model and beyond. *Annals of Physics*, 321(1):2–111, 2006.
- [109] M. M. Rams, M. Zwolak, and B. Damski. A quantum phase transition in a quantum external field: The formation of a Schroedinger magnet. *arXiv:1201.1932*, January 2012.
- [110] B. P. Lanyon, C. Hempel, D. Nigg, M. Müller, R. Gerritsma, F. Zhinger, P. Schindler, J. T. Barreiro, M. Rambach, G. Kirchmair, M. Hennrich, P. Zoller, R. Blatt, and C. F. Roos. Universal digital quantum simulation with trapped ions. *Science*, 2011.

- [111] Michael J. Biercuk, Hermann Uys, Aaron P. VandeVender, Nobuyasu Shiga, Wayne M. Itano, and John J. Bollinger. High-fidelity quantum control using ion crystals in a penning trap. *Quantum Information & Computation*, 9(11):920–949, 2011.